

5-1-2016

(U-Th)/He Studies of the Southern Snake Range Metamorphic Core Complex, NV and Gypsum Valley Salt Wall, Paradox Basin, CO, USA

Sarah Lynn Evans
University of Nevada, Las Vegas

Follow this and additional works at: <https://digitalscholarship.unlv.edu/thesesdissertations>



Part of the [Geology Commons](#)

Repository Citation

Evans, Sarah Lynn, "(U-Th)/He Studies of the Southern Snake Range Metamorphic Core Complex, NV and Gypsum Valley Salt Wall, Paradox Basin, CO, USA" (2016). *UNLV Theses, Dissertations, Professional Papers, and Capstones*. 2665.
<http://dx.doi.org/10.34917/9112061>

This Dissertation is protected by copyright and/or related rights. It has been brought to you by Digital Scholarship@UNLV with permission from the rights-holder(s). You are free to use this Dissertation in any way that is permitted by the copyright and related rights legislation that applies to your use. For other uses you need to obtain permission from the rights-holder(s) directly, unless additional rights are indicated by a Creative Commons license in the record and/or on the work itself.

This Dissertation has been accepted for inclusion in UNLV Theses, Dissertations, Professional Papers, and Capstones by an authorized administrator of Digital Scholarship@UNLV. For more information, please contact digitalscholarship@unlv.edu.

(U-TH)/HE STUDIES OF THE SOUTHERN SNAKE RANGE METAMORPHIC CORE
COMPLEX, NV AND GYPSUM VALLEY SALT WALL,
PARADOX BASIN, CO, USA

By

Sarah Lynn Evans

Bachelor of Science — Geoscience
University of North Carolina, Chapel Hill
2008

Master of Science — Geology
University of Kansas
2011

A dissertation submitted in partial fulfillment
of the requirements for the

Doctor of Philosophy — Geoscience

Department of Geoscience
College of Sciences
The Graduate College

University of Nevada, Las Vegas
May 2016

Dissertation Approval

The Graduate College
The University of Nevada, Las Vegas

April 14, 2016

This dissertation prepared by

Sarah Lynn Evans

entitled

(U-TH)/HE Studies of the Southern Snake Range Metamorphic Core
Complex, NV and Gypsum Valley Salt Wall, Paradox Basin, CO, USA

is approved in partial fulfillment of the requirements for the degree of

Doctor of Philosophy - Geoscience
Department of Geoscience

Andrew Hanson, Ph.D.
Examination Committee Chair

Kathryn Hausbeck Korgan, Ph.D.
Graduate College Interim Dean

Terry Spell, Ph.D.
Examination Committee Member

Wanda Taylor, Ph.D.
Examination Committee Member

Brenda Buck, Ph.D.
Examination Committee Member

Liam Frink, Ph.D.
Graduate College Faculty Representative

Abstract

(U-Th)/He studies of the Southern Snake Range Metamorphic Core Complex, NV and Gypsum Valley Salt Wall, Paradox Basin, CO, USA

by

Sarah Lynn Evans

Dr. Andrew D. Hanson, Examination Committee Chair
Associate Professor of Geology
Associate Dean of the Honors College
University of Nevada, Las Vegas

This dissertation presents three studies that investigate extension in the Southern Snake Range (SSR) metamorphic core complex (MCC) of east-central Nevada and a thermal anomaly associated with the Gypsum Valley salt wall (GVSW) of southwestern Colorado. Low temperature thermochronologic studies using the (U-Th)/He system have been applied in numerous geologic settings to understand erosional and tectonic denudation processes. Two of the studies presented use (U-Th)/He thermochronology, combined with other techniques, to investigate the extensional history of the SSR and the extent of the GVSW thermal anomaly. Both of these studies present novel methods for understanding the thermal histories of the study area using (U-Th)/He thermochronology. The third study uses geologic mapping to document the complexly deformed upper plate of the SSR metamorphic core complex.

The extensional history of the SSR, located in the Northern Basin and Range (NBR), is constrained using computer modeling of new zircon and apatite (U-Th)/He (ZrnHe and ApHe) ages and previously published low-temperature thermochronologic analyses from the footwall of the Southern Snake Range Décollement (SSRD), the major detachment fault of the MCC. The combined analytical and modeling approach suggests that extension within the SSR was episodic during the Cenozoic, and occurred in three major pulses during the Eocene, Oligocene, and

Miocene. The interpretations of the timing, rate, and magnitude of extension from this study suggest that the collapse of the Nevadaplano, a plateau of thickened crust located in the Sevier hinterland, initiated prior to ~17 Ma. Additionally, this study found no relationship between the extensional history of the SSR and nearby magmatism during the Cenozoic. Both of these conclusions are in contrast with previously published research for the NBR.

The size and magnitude of a suprasalt thermal anomaly associated with the GVSF, a salt wall of the northern Paradox Basin, was investigated using the combination of ApHe thermochronology and thermal maturation analyses of rock samples located in a suprasalt position, or a position above or adjacent to the top of a salt body. Previously published modeling of salt thermal anomalies suggests sedimentary units located in suprasalt positions will be at elevated temperatures, compared to regional temperatures, for a distance of one to three salt radii from the contact between salt and other rock units. Evaluating the predictive capabilities of salt thermal anomaly models using field based studies has important implications for the energy industry because these thermal anomalies may influence hydrocarbon maturation, petroleum reservoir cementation, or the locations of geothermal fields associated with salt bodies. The combined ApHe and thermal maturation analyses show no evidence for a thermal anomaly at the size or scale of the model prediction. The apparent absence of a salt thermal anomaly associated with the GVSF may be the result of thermal conductivity contrasts between salt and adjacent sediments that are not conducive to the development of a thermal anomaly, or the result of significant convective or advective heat transfer near the salt body. These interpretations suggest that future salt thermal anomaly models should incorporate convective and advective heat transfer mechanisms, and location specific values for thermal conductivity contrasts.

The final study presented uses geologic mapping to document the complex structures due to extension within the SSR metamorphic core complex. A map at the 1:24,000 scale of the Red Ledges 7.5' quadrangle, located at the southern edge of the SSR, was completed using traditional field techniques. This new geologic mapping was completed at a higher resolution than previously published maps of the area, and as a result provides more detailed documentation of this portion of the complexly faulted upper plate of the SSR MCC. The higher resolution mapping can be used by researchers investigating the specific extensional history of the SSR, or by researchers investigating deformation patterns within upper plates of MCCs.

Acknowledgements

This research was made possible by a variety of funding sources, and support from numerous individuals. Funding sources include the President's UNLV Foundation Graduate Research Fellowship, the Fay and Jack Ross Fellowship, an American Association of Petroleum Geologists Grant-in-Aid, Graduate Student Research Grants from the Nevada Petroleum and Geothermal Society, Graduate and Professional Student Association Research Grants, a Graduate Student Research Grant from the Geological Society of America, Geoscience Departmental scholarships, the Department of Interior, and funding from the STAR (Salt and Thermal Anomaly Research) Consortium at UNLV.

Dr. Andrew Hanson provided the everyday practical advice, scientific guidance, and humor in the office and field that made this research possible. I am now a better scientist, field cook, and person because of him. Thank you Andrew for being both interesting and illuminating, and for never making me feel (too) ridiculous for screaming-at-the-top-of-my-lungs while hopping from foot-to-foot when I heard a rattlesnake.

The members of my committee, Dr. Wanda Taylor, Dr. Brenda Buck, Dr. Terry Spell, and Dr. Liam Frink were also instrumental in my growth as a scientist while at UNLV. Without their suggestions and guidance, I would not have been able to complete my degree or have found employment following graduation. Dr. Wanda Taylor provided invaluable assistance in retrodeforming geologic cross sections, and discussion of extension in eastern Nevada during the Neogene. Dr. Brenda Buck's guidance and advice greatly improved the description of Quaternary deposits and surfaces.

Dr. Kip V. Hodges, Dr. Matthijs van Soest, Michelle Aigner, and Dr. Wendy Bohon provided the support and infrastructure necessary to complete the (U-Th)/He analyses presented

in this work. Dr. Richard Styron was an important collaborator for the research presented in Chapter 2, and without his help the results and interpretations would have been impossible. I would also like to thank my multiple field assistants, Kirellos Sefein, Joseph Miller, Robert Springs, Marcio Cardoso Jr., and Richard Ness, who helped with the collection of samples and the completion of the mapping presented in Chapter 4.

Finally, thank you to all of my friends and family that supported me throughout the completion of my dissertation.

*This dissertation is dedicated to the fifteen rattlesnakes I counted and the others I never saw—
your tolerance of my presence is greatly appreciated.*

Table of Contents

Approval Page	ii
Abstract.....	iii
Acknowledgements	vi
List of Tables	xiv
List of Figures.....	xv
Chapter 1: Dissertation overview	1
Chapter 2: Zircon and apatite (U-Th)/He evidence for Paleogene to Neogene extension in the Southern Snake Range, Nevada, USA	5
1. Introduction.....	6
2. Regional Geologic Setting.....	8
3. Snake Range Geologic Setting	11
<i>3.1 Extensional History of the SSRD</i>	<i>11</i>
4. (U-Th)/He Thermochronology	13
<i>4.1 (U-Th)/He Results</i>	<i>14</i>
<i>4.1.1 Zircon (U-Th)/He Results</i>	<i>15</i>
<i>4.1.2 Apatite (U-Th)/He Results.....</i>	<i>16</i>
<i>4.2 Thermochronologic Data Interpretation</i>	<i>16</i>
5. Thermochronologic Modeling.....	19
<i>5.2 Construction of Priors</i>	<i>21</i>
<i>5.2.1 Filtering of Priors to Fit Structural Constraints</i>	<i>23</i>
<i>5.3 Calculating Likelihood with Pecube.....</i>	<i>24</i>
<i>5.4 Posterior Sampling</i>	<i>25</i>

5.5 Model Results.....	25
5.6 Relationships Between Model Variables and Results.....	28
5.6.1 Relationship Between Crustal Heat and Deformation.....	28
6. Discussion	29
6.1 Extension in the SSR and NSR	30
6.2 Sedimentary Evidence for SSR Extension	32
6.3 Cenozoic Magmatism and Extension in the SSR.....	33
6.4 Conceptual Evolution of the SSR	34
6.5 Regional Context of SSR Extension	35
7. Conclusions.....	37
Figures.....	39
Tables	57
Chapter 3: Constraints on the salt thermal anomaly associated with the Gypsum Valley salt wall, Paradox Basin, CO	59
Abstract.....	59
1. Introduction.....	60
1.1 Application of (U-Th)/He thermochronology and thermal maturation indicators	63
2. Geologic setting	66
2.1 Formation of the Paradox Basin and relevant stratigraphy.....	67
2.2 Timing and mechanism of salt movement	69
2.3 Tertiary surface exposure of the GVSW.....	70
3. Methodology	70
3.1 T_{max} , R_o , and TAI.....	71

3.2 (U-Th)/He thermochronology	73
3.3 Salt distance measurements	74
3.3.1 Surface measurements	74
3.3.2 Sub-surface measurements.....	74
4. Results	77
4.1 T_{max} , R_o , and TAI results	77
4.2 Apatite (U-Th)/He results	77
5. Discussion	78
5.1 T_{max} , R_o , and TAI interpretations	78
5.2 (U-Th)/He results and distance to salt.....	81
5.3 Apparent absence of a suprasalt thermal anomaly.....	83
5.3.1 GVSW geometry and modeling literature	84
5.3.2 Burial depth of the GVSW.....	85
5.3.3 Thermal conductivity contrasts.....	86
5.3.4 Potential impact of advective or convective heat transfer.....	89
6. Conclusions.....	90
Figures.....	92
Tables	110
 Chapter 4: Preliminary map of the Red Ledges 7.5' quadrangle, White Pine and Lincoln Counties, Nevada	 113
1. Introduction.....	113
2. Methods.....	113
3. Description of Map Units	115

3.1 Quaternary Units	115
3.2 Cenozoic Units	117
3.3 Paleozoic Units	121
4. Structure	125
4.1 Pre-Oligocene unconformity.....	125
4.2 Cross section A-A'	125
4.3 Cross section B-B'	126
Tables	127
Appendix 1: Supplemental material for Chapter 2	128
1. Overview of Contents	128
1.2 Paleodepth Reconstruction	128
1.3 Reprint permission	129
1.4 Supporting Tables	129
Appendix 1 Figures	130
Appendix 2: Supplemental material for Chapter 3	135
1. Overview of Contents	135
Appendix 2 Figure.....	136
Appendix 2 Tables	138
Appendix 3: Plate of preliminary geologic map of the Red Ledges 7.5' quadrangle	140
Appendix 4: $^{40}\text{Ar}/^{39}\text{Ar}$ data from Chapter 4	141
1. Overview of Contents	141
2. Analytical Procedures.....	141
Appendix 4 Figures	142

Appendix 4 Tables	152
References.....	157
Curriculum Vitae.....	178

List of Tables

Table 2.1 (U-Th)/He age data.....	57
Table 2.2 Pecube modeling input parameters	58
Table 3.1 Salt thermal anomaly predictions from modeling literature	110
Table 3.2 Mudstone sample data	111
Table 3.3 Apatite (U-Th)/He data.....	112
Table 4.1 $^{40}\text{Ar}/^{39}\text{Ar}$ ages of volcanic units in the Red Ledges quadrangle.....	127
Table A1.1 Replicate zircon (U-Th)/He analyses	133
Table A1.2 Replicate apatite (U-Th)/He analyses	134
Table A2.1 Replicate apatite (U-Th)/He analyses	138
Table A2.2 Well data from Chapter 3.....	139
Table A4.1 12RS03, sanidine, single crystal fusion ^a	152
Table A4.2 12SR08, amphibole, 22.18 mg ^a	153
Table A4.3 12SR09, plagioclase, 17.90 mg ^a	154
Table A4.4, 14SR01, single crystal sanidine ^a	155
Table A4.5 14SR02, single crystal plagioclase ^a	156

List of Figures

Figure 2.1 Generalized geologic map, sample locations, and cross section	39
Figure 2.2 Zircon and apatite (U-Th)/He versus distance from the SSRD.....	41
Figure 2.3 Example of model cross section	43
Figure 2.4 Comparison of modeled and measured cooling ages	45
Figure 2.5 Modeled extension histories.....	47
Figure 2.6 Histograms for the posterior model results of the SSR.....	49
Figure 2.7 Plots of various variables used in models.....	51
Figure 2.8 Interpreted model histories.....	53
Figure 2.9 Conceptual evolution of the SSR.....	55
Figure 3.1 Location map of study area	92
Figure 3.2 Conceptual model for use of (U-Th)/He dating.....	94
Figure 3.3 Simplified geologic map and cross section	96
Figure 3.4 Interpolated Paradox salt surfaces	98
Figure 3.5 Thickness of Paradox salt and interpreted cross section	100
Figure 3.6 Plot of R_0 and (U-Th)/He versus distance to salt	102
Figure 3.7 Plot of R_0 and (U-Th)/He versus depth to salt.....	104
Figure 3.8 Plot of R_0 and (U-Th)/He versus salt thickness.....	106
Figure 3.9 Paleo-isotherm interpretations.....	108
Figure A1.1 Paleodepth reconstruction	130
Figure A1.2 Previously published journal article reprint permission	132
Figure A2.1 Well locations	136
Figure A4.1 12SR03 (sanidine)	142

Figure A4.2 12SR08 (amphibole).....	144
Figure A4.3 12SR09 (plagioclase).....	146
Figure A4.4 14SR01 (sanidine)	148
Figure A4.5 14SR02 (plagioclase).....	150

Chapter 1: Dissertation overview

This dissertation presents research from two geologic investigations into (1) the tectonic evolution of the Southern Snake Range (SSR) metamorphic core complex (MCC) located in east-central Nevada, and (2) the magnitude and extent of a salt thermal anomaly within the Paradox Basin, southwestern Colorado. Chapter 2 “Zircon and apatite (U-Th)/He evidence for Paleogene to Neogene extension in the Southern Snake Range, Nevada, USA” and Chapter 4 “Preliminary map of the Red Ledges 7.5’ quadrangle, White Pine and Lincoln Counties, Nevada” address the tectonic evolution of the SSR MCC by focusing on extension in the lower plate (Chapter 2) and in the upper plate (Chapter 4) of the core complex. Chapter 3 “Constraints on the salt thermal anomaly associated with the Gypsum Valley salt wall, Paradox Basin, CO” is an outcrop based study that evaluates the predictive capabilities of mathematical models of salt thermal anomalies near the Gypsum Valley salt wall (GVSW) in the Paradox Basin, Colorado. Although the investigations into the evolution of a Basin and Range metamorphic core complex and a Paradox Basin salt wall are not located within similar geologic settings, both investigations apply low-temperature thermochronology in novel ways to better understand the geologic history. The work presented in this dissertation highlights how low-temperature thermochronology may be combined with fieldwork and other techniques to understand various geologic processes.

Chapter 2 presents thermokinematic modeling of new zircon and apatite (U-Th)/He analyses and previously published zircon and apatite fission track data [Miller *et al.*, 1999] to constrain the timing, magnitude, and rates of extension in the SSR. Quantifying the extensional history of the SSR MCC, an important extensional feature of the Basin and Range, has implications on the evolution of extension within the province. The thermokinematic modeling

methods presented in this chapter builds upon previously published methods, and this new approach can be applied to a variety of extensional provinces to quantify the rates, timing, and magnitude of extension. The research presented in Chapter 2 was originally published in the journal *Tectonics* in 2015 by *Evans et al.* [2015]. The article was written in collaboration with Dr. Richard H. Styron, Dr. Matthijs C. van Soest, Dr. Kip V. Hodges, and Dr. Andrew D. Hanson. Dr. Styron developed the new Bayesian Monte Carlo method incorporating Pecube (a thermal modeling software package [*Braun*, 2003; *Braun et al.*, 2012]) and the computer scripts used to implement this new modeling technique. As a result, this chapter contains original work and writing from Dr. Styron throughout, and particularly in section 5 on the modeling technique and discussion of the validity of the posterior modeling results. (U-Th)/He analyses were completed at Group 18 Laboratories at Arizona State University. Dr. van Soest and Dr. Hodges developed the protocol for (U-Th)/He analyses, age reductions, and error analysis. The presentation of the error analysis of the (U-Th)/He data in Chapter 2 is summarized from Group 18 Laboratories operating procedures, with additional input from Dr. van Soest and Dr. Hodges. The discussions of the (U-Th)/He data and thermokinematic modeling results with Dr. Styron, Dr. van Soest, Dr. Hodges, Dr. Hanson and Dr. Wanda Taylor were crucial to the development of the ideas presented in Chapter 2. The entire publication also benefitted from careful editing and written input from co-authors of the journal article, and editing from dissertation committee members, the editorial staff of *Tectonics*, and two anonymous reviewers.

Chapter 3 investigates the size and magnitude of a salt thermal anomaly associated with GVSW located in the Paradox Basin of southwestern Colorado. Similar to Chapter 2, this study uses apatite (U-Th)/He (ApHe) thermochronology in a novel way to understand the thermal history of the area. The ApHe technique was combined with thermal maturity analyses (vitrinite

reflectance, Rock-Eval pyrolysis data, and thermal alteration index) in an outcrop based study aimed at investigating a possible thermal anomaly associated with the GVSF. The magnitude and size of salt thermal anomalies have been predicted using modeling techniques [e.g., *Selig and Wallick*, 1966; *Geertsma*, 1971; *Jensen*, 1983; *O'Brien and Lerche*, 1984; *Vizgirda et al.*, 1985; *Jensen*, 1990; *Yu et al.*, 1992; *Mello et al.*, 1995; *Petersen and Lerche*, 1995]. This study investigates the usefulness of these models for predicting the size and magnitude of a thermal anomaly associated with the GVSF. The findings from this study suggest the salt thermal anomaly models are not predictive near the GVSF, which has important implications for use of these models by the energy industry. The ApHe analyses from this chapter were also completed at Group 18 Laboratories at Arizona State University following the analytical procedures and error analysis developed by Dr. Hodges and Dr. van Soest. The description of error analysis is summarized from procedures developed by Dr. Hodges and Dr. van Soest. Analyses of mudstones used in this chapter were completed by StratoChem services, and analytical procedures are summarized from the company website (www.stratochem.com) and from references cited in the chapter. Interpretations from this chapter were completed in collaboration with Dr. Hanson, Dr. Hodges, and Dr. van Soest.

Chapter 4 presents a new geologic map of the 7.5' Red Ledges quadrangle, located in the southernmost SSR. This new map of the complexly faulted and folded upper plate of the SSRD may be used in future investigations into geologic processes of MCC. The geologic mapping was completed in collaboration with Dr. Hanson, and several field assistants were present during the mapping process: Kirellos Sefein, Joseph Miller, Robert Springs, and Richard Ness. The mapping and description of Quaternary deposits and surfaces greatly benefitted from the input of Dr. Brenda Buck. $^{40}\text{Ar}/^{39}\text{Ar}$ analyses of mineral separates from the volcanic units presented in

Chapter 4 and Appendix 4 were completed at the Nevada Isotope Geochemistry Laboratory (NIGL) at the University of Nevada, Las Vegas by Dr. Terry Spell and Kathleen Zanetti. NIGL provided tables and graphs depicting the results of these analyses in Appendix 3. Dr. Taylor reviewed early versions of this map, and provided valuable input on retrodeformation of cross sections and the final version of the map presented.

Chapter 2: Zircon and apatite (U-Th)/He evidence for Paleogene to Neogene extension in the Southern Snake Range, Nevada, USA

Abstract

Despite decades of study, the timing, rates, and magnitude of extension in the Basin and Range are poorly quantified in some areas. This study integrates new zircon and apatite (U-Th)/He analyses (ZrnHe, ApHe) with published thermochronologic data to quantify these extensional parameters in the Southern Snake Range (SSR) of east-central Nevada. The new ZrnHe dates range from 40.7 ± 4.9 Ma in the western SSR to 21.0 ± 3.3 Ma near the present-day trace of the Southern Snake Range Décollement (SSRD), and the ApHe dates range from 15.1 ± 2.4 Ma in the central SSR to 13.6 ± 0.7 Ma closest to the SSRD trace. These new and previously published low-temperature thermochronologic cooling ages were inverted for the extensional history of the SSR using a Bayesian Monte Carlo method incorporating Pecube. The posterior extensional histories indicate three significant pulses of extension occurred during the Paleogene and Neogene: (1) ~ 50 -45 to ~ 38 Ma (Eocene), (2) ~ 33 -30 to ~ 23 Ma (Oligocene), and (3) ~ 23 -20 to ~ 10 -8 Ma (Miocene). Modeled rates of extension were low at $\leq 0.5 \text{ mm a}^{-1}$; however, more rapid rates possibly occurred during the Eocene and the Miocene based on posterior histories. Net cumulative extension from posterior histories is 19.8 to 34.9 km, with a mean of 29.7 km. About 10-18 km of extension occurred during the Eocene and Oligocene. Model results indicate no relationship between extension and magmatism in the SSR. Our new model results and interpretations also indicate extensional collapse of the Nevadaplano initiated prior to ~ 17 Ma.

Sarah Evans was the first author for this previously published journal article from *Tectonics*, and contributing authors, in order from publication, are Richard H. Styron, Matthijs C. van Soest, Kip V. Hodges, and Andrew D. Hanson.

Citation for previously published article:

Evans, S. L., R. H. Styron, M. C. Soest, K. V. Hodges, and A. D. Hanson (2015), Zircon and apatite (U-Th)/He evidence for Paleogene and Neogene extension in the Southern Snake Range, Nevada, USA, *Tectonics*, 34(10), 2142-2164, doi:10.1002/2015TC003913.

1. Introduction

Over the past several decades, geologic research has focused on the structural history (e.g., the style, timing, rates, and magnitude of extension) of the Basin and Range of western North America. In particular, metamorphic core complexes (MCC) have been a focus of intense study because these features have accommodated large-magnitude extension [e.g., *Coney and Harms*, 1984; *Buck*, 1991; *Wernicke*, 1992]. Determining the structural history of MCC is particularly important for understanding large-scale driving mechanisms for extension within the sub-provinces of the Basin and Range [e.g., *Sonder and Jones*, 1999]. However, despite intense study of MCC in the Northern Basin and Range (NBR) during the past several decades [e.g., *Armstrong*, 1972; *Allmendinger et al.*, 1983; *Miller et al.*, 1983; *Bartley and Wernicke*, 1984; *Dallmeyer et al.*, 1986; *Wells et al.*, 1990; *Hodges and Walker*, 1992; *MacCready et al.*, 1997; *Wells et al.*, 2000; *Colgan and Henry*, 2009; *Konstantinou et al.*, 2012] the structural history has not been strictly quantified throughout the Cenozoic for some of these important features. In the Southern Snake Range (SSR), part of the Snake Range MCC (Figure 2.1a), the structural history is only partially understood for the Southern Snake Range Décollement (SSRD), the main structure responsible for extension in the range [e.g., *Miller et al.*, 1999].

Quantifying the structural history (e.g., timing, magnitude, and rates of extension) for the partially understood SSRD provides new evidence that may be used to address important issues about the extensional history of the NBR. Some models for the evolution of the NBR suggest there are regional links between magmatism and extension [e.g., *Gans et al.*, 1989; *Best and Christiansen*, 1991; *Axen et al.*, 1993; *Best et al.*, 2013b], and the validity of these proposed models can be addressed at the scale of the SSR once the extensional history is better understood. Hypothesized relationships between the Snake Range MCC and other extensional structures of the region [e.g., *Taylor*, 1990; *Taylor and Bartley*, 1992; *Axen et al.*, 1993] may also be tested with information about the extensional history. Additionally, the timing of the collapse of the Nevadaplano may be inferred for this portion of the NBR given quantitative values for the onset and magnitude of extension in the SSR, as previously completed in other regions [e.g., *Colgan and Henry*, 2009]. To constrain these important extensional parameters and address these issues, new thermochronologic data, zircon and apatite (U-Th)/He analyses (ZrnHe and ApHe), were determined for the SSR. These new data were integrated with previously reported zircon and apatite fission track ages (ZrnFT and ApFT) [*Miller et al.*, 1999] by modeling the data using the software package Pecube [*Braun*, 2003; *Braun et al.*, 2012] and methods modified from *Styron et al.* [2013]. *Styron et al.* [2013] defined a methodology for using the Pecube software package to model timing, magnitude, and rates of extension in a Tibetan MCC. Those methods are refined into a more efficient Bayesian inversion for a multistage extensional history, as well as thermal parameters (radiogenic heat production and Moho temperature) that control thermochronometric cooling ages.

The integrated thermochronologic data and modeling allows us to address several important research questions regarding the extensional history of the SSR, such as: (1) Did the

majority of extension in the SSR occur during a Miocene period of extension along the Snake Range-Deep Creek fault system as proposed by *Miller et al.* [1999]? (2) Are there additional periods of extension in the SSR, similar to those documented in the Eocene and Oligocene in the better studied Northern Snake Range (NSR) [e.g., *Lee*, 1995]? (3) What is the magnitude of extension in the SSR and how does it compare to previous estimates by *McGrew* [1993] and *Miller et al.* [1999]? (4) Is there evidence for pre-Cenozoic extension in the SSR as documented in the upper crust of the NBR west of the SSR [e.g., *Druschke et al.*, 2009; *Long et al.*, 2015]? and (5) Does our understanding of temporal relationships between extension and magmatism, relationships to other regionally important structures, and timing of Nevadaplano collapse need to be revised in light of these new data?

2. Regional Geologic Setting

The tectonic history of east-central Nevada extends to at least the late Proterozoic, when Neoproterozoic to Devonian strata were deposited in the passive margin of western North America following the breakup of Rodinia [e.g., *Dickinson*, 2006]. Passive margin sedimentation in the region ceased in the Late Devonian with the onset of the Antler Orogeny [e.g., *Poole et al.*, 1992; *Dickinson*, 2006]. Late Devonian to Pennsylvanian strata of east-central Nevada were deposited in basins associated with the Antler orogeny (e.g., Antler foreland basin) and other late Paleozoic deformation [e.g., *Trexler et al.*, 2004]. The overall thickness of Neoproterozoic to Permian strata in the NSR are estimated at ~10 to 12 km [*Miller et al.*, 1983], and between 10 to 15 km regionally [*Miller et al.*, 1992].

During the Jurassic to Cretaceous this area of east-central Nevada experienced several episodes of plutonic intrusion, metamorphism, and large-scale folding [e.g., *Miller et al.*, 1988; *Dickinson*, 2006]. Several Jurassic aged plutons are exposed in the SSR, NSR, and possibly in

the Schell Creek Range (SCR) [Lee and Christiansen, 1983; Miller *et al.*, 1988]. Jurassic metamorphism reached amphibolite grade in the SSR and was associated with the intrusion of the Snake Creek-Williams Canyon (SCWC) pluton [Miller *et al.*, 1988; McGrew, 1993] at ~160 Ma [Lee and Christiansen, 1983]. East-central Nevada was also intruded by several plutons during the Cretaceous between 110 and 75 Ma [Miller *et al.*, 1988]. The SSR also experienced minor metamorphism around the time of emplacement of a two-mica granite, the Pole Canyon-Can Young Canyon pluton [Miller *et al.*, 1988; McGrew, 1993] at ~79.1 to 79.7 Ma [Lee *et al.*, 1970; Lee *et al.*, 1986]. Penetrative metamorphism in the Cretaceous occurred in the NSR [Miller *et al.*, 1988; Lewis *et al.*, 1999; Cooper *et al.*, 2010], SCR, Deep Creek Range, and Kern Mountains [Miller *et al.*, 1988]. Based on thermobarometric studies, the footwall of the Northern Snake Range Décollement (NSRD) was buried to depths of 25-30 km [Lewis *et al.*, 1999; Cooper *et al.*, 2010] during Cretaceous metamorphism at ~88 Ma [Cooper *et al.*, 2010]. No thermobarometric studies have been completed in the footwall of the SSRD to ascertain depths of burial prior to Cenozoic extension.

East-central Nevada occupied a hinterland position during the Sevier orogeny [e.g., DeCelles and Coogan, 2006]. During the Sevier event, this part of the hinterland was uncut by thrusts based on several studies of the sub-Tertiary/Oligocene unconformity [e.g., Armstrong, 1972; Miller *et al.*, 1983; Long, 2012], leading several authors to conclude that the Sevier hinterland prior to the Tertiary was a thick, elevated orogenic plateau [e.g., Coney and Harms, 1984; DeCelles, 2004]. This “Nevadaplano” [DeCelles, 2004], was located between the Central Nevada thrust belt to the west [Taylor *et al.*, 2000] and the Sevier fold and thrust belt to the east [Coney and Harms, 1984; DeCelles and Coogan, 2006]. Its elevation may have been ≥ 2 km in the Late Cretaceous based on a clumped stable isotope study of carbonates from eastern Nevada

and central Utah [Snell *et al.*, 2014]. Although this region was not involved in thrusting during the Sevier orogeny, some areas underwent syn-convergent extension. This phenomenon is well documented by the onset of mid-crustal extension in the Cretaceous in the Raft River-Albion-Grouse Creek MCC [Wells *et al.*, 1990] and Ruby-East Humboldt MCC [Hodges and Walker, 1992], and by the onset of surface-breaking normal faulting in the Egan Range of east-central Nevada [Druschke *et al.*, 2009] and in the Eureka Culmination of central Nevada [Long *et al.*, 2015].

Following the Sevier orogeny, east-central Nevadan crust was highly attenuated, and experienced minor plutonism and voluminous volcanism during the Cenozoic [e.g., Coney and Harms, 1984; Gans, 1987; Miller *et al.*, 1988; Dickinson, 2006]. Crustal thicknesses of ~50 km in the Sevier hinterland were thinned to present day thicknesses of ~30-35 km during Cenozoic extension in the NBR [Gans, 1987]. Extension in the NBR occurred on both high-angle faults and on low-angle detachments [e.g., Miller *et al.*, 1983; Bartley and Wernicke, 1984; Gans, 1987; Miller *et al.*, 1999].

Multiple periods of extension of varying intensity have been proposed for the Snake Range and the associated Deep Creek Range and Kern Mountains fault systems [Armstrong, 1972; Miller *et al.*, 1983; Lee, 1995; Miller *et al.*, 1999]. Lee [1995] proposed three discrete extensional events at 48-41 Ma, 30-26 Ma, and 20-16 Ma in the NSR using $^{40}\text{Ar}/^{39}\text{Ar}$ MDD modeling of potassium feldspars. A rapid period of extension in the Miocene around 17 Ma was documented in the NSR, SSR, SCR, Deep Creek Range, and in the Kern Mountains based on ZrnFT and ApFT data [Miller *et al.*, 1999]. Quaternary to present day extension on high-angle range bounding faults in east-central Nevada has also been documented [e.g., Dohrenwend *et al.*, 1996; Wesnousky and Willoughby, 2003; U.S. Geological Survey and Nevada Bureau of Mines

and Geology, 2006; *DePolo*, 2008]. A geodetic study documented modern day “distributed extension” from east-central Nevada to west-central Utah [*Kreemer et al.*, 2010].

3. Snake Range Geologic Setting

The NSR is a Cordilleran MCC with a ductilely deformed and mylonitized lower plate in contact with a brittlely extended upper plate along a detachment surface [e.g., *Miller et al.*, 1983; *Coney and Harms*, 1984]. Geologic investigations of the NSR have established a detailed tectonic evolution of the core complex based on mapping, structural analyses, interpretations of geophysical data, thermobarometric, and thermochronologic studies [e.g., *Allmendinger et al.*, 1983; *Miller et al.*, 1983; *Bartley and Wernicke*, 1984; *Gans et al.*, 1985; *Lee and Sutter*, 1991; *Lee*, 1995; *Lewis et al.*, 1999; *Miller et al.*, 1999; *Cooper et al.*, 2010]. The Cenozoic evolution of the SSR and SSRD has been less intensively studied [e.g., *Armstrong*, 1972; *McGrew*, 1993; *Miller et al.*, 1999], possibly because the SSRD was not initially recognized as structurally linked to the NSRD [e.g., *Miller et al.*, 1983]. Nevertheless, the SSRD accommodated a significant amount of extension during the Cenozoic [e.g., *McGrew*, 1993; *Miller et al.*, 1999], and a systematic study of the timing and rates of extension is necessary to fully understand extension in the NBR.

3.1 Extensional History of the SSRD

The SSRD is currently a low-angle structure that is exposed throughout the SSR [e.g., *Whitebread*, 1969; Figure 2.1b]. The SSRD separates metamorphosed Neoproterozoic to Cambrian strata and Mesozoic and Paleogene intrusions in the lower plate [*Lee and Christiansen*, 1983; *Miller et al.*, 1988] from unmetamorphosed Cambrian to Permian strata in the upper plate [*Whitebread*, 1969; *McGrew*, 1993]. Additionally, the upper plate of the SSRD contains a variety of Cenozoic volcanic units and minor sedimentary deposits [*Whitebread*,

1969; McGrew, 1993; Miller *et al.*, 1999]. Although, the SSRD was originally interpreted as a thrust fault, [e.g., Drewes, 1958; Misch, 1960], it was subsequently recognized as a Tertiary extensional feature [Armstrong, 1972] and as part of the extensive (~150 km along strike) Miocene Snake Range-Deep Creek fault system [Miller *et al.*, 1999].

The exact timing of extension along the SSRD is unclear. Cataclasis and mylonitization of a ~36 Ma pluton [Miller *et al.*, 1988] in the SSR suggests extension occurred post-intrusion [McGrew, 1993]. Pre-Oligocene extension may be recorded by ~40-42 Ma ZrnFT ages from the lower plate of SSRD and a pre-31 Ma conglomerate in the upper plate of the SSRD, but the exact timing, amount, and rate of extension prior to the Oligocene is not understood [Miller *et al.*, 1999]. Lee *et al.* [1970] interpreted K-Ar ages from the SSR to indicate movement on the SSRD between ~17-18 Ma, but attributed these ages to thrusting along the SSRD rather than extension. Miller *et al.* [1988] reinterpreted these K-Ar ages to be the result of intrusion of the Young Canyon-Kious Basin pluton at ~36 Ma and hydrothermal alteration. Finally, a fission track study interpreted extension in the SSR to have occurred along high angle normal faults sometime before 31 Ma, based on the ZrnFT data and a pre-31 Ma conglomerate, and again at ~17 Ma, based on ApFT data [Miller *et al.*, 1999]. This Miocene extension was interpreted to have been “rapid,” though no formal slip rate was defined, and to have occurred along the strike of ~150 km of interconnected extensional faults in the SSR, NSR, Kern Mountains and Deep Creek Range [Miller *et al.*, 1999].

Overall extension on the SSRD has been estimated at 8 to 24 km based on a retrodeformable cross section constructed by McGrew [1993]. The ~17 Ma period of extension documented by the ApFT data is thought to have accommodated ~15 km of slip on the SSRD based on an assumed high-angle fault geometry and a 35 °C km⁻¹ geothermal gradient [Miller *et*

al., 1999]. No Cenozoic slip rate has been determined for the SSRD by previous research. This study combines previously collected ApFT/ZrnFT data and new zircon and apatite (U-Th)/He data with finite element modeling to better understand the overall timing, magnitude, and rates of extension in the SSR during the Cenozoic.

4. (U-Th)/He Thermochronology

ZrnHe and ApHe thermochronology has been applied to a variety of tectonic settings to understand near surface and upper crustal (<10 km) processes [e.g., *House et al.*, 1998; *Stockli et al.*, 2000; *Farley*, 2002; *Ehlers and Farley*, 2003; *Reiners*, 2005; *Stockli*, 2005; *Colgan et al.*, 2006; *Flowers et al.*, 2008; *Schildgen et al.*, 2009a; *Colgan et al.*, 2010; *van Soest et al.*, 2011; *Styron et al.*, 2013]. These thermochronometers can be used to determine when a sample cooled below a specific temperature (i.e., closure temperature) [*Dodson*, 1979] or temperature range (i.e., helium partial retention zone, HePRZ) [e.g., *Wolf et al.*, 1998]. The ZrnHe thermochronometer has a HePRZ of 140-200 °C [*Wolfe and Stockli*, 2010], and a closure temperature that ranges from 175-193 °C given a cooling rate of 10 °C m.y.⁻¹ for typical grain sizes [*Reiners*, 2005]. The ApHe system has a HePRZ between ~40-80 °C [*Wolf et al.*, 1998; *House et al.*, 1999; *Stockli et al.*, 2000], and has a closure temperature of ~75 °C [*Farley*, 2000]. Assuming a conservative geothermal gradient of 30 °C km⁻¹ for the NBR during the Cenozoic, the ZrnHe and ApHe thermochronometers would record exhumation of upper crustal rocks from ~6.7 to 1.3 km depth. These low-temperature thermochronometers are thus powerful tools for understanding the exhumation of lower plate rocks of MCC in the upper crust.

Ten rock samples were collected for ZrnHe and ApHe analysis from the Jurassic SCWC intrusion [*Lee and Christiansen*, 1983] at ~1-1.5 km intervals along an almost 10 km long horizontal transect roughly parallel to the ESE slip direction of the SSRD [*McGrew*, 1993]

(Figure 2.1b). *Stockli* [2005] outlined this sampling strategy for low-temperature thermochronometers in extensional tectonic settings to determine the magnitude of extension and fault slip rates.

4.1 (U-Th)/He Results

Mineral separation and single-grain (U-Th)/He analyses were completed in the Group 18 Laboratories (NG³L) at Arizona State University using techniques similar to those described by *Schildgen et al.* [2009a and 2009b] and *van Soest et al.* [2011]. Raw zircon and apatite (U-Th)/He dates were corrected for the loss of ⁴He in the outer ~20 μm of the mineral structure (alpha ejection correction) using standard methods from *Farley et al.* [1996], *Farley* [2002], and *Hourigan et al.* [2005]. Individual dates for 44 zircon and 11 apatite crystals are reported in the supplementary data tables A1.1 and A1.2 with uncertainties based on analytical imprecision alone; the error-weighted mean dates for sets of zircon or apatite analyses from each sample are shown in Table 2.1. In many cases, the dispersion of ZrnHe or ApHe dates from a single sample exceeded the variation that might be expected given the magnitude of analytical uncertainties. As a result, for each ensemble of ZrnHe or ApHe dates of a sample, clear outliers were determined using the Hampel identifier, as described by *Pearson* [2011], assuming a threshold value of 4. Any outliers determined by this method were rejected and the weighted mean was recalculated. Final dispersions were evaluated using mean squared weighted deviation (MSWD) [*Wendt and Carl*, 1991]. For groups of dates without excess dispersion, the uncertainties reported in Table 2.1 represent two standard deviations of the error-weighted mean ($2\sigma_{wm}$) based on the propagation of analytical uncertainties alone. For groups of dates with excess dispersion, the calculated $2\sigma_{wm}$ values were multiplied by the square root of the MSWD and the result was reported as an expanded uncertainty $2\sigma_{exp}$ in an attempt to account for the scatter. The reported

uncertainties do not take into account natural zoning of U and Th isotopes within the crystal lattice [e.g., *Hourigan et al.*, 2005].

4.1.1 Zircon (U-Th)/He Results

We obtained ZrnHe dates for all ten rock samples. The dates range from 40.7 ± 4.9 Ma for a sample collected near the western end of the horizontal transect to 21.0 ± 3.3 Ma for a sample closest to the SSRD trace (Table 2.1; Figure 2.1c; Figure 2.2). The distribution of ZrnHe dates in the SSR is bimodal, with a cluster of Eocene dates (37.0 ± 5.4 to 41.5 ± 2.4 Ma) in the western portion of the transect, and an abrupt transition to Oligocene dates (21.0 ± 3.3 to 26.4 ± 3.9 Ma) in the central to eastern portion of the transect (Figure 2.1c; Figure 2.2). The Eocene population shows no apparent age progression from west to east. However, the Oligocene dates show a systematic decrease in the direction of extension, with the youngest dates coming from samples collected closest to the trace of the SSRD (Figure 2.1c; Figure 2.2).

Nine of the ten weighted mean dates are overdispersed as shown by greater than anticipated MSWD values [*Wendt and Carl*, 1991]. All ZrnHe dates were evaluated for correlations with effective uranium concentration (eU) to assess if radiation damage may have contributed to dispersion of replicate dates (Table A1.1) [e.g., *Reiners*, 2005; *Guenther et al.*, 2013]. A single aliquot 12WC02 z03 was found to have a high eU and a significantly younger date compared to the other 12WC02 replicate analyses. However, this replicate was excluded from the error-weighted mean date based on the outlier identification method (Table 2.1; Table A1.1). No other samples showed a significant range in eU values with a corresponding correlation to ZrnHe dates; as a result, radiation damage is not considered to be a major factor in the overdispersed dates. Instead, this overdispersal may be the result of parent isotope zonation within the zircon crystals, which was shown by *Hourigan et al.* [2005] to contribute to

overdispersed ZrnHe dates. Although zircons with obvious optical zoning were not chosen for analysis, it was impossible to completely avoid zoned grains since non-acicular zircons in the SCWC commonly exhibit some zonation [Lee *et al.*, 1968]. This is considered to be the most likely cause of the overdispersed ZrnHe dates.

4.1.2 Apatite (U-Th)/He Results

Only three samples yielded apatite grains suitable for (U-Th)/He dating (Table 2.1). All three were collected in the central to eastern portion of the footwall transect. ApHe dates from the three samples decrease from 15.1 ± 2.4 Ma in the central portion of the transect to 13.6 ± 0.7 Ma closest to the SSRD (Figure 2.1c; Figure 2.2). In the western section of the transect a previous study documented ≤ 0.02 wt. % apatite present in the intrusion [Lee *et al.*, 1973], and the few apatites observed contained inclusions, rendering them unfit for conventional ApHe analysis [e.g., Wolf *et al.*, 1996]. Only the ApHe dates from sample 12SC03 exhibit significant overdispersion, and this is most likely due to unrecognized inclusions containing U, Th, or Sm. None of the ApHe samples showed a large range in eU values among replicate analyses (Table A1.2). Therefore, radiation damage is not considered to be a major factor in the overdispersed dates as observed in other ApHe date populations [e.g., Shuster *et al.*, 2006; Flowers *et al.*, 2009].

4.2 Thermochronologic Data Interpretation

Ranges of denudation rates were estimated for the SSR using (U-Th)/He and fission track samples that were dated by multiple thermochronometers ($n=6$). We used these rates to assess the relative influences of erosional and tectonic denudation in the SSR. For the (U-Th)/He data, denudation rates were calculated from samples 12SC03, 12SC05, and 12SC07 (Table 2.1) [e.g., Reiners and Brandon, 2006]. The previously published ZrnFT and ApFT data for samples

93SRFT-29, 93SRFT-30, and 93SRFT-31 from *Miller et al.* [1999] were also used to estimate denudation rates in the same manner. The *Reiners and Brandon* [2006] method assumes nominal closure temperatures for each thermochronometer (ZrnFT: 240 °C, ZrnHe: 180 °C, ApFT: 110 °C, ApHe: 65 °C; 10 °C Myr⁻¹ cooling rate) when determining cooling rates, and assumed steady-state geothermal gradients to calculate denudation rates.

Minimum and maximum cooling rates were calculated for each sample based on the errors of each date. For example, 12SC03 has a minimum calculated cooling rate of 4.05 °C Myr⁻¹ and a maximum cooling rate of 5.27 °C Myr⁻¹. Although these cooling rates are less than 10 °C Myr⁻¹, as assumed for the nominal closure temperature, the ~5-6 °C difference does not significantly change the closure temperature of either system for typical grain sizes [e.g., *Reiners*, 2005]. The cooling rate minimum, average, and maximum values were then divided by a range of geothermal gradients from 10-50 °C km⁻¹. These calculations lead to an estimated minimum denudation rate of 0.08-0.4 km Myr⁻¹ for sample 12SC03. This analysis was completed for all six samples, and the range of denudation rates for the SSR is 0.08-2.25 km Myr⁻¹. Two samples (12SC03 and 93SRFT-29) with Eocene ZrnHe and ZrnFT dates, closest to one another in the range, were used to calculate Eocene denudation rates between 0.15 and 6.35 km Myr⁻¹.

These calculated denudation rates are 16 to 1270 times greater than the present day median global outcrop erosion rate of 0.005 km Myr⁻¹ [*Portenga and Bierman*, 2011]. Although the median outcrop erosion rates from *Portenga and Bierman* [2011] are only calculated for the present, the significantly higher denudation rates estimated for the SSR suggest that even if erosion rates were higher in the past (e.g., during a warm Eocene climate) unreasonably higher rates would be necessary to attribute the majority of denudation in the SSR to erosional processes. As a result of this comparison, erosional denudation is assumed to be negligible, and

the majority of exhumation is considered to be of tectonic origin for the SSR.

The ZrnHe and ApHe cooling ages for the SSR are progressively younger in the extension direction, as expected for exhumation along a normal fault (Figure 2.2) [e.g., *John and Foster*, 1993; *Wells et al.*, 2000; *Stockli*, 2005]. The observed age distribution in the central and eastern part of the transect is consistent with exhumation due to unroofing by extension along the SSRD during the Oligocene starting at ~26-25 Ma, and continuing into the Miocene to at least ~13.6 Ma based on the youngest ApHe age in the transect. The mechanism for Eocene cooling of the western portion of the transect below ~140 °C is less clear from these data alone. The onset of extension interpreted from the ZrnHe data is 8 to 9 m.y. older than a previous estimate for movement along the SSRD from ApFT data [*Miller et al.*, 1999]. This difference in minimum age for the onset of extension is a function of the higher closure temperature of the ZrnHe system in comparison to the ApFT system.

A one-dimensional paleodepth reconstruction [e.g., *Stockli et al.*, 2003] of the available low-temperature thermochronologic data was completed using the retrodeformable cross section of *McGrew* [1993] (Figure A1.1). Difficulties in quantifying the errors associated with the paleodepth reconstruction, and a lack of definable age-depth relationships does not allow for direct interpretation of the timing and rates of exhumation in the SSR. Instead, to better understand the extension history of the SSR based on our new data and previously published ZrnFT and ApFT data, a Pecube [*Braun*, 2003; *Braun et al.*, 2012] modeling approach was used.

Pecube is an ideal tool to investigate the tectonothermal history of the SSR, as it is well suited to modeling multiple-sample thermochronological datasets given relatively simple deformational scenarios. In particular, the relatively time-invariant fault geometry of the SSRD at depth [*McGrew*, 1993] avoids Pecube's limitations on time-varying fault geometry.

Furthermore, the nature of our dataset (~30 footwall thermochronometer ages, with few samples yielding multiple ages from multiple thermochronometers) makes it more suitable for an analysis tool that exploits the spatial and structural relationships between samples to constrain the time-temperature-exhumation history of the samples, rather than a tool that emphasizes single-sample, multiple-thermochronometer analysis such as HeFTy [Ketcham, 2005].

5. Thermochronologic Modeling

We reconstruct the extensional history of the SSR through a Bayesian inversion incorporating the thermokinematic modeling program Pecube as well as structural estimates for total strain and fault slip [e.g., McGrew, 1993] using methods derived from Styron *et al.* [2013]. The inversion essentially takes random tectonothermal histories for the SSR, filters them so they are within structural constraints (section 5.2.1), uses Pecube to predict thermochronometric ages for each history, and selects posterior histories based on the goodness of fit between the predicted and observed thermochronometer ages. This process yields joint posterior probability distributions for the thermal and tectonic variables in the inversion.

The Bayesian approach to inversion for continuous model variables is well described mathematically [e.g., Sambridge, 1999; Sambridge and Mosegaard, 2002; Tarantola, 2005] but here we focus on a procedural description, and use mathematical descriptions as an aid rather than as the most compact description of the process. Bayesian inversion or inference involves taking initial estimates of probability distributions for each variable of interest, and then refining those estimates based on how well predictions made by the variables compare to observations. The initial estimates are called 'prior probabilities' or simply 'priors,' and the refined probabilities are known as 'posterior probabilities.' Whether a distribution is a prior or posterior distribution is solely based on whether it will be refined in the inversion step at hand, and in many instances the

posteriors for one inversion step form the priors for another. However, in our methods this iteration does not happen.

The priors map to the posteriors through another distribution called the ‘likelihood,’ which encapsulates the goodness of fit between the model predictions and the observations. This is summarized by Bayes' rule:

$$p(T | D) \propto p(T)p(D | T) \quad (1)$$

where $p(T)$ is the prior probability distributions for all variables in T (in our case, variables that represent the thermal and strain history); $p(T | D)$ is the posterior probability distributions, i.e., the probability distributions of the variables T given the data D ; and $p(D | T)$ is the likelihood, i.e., the probability of observing the data D given that the parameters T are true.

5.1 Pecube Model Setup

The Pecube finite element model (FEM) covers the entirety of the SSR, with an areal distribution of 119 km E-W by 32 km N-S. The upper surface of the model is the modern topography, taken from SRTM data [Farr *et al.*, 2007]. Topographic evolution is modeled as steady-state across the FEM. The model extends to 30 km depth, based on the present day distance to the Moho in the Snake Range [Gans, 1987]. Node spacing in the FEM mesh is 900 m in the x , y , and z directions. The FEM has two faults, the SSRD and Wheeler Peak Fault (WPF) (Figure 2.3). The retrodeformable cross section of McGrew [1993] suggests the fault geometries of the SSRD and WPF remain relatively constant throughout extension. The geometries of the faults in the subsurface for the model are taken from McGrew [1993]. The mineral elongation of mylonites exposed in the eastern SSR documented by McGrew [1993] was used to define the slip direction of the SSRD at 105° and a generalized strike for the structure at 015° . This inferred strike is similar to a generalized strike of 007° calculated based on a corrugation axis of the SSRD from

mapping of *McGrew et al.* [1995]. The Pecube software does not allow for lateral or temporal changes in fault geometry. The strike orientation of the SSRD in the east-central SSR (closest to the measured mineral elongations) must be extrapolated to the northern and southern portions of the range. As a result, the modeled trace of the SSRD farther away from the east-central portion of the range is less representative of the mapped trace of the SSRD.

Pecube uses several variables to calculate the 'steady-state' geothermal gradient in the FEM, which is then perturbed by tectonic deformation; variables used to define this are the temperatures at the model surface and base (the Moho in our FEM), thermal diffusivity, atmospheric lapse rate, and radiogenic heat production. We fix the FEM surface temperature, thermal diffusivity, and atmospheric lapse rate, values that are reasonably well constrained relative to the Moho temperature and radiogenic heat production. The Moho temperature and radiogenic heat production are solved for in the inversion. Table 2.2 lists the values for all fixed parameters in the model.

5.2 Construction of Priors

The initial step in the inversion is construction of geologically reasonable priors. In order to solve for both the coupled strain history and thermal state of the crust, representative model variables were defined (Table 2.2).

The strain history of the SSR is separated into independent histories for the SSRD and WPF. These histories are then discretized into several time intervals with different slip rates. The time boundaries of each slip interval and the slip rates for each interval are all randomly sampled from uniform probability distributions.

Slip on the SSRD has four intervals between 80 and 5 Ma, with the beginning and end points for the entire slip history occurring anywhere in this interval, and possible slip rates

between 0-10 mm a⁻¹ at any time. Note that successive intervals are allowed to have the same slip rate, so substantial changes in slip rate are not enforced between intervals.

Direct evidence (i.e., cross cutting relationships) to define the boundaries for onset and completion of extension on the SSRD are poor, and previous work largely inferred the slip history of the SSRD from thermochronologic data [e.g., *Lee et al.*, 1970; *Lee et al.*, 1980; *Miller et al.*, 1988; *Miller et al.*, 1999]. The most direct evidence for timing of motion along the SSRD comes from the ~36 Ma Young Canyon-Kious Basin pluton [*Miller et al.*, 1988] which contains both mylonitic and cataclastic deformation features that are interpreted to be a result of motion along the SSRD [*McGrew*, 1993]. *Armstrong* [1972] also interpreted an Oligocene age of motion based on a normal fault mapped as cross cutting Oligocene volcanic strata of the Needles Range Group [*Whitebread*, 1969; *Best and Grant*, 1987] that was interpreted to either merge into or was truncated by the SSRD. *Miller et al.* [1999] described fanglomerates on the eastern edge of the SSR that contain Oligocene aged volcanic clasts and interpreted these strata as deposits directly related to extension on the SSRD after the Oligocene. Although these relationships point to an Oligocene age and younger period of extension on the SSRD they do not preclude pre-Oligocene periods of extension on the SSRD. The Eocene ZrnHe dates from the eastern portion of our transect suggest extension may have begun prior to the Oligocene. Therefore, a maximum age for extension on the SSRD is set at 80 Ma, based on the timing of Cretaceous metamorphism recorded in the Pole Canyon-Can Young Canyon pluton at ~79.7-79.1 Ma [e.g., *Lee et al.*, 1970, 1986; *McGrew*, 1993].

Three intervals of slip between 40 and 0 Ma were defined for the WPF. Slip rates at any time on the WPF were defined between 0 and 4 mm a⁻¹. The WPF is active, defining the lower age bound, and has a slip rate of < 0.2 mm a⁻¹ [*Sawyer*, 1998; *U.S. Geological Survey and*

Nevada Bureau of Mines and Geology, 2006]. McGrew [1993] also included either this structure, or a similarly oriented structure, in an intermediate stage of extension in the SSR; as a result, an intermediate age in the range for slip history of the SSRD (40 Ma) was chosen as an upper age bound. Fewer modeled intervals of slip are used for the WPF due to its shorter extensional history in comparison to the SSRD. Similar to the SSRD, these intervals allow variability within the model.

Moho temperatures were varied between 600-1100 °C, and radiogenic heat production from 5-50 °C Ma⁻¹. These broad ranges were chosen because these parameters are not well constrained for the SSR; however, they combine to yield upper-crustal geothermal gradients of 20-55 °C km⁻¹, bracketing Tertiary estimates for the Basin and Range [e.g., *Foster and John*, 1999; *Stockli et al.*, 2002; *Gorynski et al.*, 2013; *Long et al.*, 2015]. The combination of these thermal parameters with the strain history variables yields a prior distribution $p(T)$, where T is the set of probability distributions for each variable t in T . Each $p(t)$ is independent of the others.

5.2.1 Filtering of Priors to Fit Structural Constraints

When constructing $p(T)$, we chose probabilities $p(t)$ for each t that are individually reasonable (or at least possible) and considered independent. However, many combinations of the variables yield extension histories that violate constraints from geologic cross sections by producing unreasonable magnitudes of net extension. Therefore, we only considered the subset of $p(T)$ that is consistent with geological constraints, which we call $p(T | G)$, or the probability of T given geological constraints G . From a practical perspective, by reducing $p(T)$ to a much smaller, or much more sparse $p(T | G)$ before the computationally-intensive Pecube modeling, the total

computation times may be reduced by one or two orders of magnitude with no loss of statistical robustness, as $p(t | G)$ may be very similar to $p(t)$ for any t .

A very effective way to reduce $p(T)$ to $p(T | G)$ is to filter samples from $p(T)$ that predict net extension outside of acceptable bounds determined by geologic cross sections [e.g., *Styron et al.*, 2013]. We arithmetically calculate the net extension for each sample of $p(T)$ given fault dips from the FEM and strain history variables from the $p(T)$ sample and accept into $p(T | G)$ only those with net extension values between 8 and 35 km. This estimate is in part based on the 8-24 km of allowable extension from a non-unique retrodeformable cross section that assumes a specific SSRD upper plate geometry and a footwall cutoff in the Cambrian Pole Canyon Limestone [*McGrew*, 1993]. The total allowable extension was increased from 24 to 35 km so the model would not be overly constrained by a single interpreted cross section; however, the models were not forced to a total of 35 km of extension. We iteratively sampled and filtered $p(T)$ until $p(T | G)$ had 9999 samples, which were then run in Pecube.

5.3 Calculating Likelihood with Pecube

We use Pecube to predict thermochronometer ages at our sample locations, in order to calculate $p(D | T)$. Pecube models were run on the Eureka cluster at the National Supercomputing Center for Energy and the Environment at the University of Nevada, Las Vegas. Each model took between 0.5 to 2.5 hours to compute. Parallelization of about 100x allowed us to run the ~15,000 CPU hours of computation in a little over a week. Out of 9999 jobs, 18 (0.2%) finished with errors, and therefore the total number of runs considered is 9981.

We evaluate each model from $p(T | G)$ by calculating the relative model likelihood $p(D | T)$ using the equation

$$p(D | T) = \frac{\exp(-\chi^2)}{\exp(-\chi_{\min}^2)} \quad (2)$$

where χ^2 is the goodness-of-fit statistic for normally-distributed data

$$\chi^2 = \frac{1}{N} \sum_{i=1}^N \frac{(\mu_i - \hat{\mu}_i)^2}{\sigma_i^2} \quad (3)$$

μ is the error weighted-mean date, $\hat{\mu}$ is the modeled age, and σ_{wm} is the standard deviation of the weighted mean. Since the constant of proportionality in equation (1) is unknown, we normalize $p(D | T)$ relative to the best-fitting model [Tarantola, 2005].

5.4 Posterior Sampling

Once the relative likelihoods were calculated for each model, we calculated the posterior $p(T | D)$, or 'sampling the posterior' in Bayesian terminology, by selecting models from $p(T | G)$ proportional to their likelihood [e.g., Mosegaard and Tarantola, 1995]. In practice this is done through selection of models whose likelihood is larger than a number randomly sampled from the uniform distribution [0,1). This random number is independently generated for each comparison.

5.5 Model Results

$p(T | D)$ contains 39 models out of 9981 considered. Figure 2.4 shows the observed and modeled ages plotted by longitude (a good proxy for down-dip distance on the SSRD). These plots show that the model ages match measured dates within 2σ in most cases, except for three ApFT and two ZrnHe samples. It is possible that unrecognized complications in the fault geometries (e.g., corrugations, fault splays, etc.) of the SSRD and WPF were not represented in Pecube causing the modeled ages to not accurately represent measured ages. However, it is also possible that the measured values were themselves spurious results. The three ApFT samples were interpreted as only partially reset [Miller *et al.*, 1999], and the two ZrnHe samples have

unacceptably high MSWD_{wm} values. Despite these misfits, overall the modeled ages and measured thermochronologic ages are generally in good agreement.

The posterior distribution $p(T | D)$ is the complete solution to a Bayesian inverse problem. However, because of the multivariate nature of $p(T | D)$, we transformed the strain variables into extensional histories in order to describe and make inferences from them (Figure 2.5).

The results indicate that extension in the SSR starts during the Eocene at ~50-45 Ma (Figure 2.5a and 2.5b). Extension rates begin to increase in the SSR at ~50 Ma (Figure 2.5a). However, the median and mean onset of extension for the 39 best-fit models is ~45 Ma. Cumulative extension in the SSR by the Eocene-Oligocene boundary (Figure 2.6a) shows a slightly bimodal distribution, with 23 of the 39 fits requiring greater than 2 km of extension prior to the Oligocene. The mean amount of extension accumulated prior to 34 Ma is 5.8 km, with a range of 0.9-9.8 km of extension over the central 50% of results (25th to 75th percentile interval; Figure 2.5b). Extension rates during the Eocene are generally slow at ~0.5 mm a⁻¹ (Figure 2.5a). However individual modeled histories show variability in the extension rate with some results showing periods of extension with rates as high as 6 mm a⁻¹ (Figure 2.5a). Despite these low rates of extension, we regard this phase as likely responsible for producing the Eocene cooling of the higher-temperature and highest-elevation thermochronometers along the western end of the transect.

Following the inferred onset of extension in the Eocene, the model results show low extension rates from ~38 to ~33-30 Ma, where all but one modeled history show extension at rates of < 0.5 mm a⁻¹ (Figure 2.5a). Modeled extension rates increased again in the early Oligocene, and remained at levels comparable to the Eocene extension rates until the Oligocene-

Miocene boundary. Although the overall rate of extension from ~50-45 to 38 Ma and from ~33-30 to 23 Ma was rather slow, it was significant enough to produce cumulative extension of ~10-18 km for most modeled histories by 23 Ma (Figure 2.6b). The mean cumulative extension of all model fits is 11.3 km, with a range of 6.7-15.5 km over the central 50% of modeled histories for net cumulative extension at the Oligocene-Miocene boundary. This period of extension is inferred to be responsible for the Oligocene ZrHe cooling ages observed in the SSR.

Modeling results further suggest that the significant but relatively slow extension during the Eocene and Oligocene was followed by a period of more rapid extension during the Miocene. The most rapid extension rates occur at ~16.5 Ma (Figure 2.5a); however, a histogram of modeled extension rates at 16.5 Ma (Figure 2.6c) shows about half of the model fits have extension rates of $\leq 1 \text{ mm a}^{-1}$. Some individual models show more rapid extension rates of 6 and 8 mm a^{-1} , although most do not show rates greater than 3.5 mm a^{-1} . At that time, the WPF may have begun to extend at extremely low rates (Figure 2.5c). This fault may have initiated as early as ~20 Ma, and the modeling results indicate extension started by ~10 Ma (Figure 2.5c). The modeled extension rates on the WPF increased steadily after 10 Ma, but remain very low at $\leq 0.3 \text{ mm a}^{-1}$ until present day (Figure 2.5c).

Overall modeled cumulative net extension in the SSR ranged from 19.8-34.9 km. Figure 2.6d shows that most results have cumulative net extension amounts at the higher end of that range. The central 50% of results have a range of 27.5-32.3 km of cumulative net extension, and a mean cumulative net extension of 29.7 km. The contribution of WPF to cumulative net extension is minor, with a mean extension amount of 2.8 km and a total range of 1.5-3.9 km for all modeled histories (Figure 2.5d).

5.6 Relationships Between Model Variables and Results

No single variable is strongly correlated with model likelihood, and therefore no variable strongly influences the results. Additionally, the posterior variables $p(T | D)$ are poorly correlated, which seems to indicate that the results are essentially random. However, inspection of the results in terms of ‘metavariables’ (i.e., combinations of input variables that better characterize the system) show data patterns, although due to the high dimensionality of the system, some scatter still exists in many plots. This is illustrated in Figures 2.5 and 2.7. For example, Figure 2.5a, the extension rate history for the SSR, shows that throughout the Miocene, when the majority of extension occurred, there is an order of magnitude variation in posterior slip rates. However, Figure 2.5b shows that during the same time, the cumulative exhumation is much more tightly bracketed. The magnitude of cumulative exhumation, combined with the geothermal gradient, directly controls whether a given thermochronometric sample has passed through its thermal sensitivity window (partial retention or partial annealing zone). As a result, the timing of cumulative exhumation is more important for determining cooling ages than the rate at which the samples cool through this window. Additionally, the individual slip rates are generally more ephemeral and noisy than the cumulative extensions. Similarly, Figure 2.7 shows that the posteriors display more structure (e.g., linear relationships, clustering) when metavariables are plotted (Figure 2.7d-f) rather than the Pecube input variables (Figure 2.7a-c).

5.6.1 Relationship Between Crustal Heat and Deformation

The model results are not sensitive to particular values for the Moho temperature or radiogenic heat production. However, the results are sensitive to the geothermal gradient, which is a function of both of these variables. More specifically, a tradeoff exists between the geothermal gradient and the minimum amount of extension on the SSRD necessary to exhume

all thermochronometers from below their partial retention or annealing zones. This is illustrated in Figure 2.7d: below the dashed line, no posteriors are present; however, above the dashed line, the posteriors are somewhat evenly distributed, indicating this threshold. Because the posteriors plot above a line, rather than on a line, we interpret this to be a threshold effect rather than an optimal combination of variables.

6. Discussion

The new (U-Th)/He thermochronologic results combined with fission track data from *Miller et al.* [1999] and Pecube modeling suggest three significant periods of extension occurred during the Neogene and Paleogene for the SSRD and WPF (Figure 2.8): (1) ~50-45 to ~38 Ma (Eocene), (2) ~33-30 to ~23 Ma (Oligocene), and (3) ~23-20 to ~10-8 Ma (Miocene). These periods of extension were defined based on clusters of increased extension rates of individual modeling histories (see Figure 2.5), and does not imply extension occurred continuously in the SSR during each of the periods. These periods of extension are considered largely driven by tectonic rather than erosional processes based on the denudation rates discussed in section 4.2.

The first two periods of extension most likely occurred on the SSRD and related upper plate structures, while the third period of extension was probably accommodated on both the SSRD and WPF. A younger period of extension during the Miocene, possibly starting at ~10-8 Ma, continuing to present day occurs solely on the WPF (Figure 2.5), an active range bounding normal fault [*Sawyer*, 1998; *U.S. Geological Survey and Nevada Bureau of Mines and Geology*, 2006]. However, the contribution of this period to the overall extensional history of the SSR is minor.

Our modeling results suggest that extension in the SSR could be accommodated, at least in part, on a structure with a dip similar to the SSRD of *McGrew* [1993]. Extension in the SSR

has previously been interpreted to occur on a high-angle normal fault during the Miocene that subsequently rotated to the present day low-angle orientation of the SSRD [Miller *et al.*, 1999]. Our modeling results suggest that tectonic denudation by a low-angle detachment, as shown in the McGrew [1993] cross section, also matches the observed distribution of cooling ages. However, our methodology does not preclude the interpretation of Miller *et al.* [1999] because it does not explicitly address the possibility of variable fault geometries (e.g., rotation of fault planes) through time.

Modeled extension in the SSR appears to have been relatively slow throughout much of its history. Despite relatively slow rates, mostly $< 1 \text{ mm a}^{-1}$, extension produced a mean cumulative net extension of 29.7 km. Our modeled magnitude of extension in the SSR is higher than the ~15 km of Miller *et al.* [1999] (only estimated for the Miocene) and similar to the upper end of the 8-24 km range for the Cenozoic from McGrew [1993]. The discrepancy between our estimate of total net extension and Miller *et al.* [1999] is likely due to significant pre-Miocene extension in the range. Our cumulative net extension estimate for the WPF, 2.8 km, is in good agreement with first-order extension estimates based on an assumed planar high-angle normal fault and depth to basement in Spring Valley from gravity data [Maniken *et al.*, 2007].

6.1 Extension in the SSR and NSR

An Eocene period of extension is documented in the NSR by Lee [1995] from ~48-41 Ma, similar to the first period of SSR extension. The similarities in timing of extension in the SSR and NSR suggest that the NSRD and SSRD have been intimately linked structures since the Eocene, rather than strictly during rapid extension in the Miocene [e.g., Miller *et al.*, 1999]. Lee [1995] only reported cooling rates in the NSR, and as a result it is impossible to compare rates of extension between the NSRD and SSRD. However, the NSR was significantly more deformed

during Cenozoic extension than the SSR [e.g., *Miller et al.*, 1983; *Bartley and Wernicke*, 1984], and it is reasonable to assume that extension rates were faster in the NSR than those suggested by the Pecube modeling for the SSR.

Based on our modeling, the quiescent period between the first and second period of extension in the Oligocene is coincident with plutonism in the SSR at ~36 Ma [*Miller et al.*, 1988] and volcanic activity in the region [*Gans et al.*, 1989] (Figure 2.8). It also coincides with a period of slow cooling documented in the NSR [*Lee*, 1995].

Modeled rates of extension increased again in the SSR during the Oligocene at ~33-30 Ma and continued until the Miocene (Figure 2.8). This second period of extension has not been previously reported for the SSR, and occurs during major Needles Range Group volcanism associated with eruptions of the Indian Peak Caldera Complex [e.g., *Best and Grant*, 1987; *Best et al.*, 1989; *Best and Christiansen*, 1991]. A similar pulse of Oligocene extension was documented by potassium feldspar MDD modeling [*Lee*, 1995] and by $^{40}\text{Ar}/^{39}\text{Ar}$ and stable isotope analyses of white mica [*Gébelin et al.*, 2011] in the NSR. The similar timing of extension in the NSR and SSR during the Oligocene further substantiates a link between the NSRD and SSRD throughout the Cenozoic.

Our model results show that the most rapid extension in the SSR began during the third extensional period at ~16.5 Ma (Figure 2.8). Rapid extension was previously interpreted by *Miller et al.* [1999] for the greater Snake Range-Deep Creek fault system at ~17 Ma based on ZrnFT and ApFT data. However, our results show that in the SSR there was an increase in extension rates that started during the early Miocene (~23-20 Ma) and extension rates remained relatively high until the middle Miocene (~10-8 Ma). We interpret this to mean that extension in

the SSR occurred over a significantly longer period of time than the short period interpreted by *Miller et al.* [1999].

The mean cumulative net extension for the SSR, 29.7 km, is significantly less than the estimated 60 km of net slip on the Snake Range décollement (NSRD) by *Bartley and Wernicke* [1984]. However, the estimate of slip for the NSRD by *Miller et al.* [1999] is 12-15 km during the Miocene. Our net cumulative extension for the SSR during the Miocene is 15-20 km, only slightly more than estimated for the NSRD by *Miller et al.* [1999].

6.2 Sedimentary Evidence for SSR Extension

Strata preserved within the upper plate of the SSRD corroborate the Eocene and Miocene periods of extension in the SSR suggested by our thermochronologic and modeling results (Figure 2.8). In the southernmost SSR, a ~40 m thick clast-supported conglomerate containing plutonic and carbonate clasts, informally named the Murphy Wash conglomerate, is capped by the ~31 Ma Cottonwood Wash Tuff (unpublished $^{40}\text{Ar}/^{39}\text{Ar}$ age reported by *Miller et al.* [1999]). This conglomerate has been used as evidence for pre-31 Ma extension within the SSR, but the timing was only loosely bracketed as latest Eocene to early Oligocene [*Miller et al.*, 1999]. Our modeling data suggest this period of extension occurred from ~50-45 to 38 Ma, and the extension must have created sufficient topography to act as source for this conglomerate. Furthermore, the plutonic clasts, if they are locally derived from the SSR, requires that extension during the Eocene was of sufficient magnitude to expose one or more of the plutonic bodies presently located in the lower plate of the SSRD at the surface. It seems reasonable that these plutonic clasts were locally derived as they are in an areally-restricted, thin deposit, and clasts are sub-rounded to sub-angular. This relationship between conglomerate deposition and extension in the Eocene suggests that higher estimates for net cumulative extension may be more

reasonable than the modeled lower magnitudes prior to 34 Ma (see higher magnitude population in Figure 2.6a).

During the Oligocene to early Miocene, the Sacramento Pass Basin formed between the SSR and NSR [e.g., *Miller et al.*, 1999]. The increase in extension rates at ~23 to 20 Ma in the SSR is concurrent with interpreted rock avalanche deposits in the basal Sacramento Pass basin stratigraphy [*Martinez*, 2001], suggesting the acceleration in extension rates at ~20 Ma in many of the model results is geologically significant.

6.3 Cenozoic Magmatism and Extension in the SSR

Volcanism in east-central Nevada during the Eocene produced andesitic and rhyolitic lava flows (Figure 2.8) [e.g., *Gans et al.*, 1989]. During the Oligocene to early Miocene voluminous ash flow tuffs erupted from the Indian Peak Caldera complex (Figure 2.8) [e.g., *Best and Grant*, 1987; *Best et al.*, 1989; *Best and Christiansen*, 1991; *Best et al.*, 2013b]. Studies of east-central Nevada volcanism have suggested a spatial and temporal link between the timing of extension and magmatism in the region. *Gans et al.* [1989] interpreted magmatism to have thermally weakened the crust driving the onset of extension, and as a result, the onset of extension in the region was either syn-magmatic or immediately post-magmatic. They documented upper crustal extension in east-central Nevada post-eruption of andesite and rhyolite lavas and ash-flow tuffs, which initiated at ~40 Ma, and argued that extension was concurrent with the eruption of the Kalamazoo Tuff at ~35 Ma [*Gans et al.* 1989]. *Axen et al.* [1993] interpreted the onset of extension in the northern portion of their “eastern-belt of extension” (includes the SSR) to be either syn- or post-volcanism. In contrast, *Best and Christiansen* [1991] and *Best et al.* [2013b] found no evidence for significant, regional scale syn-magmatic extension during Oligocene and early Miocene Needles Range Group volcanism (~31-20 Ma). Our results and interpretations for

the timing of extension show no clear relationship between extension and magmatism in the SSR (Figure 2.8). Extension in the SSR initiates in the Eocene at ~50-45 Ma, based on the modeling results, prior to the east-central Nevada volcanism and extension documented by *Gans et al.* [1989]. Our model interpretations suggest it is either minor or nonexistent during the intrusion of the Young Canyon-Kious Basin pluton at ~36 Ma [*Miller et al.*, 1988], and is significant during and following the eruption of the Needles Range Group [*Best and Grant*, 1987; *Best et al.*, 1989; *Best and Christiansen*, 1991]. If strictly interpreted, none of the temporal relationships expected in this region between extension and magmatism [e.g., *Gans et al.*, 1989; *Best and Christiansen*, 1991; *Axen et al.*, 1993; *Best et al.*, 2013b] are supported by our new data at the scale of the SSR. This absence of a relationship between extension and magmatism at the scale of a single range is not a new interpretation in the NBR; *Taylor* [1990] documented a similar lack of relationship between volcanism and extension at the scale of the North Pahroc and Seaman Ranges. Further, *Axen et al.* [1993] suggested local relationships between extension and volcanism may be variable, with extension initiating prior to volcanism and continuing after volcanism, similar to our interpretations from the SSR. It is possible the SSR is too small scale to record any regionally applicable temporal relationship between extension and magmatism. Larger scale relationships between extension and magmatism are not refuted by our data [e.g., *Axen et al.*, 1993].

6.4 Conceptual Evolution of the SSR

Our new thermochronologic data and Pecube modeling of these data, combined with previously published low-temperature thermochronologic data from *Miller et al.* [1999], allowed us to define three periods of extension in the SSR. A conceptual model for the evolution of the SSR based on these interpretations, and ideas from *Armstrong* [1972], *Miller et al.* [1983; 1988],

McGrew [1993], *Miller et al.* [1999], *Martinez* [2001], and *Long* [2012] is presented in Figure 2.9. This evolutionary model suggests extension began earlier, in the Eocene, than previously interpreted from low-temperature thermochronology or conglomerate deposits in the SSR [*Miller et al.*, 1999]. Although our data do not preclude even earlier, syn-convergence extension, the thermochronologic data and modeling provide no direct evidence for pre-Cenozoic extension in contrast to other portions of the NBR [e.g., *Wells et al.*, 1990; *Hodges and Walker*, 1992; *Druschke et al.*, 2009; *Long et al.*, 2015]. However, our model does incorporate surface breaking extension along the SSRD during the Eocene-Oligocene, based on the cooling of rocks, now exposed at the surface, below ~200-140 °C (ZrnPRZ) during the Eocene. Further, we infer that extension on the SSRD was of sufficient magnitude to exhume a footwall pluton to the surface prior to ~31 Ma (Figure 2.9) based on the presence of plutonic clasts within the Murphy Wash conglomerate. Our modeling corroborates interpretations that extension was more rapid during the Miocene [e.g., *Miller et al.*, 1999], but extension most likely occurred over a significantly longer period of time. Finally, extension on both the WPF and SSRD are responsible for creating the geologic relationships observed in the SSR today (Figure 2.9).

6.5 Regional Context of SSR Extension

Extension in the SSR interpreted from the Pecube modeling is broadly coincident with cooling related to extension in the NSR during the Cenozoic [e.g., *Lee*, 1995]. Extension during the latest Eocene to early Oligocene documented by *Gans et al.* [1989] in east-central Nevada (north of the SSR) overlaps the second period of Oligocene extension in the SSR. Our results and interpretations support coincident extension in the SSR, NSR, Deep Creek Range, and Kern Mountains during the Miocene in agreement with *Miller et al.* [1999]. Previous workers also suggested that the Snake Range décollement (NSRD and SSRD) has a structural link to the

Stampede detachment/Seaman breakaway or these structures form a regional extensional belt [e.g., *Taylor, 1990; Taylor and Bartley, 1992; Axen et al., 1993*]. The timing of extension in the SSR during the Oligocene and Miocene are similar to the periods of extension interpreted by *Taylor [1990]* for the Seaman breakaway; therefore, our new data and models further corroborate a possible structural link between these detachment systems during at least the Oligocene and Miocene. The interpreted periods of extension in the SSR, from our modeling of low-temperature thermochronometers, are also broadly coincident with extension during the Cenozoic in the Raft River-Albion-Grouse Creek MCC and Ruby-East Humboldt MCC [e.g., *Dallmeyer et al., 1986; Saltzer and Hodges, 1988; Mueller and Snoke, 1993; McGrew and Snee, 1994; Wells et al., 2000; Colgan and Henry, 2009; Colgan et al., 2010; Konstantinou et al., 2012*].

Our new data and model interpretations suggest an onset of extension and possible collapse of the Nevadaplano prior to ~17 Ma [e.g., *Colgan and Henry, 2009*]. The new data and model interpretations do not constrain whether the upper crustal extension in the SSR during the Eocene and Oligocene represents extension that directly contributed to the collapse of the Nevadaplano. However, the magnitude of extension by the Oligocene-Miocene boundary in the SSR is between ~10-18 km for most model histories (Figure 2.6b), suggesting a significant amount of extension occurred in this area prior to ~17 Ma. It is possible that the extension in the SSR represents early onset extensional collapse of the eastern Nevadaplano prior to collapse in the western portion of the plateau at ~17 Ma [e.g., *Colgan and Henry, 2009*].

7. Conclusions

The integration of low-temperature thermochronology and Bayesian thermokinematic modeling suggests extension in the SSR was episodic throughout the Cenozoic. These results allowed us to address the five questions initially proposed in this study as follows:

(1) The new thermochronologic data and interpreted modeling results suggest around half of the extension within the SSR occurred pre-Miocene. Eocene and Oligocene extensional magnitudes are significant compared to overall extension in the SSR, and cooling during this time is well documented by the thermochronologic data. This contrasts with *Miller et al.* [1999] who interpreted the majority of extension to be Miocene in age. The rate of extension was relatively low throughout the Cenozoic in the SSR at $< 0.5 \text{ mm a}^{-1}$; however, individual modeling histories suggest periods of rapid extension rates, especially at $\sim 16.5 \text{ Ma}$. These modeling histories are in agreement with the period of rapid extension reported by *Miller et al.* [1999] during the Miocene.

(2) Three significant periods of extension in the SSR were defined based on modeling results at $\sim 50\text{-}45$ to $\sim 38 \text{ Ma}$ (Eocene), $\sim 33\text{-}30$ to $\sim 23 \text{ Ma}$ (Oligocene), and $\sim 23\text{-}20$ to $\sim 10\text{-}8 \text{ Ma}$ (Miocene). These three periods of modeled extension in the SSR are broadly coincident with cooling related to extension in the NSR [e.g., *Lee*, 1995].

(3) The magnitude of extension in the SSR based on modeling ranges from 19.8 to 34.9 km for all modeled histories, and has a mean value of 29.7 km. This total magnitude is slightly higher than the estimate by *McGrew* [1993] based on a palinspastic reconstruction of the SSR. Our estimate for the total magnitude of extension in the SSR is also higher than estimates for the SSRD reported by *Miller et al.* [1999]; however, their estimate only included extension on the SSRD during the Miocene, whereas our estimate is for the entire Cenozoic.

(4) The new and previously published low-temperature thermochronologic data for the SSR are exclusively Cenozoic and thus do not speak to the issue of whether or not there was significant Cretaceous extension in this range as has been suggested for other parts of the NBR. The models were built to permit the possibility of an initiation of extensional activity in the Cretaceous, but the modeling results showed that such an early start is not required by the available low-temperature thermochronologic data.

(5) Overall, the timing of Cenozoic extension in the SSR was similar to Cenozoic extension in the NSR [e.g., *Lee, 1995; Miller et al., 1999*] and in other areas of east-central Nevada [e.g., *Gans et al., 1989; Taylor, 1990*]. Extension and magmatism in the SSR have no clear temporal relationship; however, regional scale relationships [e.g., *Gans et al., 1989; Best and Christiansen, 1991; Axen et al., 1993; Best et al., 2013b*] are not ruled out. Our interpreted periods of extension in the SSR further support a large-scale extensional belt in east-central Nevada during the Oligocene and Miocene stretching from the Stampede detachment/Seaman breakaway, through the SSR, and north to the NSR, Deep Creek Range and Kern Mountains [e.g., *Taylor, 1990; Taylor and Bartley, 1992*]. Given the timing of extension from the Eocene to Miocene in east-central Nevada and magnitude of extension we documented for the SSR, it is possible extensional collapse of the Nevadaplano in this region began well before the ~17 Ma time-frame suggested for the NBR to the west and north of our study area [e.g., *Colgan and Henry, 2009*].

Figures

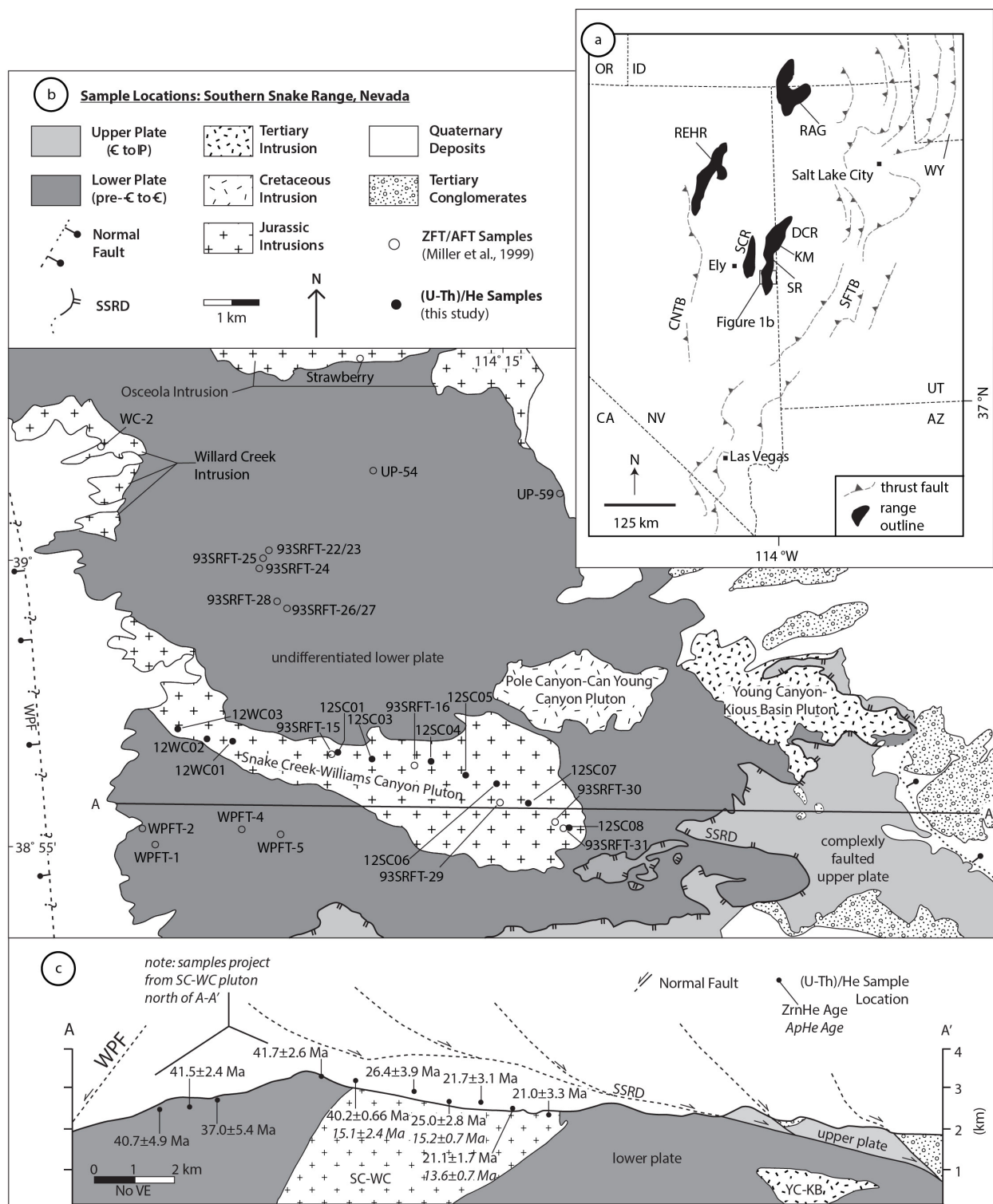


Figure 2.1 Generalized geologic map, sample locations, and cross section

Figure 2.1: Generalized geologic map, sample locations, and cross section: (a) Location of the Snake Range in east-central Nevada between the Central Nevada thrust belt (CNTB) of *Taylor et al.* [2000] and the Sevier fold and thrust belt (SFTB) [e.g., *DeCelles and Coogan*, 2006] (modified from *Miller and Gans* [1989], *DeCelles and Coogan* [2006] and *Long* [2012]). Dashed lines indicate generalized thrust faults, teeth on hanging walls. Dashed and dotted lines are state outlines. Black polygons are generalized range outlines. (b) Simplified geologic map of the central Southern Snake Range showing the location of (U-Th)/He samples (this study) and fission track samples of *Miller et al.* [1999] (map modified from *Whitebread* [1969], *McGrew* [1993], and *Miller et al.* [1999]). Names for intrusions are from *Lee and Christiansen* [1983] and *McGrew* [1993]. (c) Generalized cross section of *McGrew* [1993] for the central Southern Snake Range with (U-Th)/He dates projected into the line of section. Abbreviations: REHR-Ruby Mountain-East Humboldt Range, RAG-Raft River-Albion-Grouse Creek Range, SR-Snake Range, OR-Oregon, ID-Idaho, WY-Wyoming, UT-Utah, AZ-Arizona, NV-Nevada, and CA-California, SSRD-Southern Snake Range Décollement, WPF-Wheeler Peak Fault, SC-WC-Snake Creek-Williams Canyon Pluton, YC-KB-Young Canyon-Kious Basin Pluton, ZrnHe-zircon (U-Th)/He age, ApHe-apatite (U-Th)/He age, VE-vertical exaggeration.

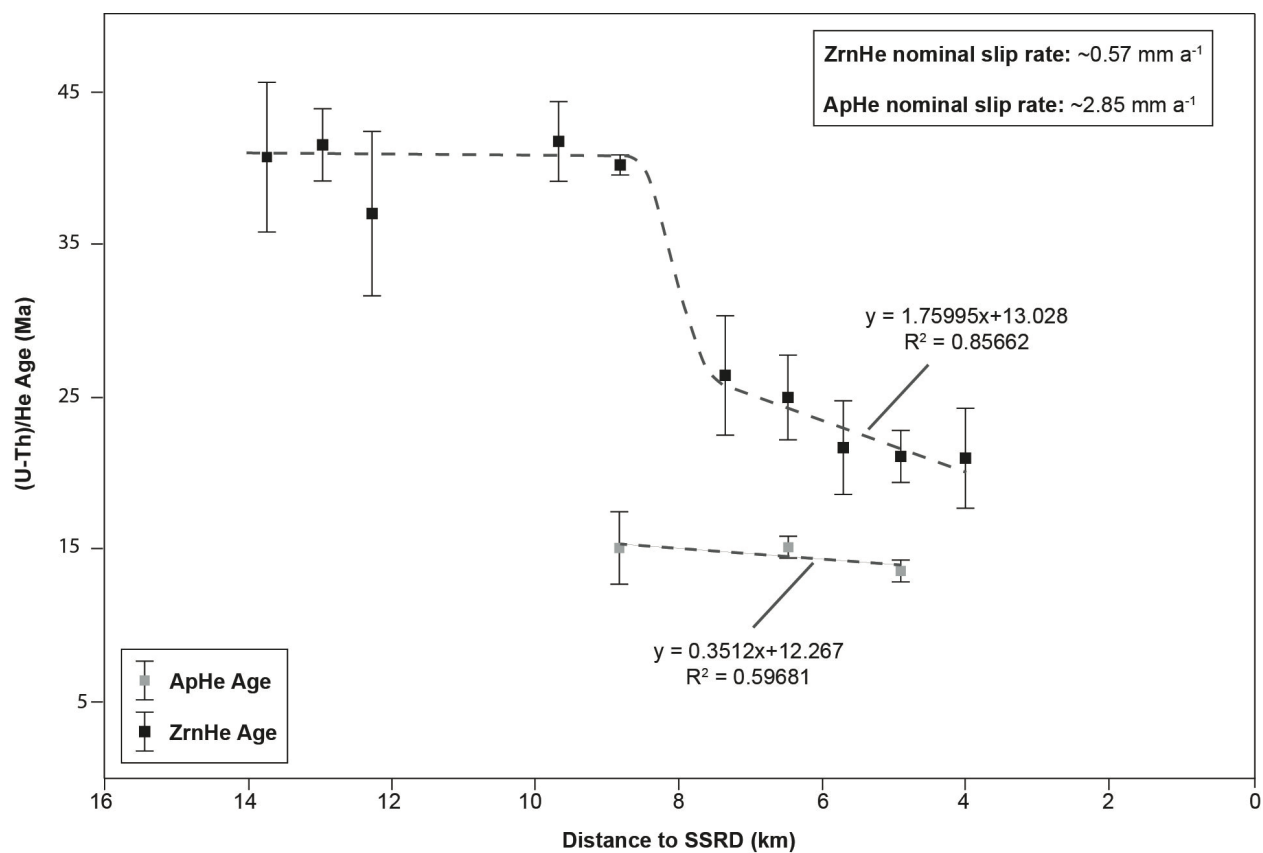


Figure 2.2 Zircon and apatite (U-Th)/He versus distance from the SSRD

Figure 2.2: Zircon and Apatite (U-Th)/He versus distance from the SSRD: Plot of measured zircon and apatite (U-Th)/He age versus distance from the SSRD. Nominal slip rates are calculated using a simple linear regression and inverse of the regression slope [e.g., *Stockli, 2005*]. Equation of linear regression and correlation coefficient are shown. Black dashed line is a visual aid for changes in ages. Age values and error bars are those quoted in Table 2.1. Abbreviations: ZrnHe-zircon (U-Th)/He age, ApHe-apatite (U-Th)/He age.

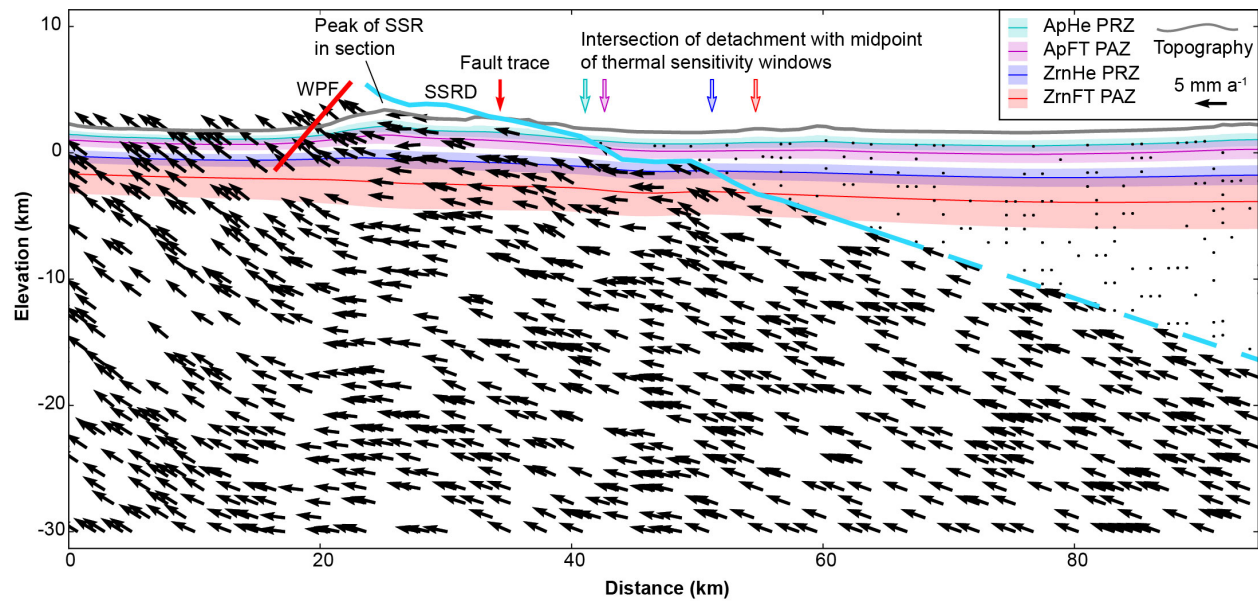


Figure 2.3 Example of model cross section

Figure 2.3: Example of model cross section: East-west oriented cross section example of the Pecube model setup for the SSR. The SSRD geometry in solid blue and WPF geometry in solid red is taken from the *McGrew* [1993] retrodeformable cross section. Dashed blue line is the extrapolated extension of the SSRD to the edge of the model. Vectors indicate velocity of rocks modeled relative to the stable hanging wall. The intersection of the middle of the thermal sensitivity window of each thermochronometer is indicated on the cross section. Abbreviations: SSRD-Southern Snake Range Décollement, WPF-Wheeler Peak Fault, SSR-Southern Snake Range, ApHe PRZ-apatite (U-Th)/He partial retention zone, ApFT PAZ- apatite fission track partial annealing zone, ZrnHe PRZ- zircon (U-Th)/He partial retention zone, ZrnFT PAZ- zircon fission track partial annealing zone.

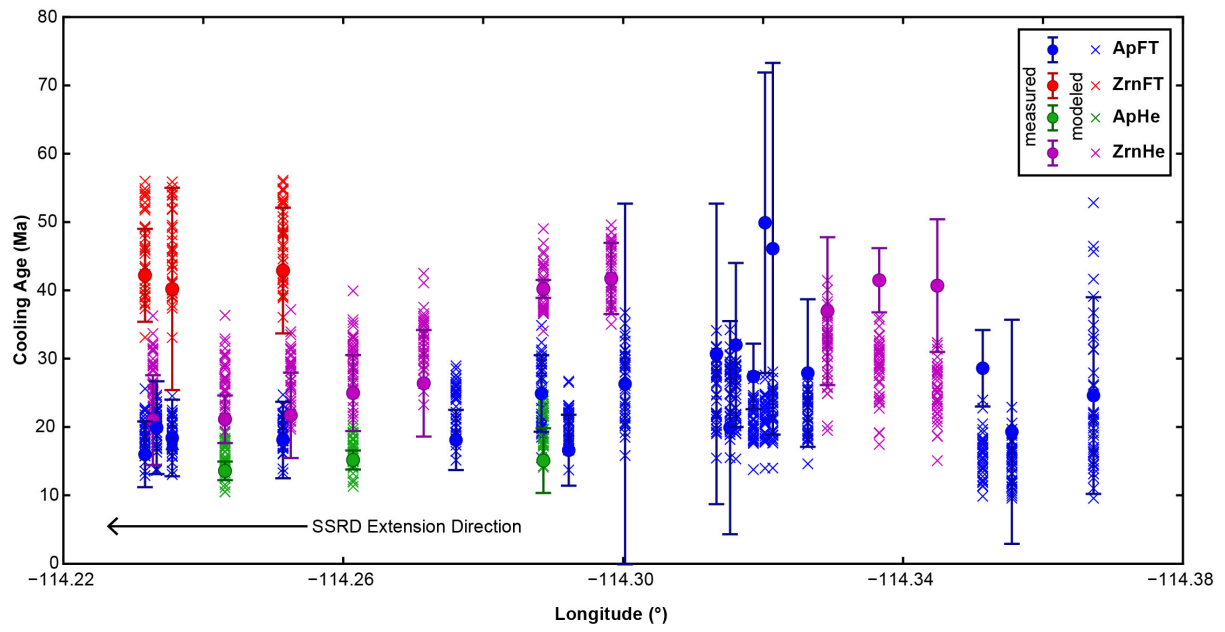


Figure 2.4 Comparison of modeled and measured cooling ages

Figure 2.4: Comparison of modeled and measured cooling ages: Plot of all measured and modeled cooling ages from the posterior distribution versus location in longitude within the SSR. Measured ages for the ZrnFT, ApFT, ZrnHe and ApHe systems are represented by colored circles and error bars (ZrnHe and ApHe: $2\sigma_{wm}$; ZrnFT and ApFT: 2σ). Please see Table 2.1 for ZrnHe and ApHe values and errors and *Miller et al.* [1999] for ZrnFT and ApFT values and errors. Colored ‘x’ symbol represents the modeled cooling age for the 39 best-fit models. The overall agreement between modeled ages and measured ages is relatively good. Please see section 5.5 for a discussion of the ages with poor agreement. Abbreviations: ZrnFT-zircon fission track age, ApFT-apatite fission track age, ZrnHe-zircon (U-Th)/He age, ApHe-apatite (U-Th)/He age, SSRD-Southern Snake Range Décollement.

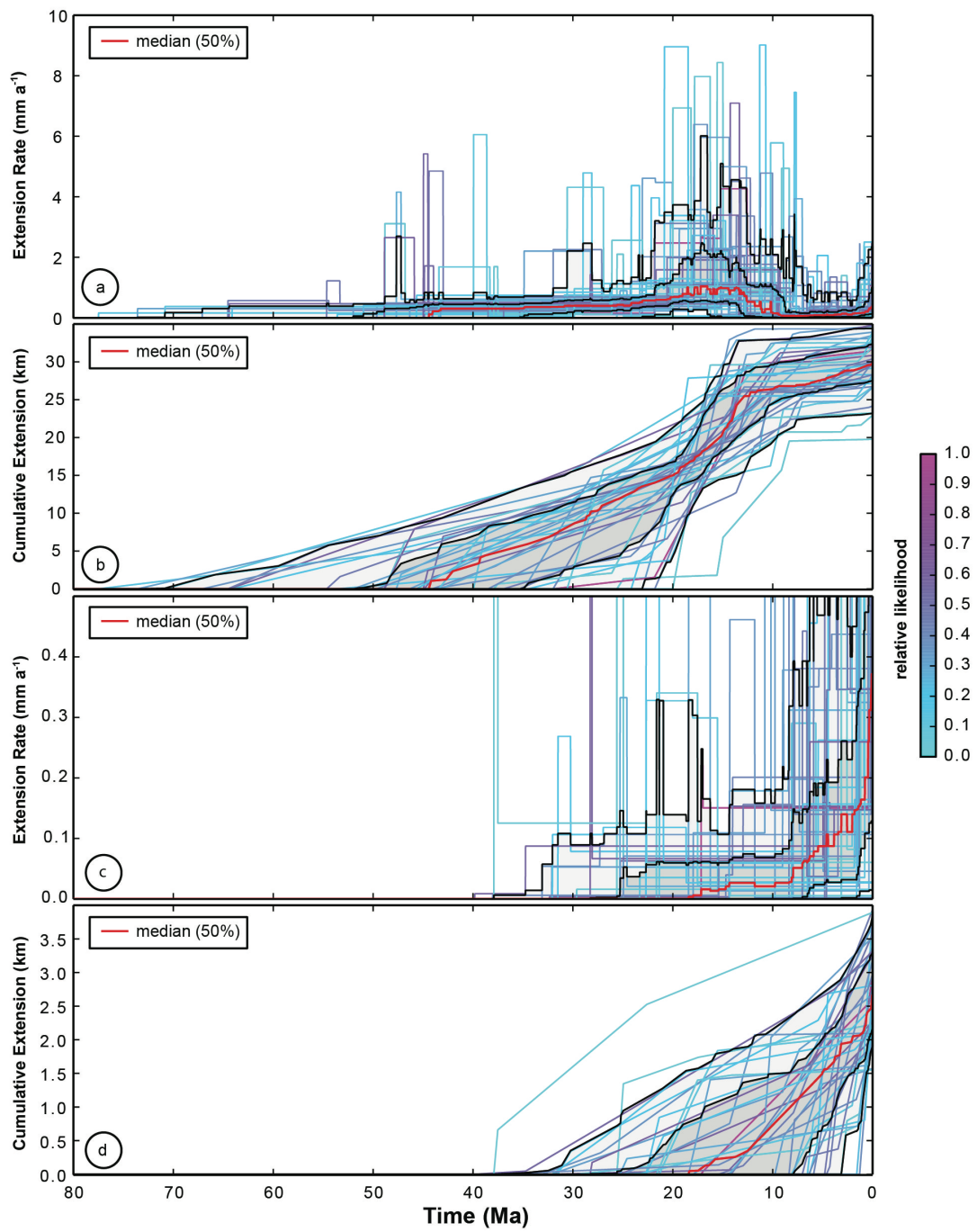


Figure 2.5 Modeled extension histories

Figure 2.5: Modeled extensional histories: Extensional history for the entire SSR (a and b) and for the WPF (c and d) from 39 of 9981 runs, where each colored line represents the relative likelihood of a particular model history based on Bayesian inversion of the $p(T | G)$ to produce the posterior distribution $p(T | D)$ (see section 5.3 and 5.4 of text for further explanation). Purple colored model histories are relatively more likely than blue colored model histories. The red line represents the median extension rate and cumulative extension through time for the SSR. The dark gray shaded area represents a 25th-75th percentile bound around the median for the modeled histories. Light gray shaded area represents a 5th-95th percentile bound around the median for the modeled histories. (a) The extension rate is low on average throughout the Cenozoic in the SSR; however, individual model histories show a fair amount of variability. (b) The median onset of extension for the SSR is ~45 Ma and a median net cumulative extension of ~30 km. (c) Extension rate on the WPF is very low on average at $< 0.5 \text{ mm a}^{-1}$. (d) The median onset for extension on the WPF is ~19 Ma, however accumulation of extension in the system does not occur until ~10 Ma.

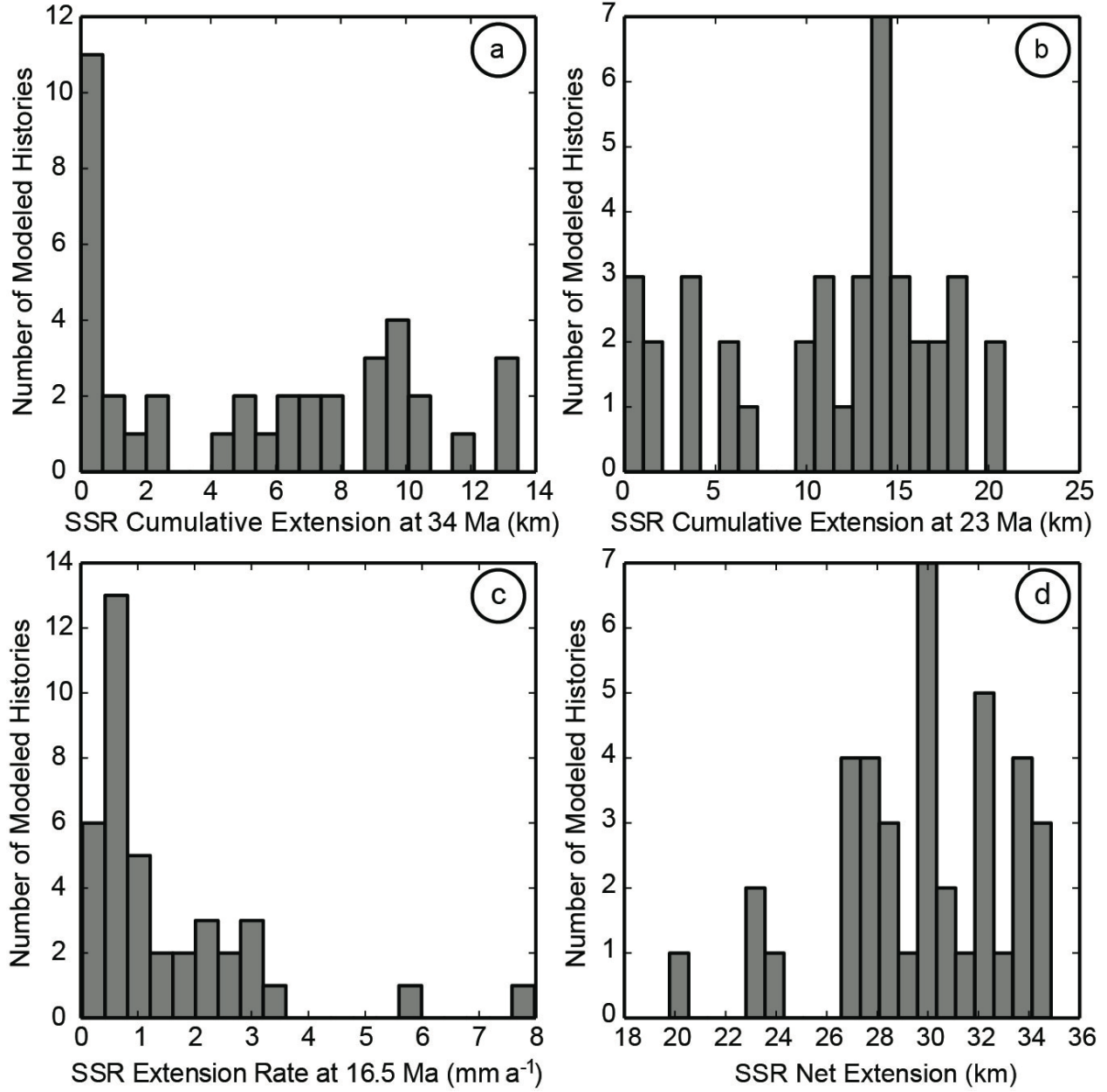


Figure 2.6 Histograms for the posterior model results of the SSR

Figure 2.6: Histograms for the posterior model results of the SSR: (a) Cumulative extension at 35 Ma shows a slightly bimodal distribution. Sixteen modeled histories have < 3 km of extension accumulated by 35 Ma. The remaining 23 of 39 modeled histories have > 4 km of extension by 35 Ma. (b) The histogram for cumulative extension at 23 Ma shows 28 of 39 modeled histories have ≥ 10 km of extension accumulated in the SSR. (c) The extension rate at 16.5 Ma is the highest modeled for the SSR. The histogram shows half of the modeled histories require < 1 mm a^{-1} extension rates, and almost all modeled histories require < 4 mm a^{-1} rates of extension. (d) The majority of the modeled histories (35 of 39) require > 26 km of total net extension in the SSR during the Cenozoic. This extension is accommodated on both the WPF and SSRD structures; however, the earliest onset of extension on the WPF is early Miocene and only accounts for a mean 2.75 km of extension based on the modeled histories.

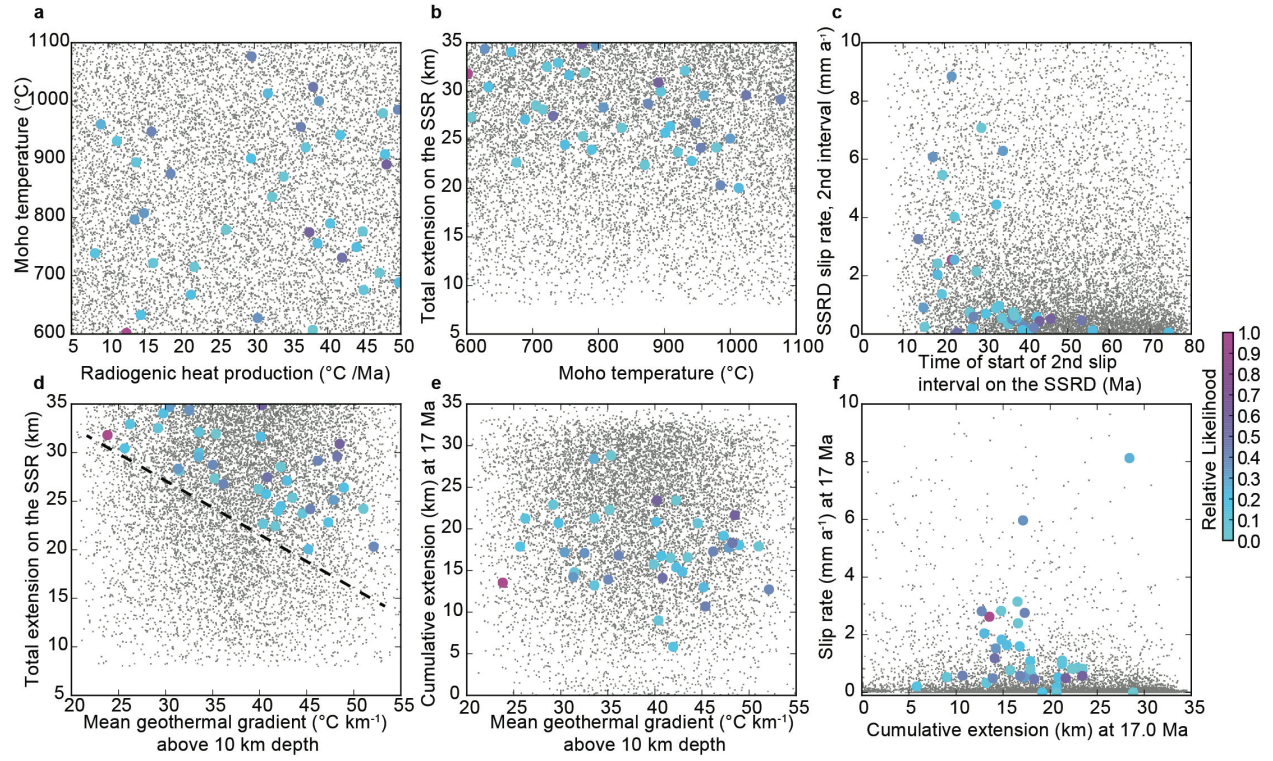


Figure 2.7 Plots of various variables used in models

Figure 2.7: Plots of various variables used in models: Scatterplots of priors (grey dots) and posteriors (colored circles) for various combinations of variables. The top row (a-c) shows variables directly used in the inversion, whereas the bottom row (d-f) shows ‘metavariables’ derived from the input variables which offer more insight into the results, as shown by the distributions of the posteriors. (a) Variables determining the thermal state of the crust; no relationship is observed. (b) Total (i.e., modern) extension across the SSR compared with Moho temperature; no relationship is observed. (c) Timing of the start of the second slip interval on the SSRD versus the slip rate for that interval. Times older than ~30 Ma have very low slip rates, suggesting that little cumulative exhumation occurred during this time; however, if the second interval is younger, faster rates are acceptable. (d) Total SSR extension versus the mean geothermal gradient in the upper crust. The dashed black line indicates a threshold amount of extension required to exhume the thermochronologic samples through their thermal sensitivity windows, which is dependent on the geothermal gradient. (e) Upper-crustal geothermal gradients versus cumulative extension at 17 Ma. The posteriors are somewhat more clustered between ~13-23 km, relative to the total extension shown in b. (f) Cumulative extension versus slip rate at 17 Ma. This plot shows the posteriors to be much more tightly clustered than in plot c.

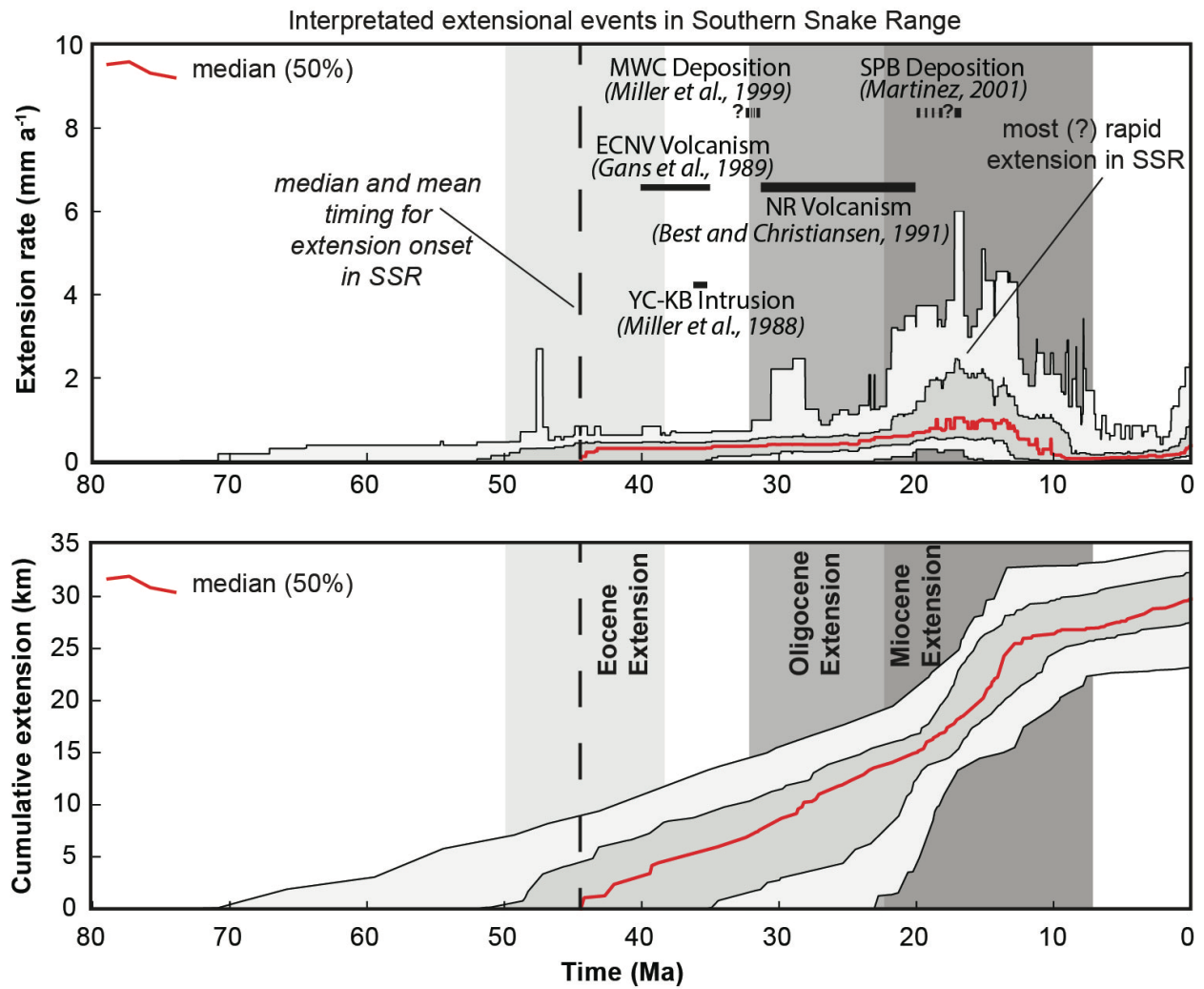


Figure 2.8 Interpreted model histories

Figure 2.8: Interpreted model histories: An interpreted plot of the percentile envelopes for the posterior model histories for the SSR from Figure 2.5. Gray bars show extensional periods discussed in section 6.1. The vertical black dashed line indicates the median and mean onset of extension in the SSR. Thin black line indicates the most rapid period of extension in the SSR from the modeled histories at ~16.5 Ma. The horizontal dashed black lines indicate the relative timing between the deposition of the Murphy Wash conglomerate (MWC) [Miller *et al.*, 1999] in the SSR, development of the Sacramento Pass Basin (SPB) [Martinez, 2001], and the three periods of extension interpreted from the modeling. Solid black bars denote the timing of magmatism in the immediate region of east-central Nevada [Miller *et al.*, 1988; Gans *et al.*, 1989; Best and Christiansen, 1991] relative to defined extensional periods. Abbreviations: MWC-Murphy Wash conglomerate, SPB-Sacramento Pass Basin, SSR-Southern Snake Range, ECNV-east-central Nevada, NR-Needles Range, YCKB-Young Canyon-Kious Basin pluton.

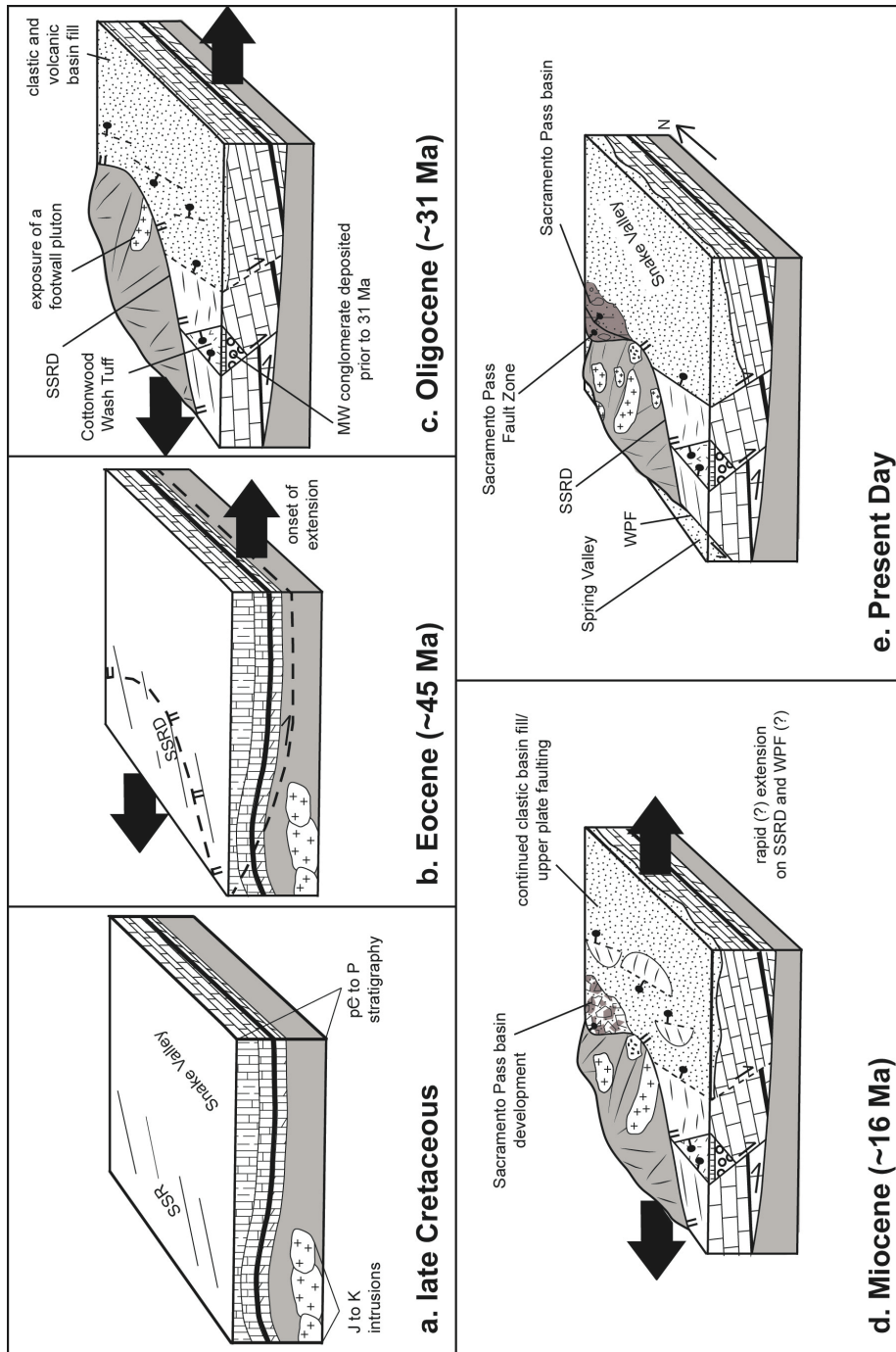


Figure 2.9 Conceptual evolution of the SSR

Figure 2.9: Conceptual evolution of the SSR: Conceptual evolution of the SSR based on our modeled history of extension in the SSR, and ideas presented in *Armstrong* [1972], *Miller et al.* [1983], *Miller et al.* [1988], *McGrew* [1993], *Miller et al.* [1999], *Martinez* [2001], and *Long* [2012]. These figures are not to scale, and orientations, locations, and stratigraphic offsets are conceptual. (a) Prior to extension during the Cenozoic, the area of the present day SSR was intruded by Mesozoic plutons, underwent Mesozoic metamorphism, and was broadly folded during the Sevier orogeny [e.g., *Miller et al.*, 1988]. No significant structural relief existed in the region based on the relatively flat sub-Tertiary unconformity [e.g., *Armstrong*, 1972; *Miller et al.*, 1983; *Long*, 2012]. (b) Based on the posterior model histories the onset of SSR extension occurred at ~45 Ma, and was, at least initially, accommodated solely on a structure similar in orientation to the SSRD of *McGrew* [1993]. (c) Extension in the Oligocene began at ~33 Ma following a period of relative quiescence in the late Eocene based on our model histories. Exposure of a footwall pluton at the surface prior to or during the early Oligocene is necessary if the plutonic clasts present in the Murphy Wash conglomerate beneath the Cottonwood Wash Tuff [*Miller et al.*, 1999] are locally derived. (d) Rapid Miocene extension occurred, and was concurrent with the development of the Sacramento Pass Basin [*Martinez*, 2001]. (e) A present-day conceptual block diagram for the SSR based on *Miller et al.* [1999] and *McGrew* [1993]. Abbreviations: SSR-Southern Snake Range, J-Jurassic, K-Cretaceous, pC-pre-Cambrian, P-Permian, SSRD-Southern Snake Range Décollement, MW-Murphy Wash, WPF-Wheeler Peak Fault.

Tables

Table 2.1 (U-Th)/He age data

Sample	Latitude ^a (°N)	Longitude ^a (°W)	Elevation (m)	Age ^b (Ma)	$\pm 2\sigma_{wm}$ ^c (Ma)	$\pm 2\sigma_{exp}$ ^d (Ma)	MSWD _{wm}	Aliquots
<i>Williams Canyon Samples (zircon)</i>								
12WC01	38.9474	114.3292	2710	37.0	0.61	5.4	78	3
12WC02	38.9484	114.3366	2567	41.5	0.67	2.4	12	4 ^e
12WC03	38.9512	114.3449	2472	40.7	0.53	4.9	84	5
<i>Snake Creek Samples (zircon)</i>								
12SC01	38.9444	114.2983	3316	41.7	0.60	2.6	19	4
12SC03	38.9425	114.2886	3224	40.2	0.66	0.89	1.8	4 ^e
12SC04	38.9418	114.2715	2944	26.4	0.34	3.9	133	5
12SC05	38.9378	114.2614	2666	25.0	0.33	2.8	71	5
12SC06	38.9354	114.2525	2671	21.7	0.26	3.1	150	6
12SC07	38.9296	114.2431	2538	21.1	0.30	1.7	34	4
12SC08	38.9223	114.2328	2373	21.0	0.30	3.3	120	4
<i>Snake Creek Samples (apatite)</i>								
12SC03	38.9425	114.2886	3224	15.1	0.29	2.4	66	5
12SC05	38.9378	114.2614	2666	15.2	0.38	0.7	3.5	3
12SC07	38.9296	114.2431	2538	13.6	0.38	0.7	3.1	3

^aWGS 1984 datum

^bWeighted mean of aliquots not excluded by Hampel identifier

^cPropagated analytical error of weighted mean

^dExpanded error calculated by multiplying the square root of MSWD_{wm} and σ_{wm}

^eAn aliquot was excluded from weighted mean age based on the Hampel identifier

Table 2.2 Pecube modeling input parameters

Parameter	Value
<i>Fixed Parameters</i>	
Model Dimensions (length, width)	119 km E-W and 32 km N-S
FEM Node Spacing (x, y, z directions)	900 m
Thermal Diffusivity^a	25 km ² Myr ⁻¹
Moho Depth^b	30 km (present day)
Surface Temperature^c	15 °C
Atmospheric Lapse Rate	0 °C km ⁻¹
<i>Prior Parameters^d</i>	
<u>SSRD</u>	
Generalized strike of structure	015°
Span of slip history	80-5 Ma
Slip rates	0-10 mm a ⁻¹
Number of slip intervals	4
<u>WPF</u>	
Span of slip history	40-0 Ma
Slip rates	0-4 mm a ⁻¹
Number of slip intervals	3
<u>Thermal Parameters</u>	
Moho temperatures	600-1100 °C
Radiogenic heat production	5-50 °C Ma ⁻¹

^aFrom Whittington et al., 2009

^bFrom Gans, 1987

^cGlobal mean annual temperature

^dSee section 5.1 and 5.2 for discussion of values and references.

Chapter 3: Constraints on the salt thermal anomaly associated with the Gypsum Valley salt wall, Paradox Basin, CO

Abstract

Thermal anomalies associated with salt bodies have been described and modeled in multiple sedimentary basins. The modeling literature suggests that salt thermal anomalies cause elevated temperatures in sedimentary units located above salt bodies (suprasalt positions), and extend laterally one to three salt radii into adjacent sedimentary units. This study tests these predictions using a novel paired thermal maturity analysis and low-temperature apatite (U-Th)/He (ApHe) dating approach in the suprasalt Jurassic Morrison Formation adjacent to the Gypsum Valley salt wall (GVSW), of the Paradox Basin, Colorado. Nine thermal maturity (vitrinite reflectance, Rock-Eval data, thermal alteration index) analyses of mudstones and seven ApHe analyses of sandstones were completed over a ~16 km (~9.9 mi) horizontal transect adjacent to the GVSW. The mudstone samples yielded thermally immature results adjacent to the GVSW. The ApHe ages adjacent to the GVSW range from 20.2 ± 2.1 Ma to 4.6 ± 1.2 Ma, and are the result of cooling within an ApHe partial retention zone prior to well-documented erosional exhumation of the Colorado Plateau after ~10 Ma. Neither set of analytical data shows evidence for a positive magnitude suprasalt thermal anomaly associated with the GVSW. These results suggest modeling predictions for the size and magnitude of salt thermal anomalies cannot be used with confidence in all sedimentary basins, and the failure of the predictions for the GVSW may be due to the thermal conductivity values or heat transfer mechanisms used in the modeling literature. Using outcrop based studies to understand the applicability of salt thermal anomaly modeling has important implications for the energy industry, because thermal anomalies may

affect the location of geothermal prospects, and hydrocarbon maturation or reservoir quality in basins containing salt.

1. Introduction

Thermal anomalies, or local temperature deviations from surrounding regional temperatures, associated with salt structures in sedimentary basins have been modeled for decades in the geologic literature [e.g., *Selig and Wallick*, 1966; *Geertsma*, 1971; *Jensen*, 1983; *O'Brien and Lerche*, 1984; *Vizgirda et al.*, 1985; *Jensen*, 1990; *Yu et al.*, 1992; *Nagihara et al.*, 1992; *Mello et al.*, 1995; *Petersen and Lerche*, 1995; *Nagihara*, 2003]. This focus on modeling research has provided constraints on the location and type of thermal anomalies expected to be associated with salt bodies. The salt thermal anomaly literature suggests that temperatures of sedimentary rocks adjacent to the top of a salt structure (suprasalt position) are higher than regional temperatures away from salt, and temperatures lower than regional values are found in sedimentary units located below salt bodies (subsalt position) [e.g., *Selig and Wallick*, 1966; *Jensen*, 1983; *O'Brien and Lerche*, 1984; *Vizgirda et al.*, 1985; *Blackwell and Steele*, 1989; *Yu et al.*, 1992; *Mello et al.*, 1995; *Peterson and Lerche*, 1995]. This general temperature arrangement of salt thermal anomalies is a result of the “chimney effect” [*Jensen*, 1983], which is a “wicking” of heat through salt structures from lower crustal levels to higher crustal levels because of the higher thermal conductivities of salt in comparison to many other sedimentary rocks [e.g., *Selig and Wallick*, 1966; *Jensen*, 1983; *O'Brien and Lerche*, 1984; *Blackwell and Steele*, 1989]. *Blackwell and Steele* [1989] reported thermal conductivities of salt between 4.80 and 6.05 Wm⁻¹K⁻¹ at 20 °C, whereas shale and sandstone range from 1.05-1.45 Wm⁻¹K⁻¹ and 2.50-4.20 Wm⁻¹K⁻¹ at 20 °C respectively. These ranges are important because modeling literature shows that the greater the contrast between the thermal conductivity of salt and the surrounding rocks, the

greater the size and magnitude of the anomaly associated with the salt body [e.g., *Jensen, 1983; Jensen, 1990; Mello et al., 1995; Petersen and Lerche, 1995*].

The constraints on the size and magnitudes of salt thermal anomalies from the modeling data are conflicting (Table 3.1). The modeling literature suggests the geometry of the salt body, particularly the width of the salt structure, will influence the extent of the salt thermal anomaly [e.g., *Jensen, 1983; O'Brien and Lerche, 1984; Jensen, 1990; Yu et al., 1992; Petersen and Lerche, 1995*]. However, individual models predict varying relationships between salt diapir width and size of thermal anomalies. Some models predict the extent of the thermal anomalies to be two or three times the radius of the salt body [*Jensen, 1990; Petersen and Lerche, 1995*], whereas others suggest the thermal anomalies only extend about one radius away from the salt body [*O'Brien and Lerche, 1984*]. The magnitudes of thermal anomalies, or temperature increases or decreases relative to regional values, also conflict somewhat between studies. For example, the models incorporating salt movement, exposure of salt at the surface, and conductive and advective heat transfer used by *Mello et al. [1995]* show the subsalt negative thermal anomaly may be as high as 85 °C for some salt bodies. In contrast, a model of a buried salt structure using only conductive heat transfer, based on a specific diapir, suggests the negative subsalt thermal anomaly may only be up to 20 °C [*Jensen, 1983*]. The differences in sizes and magnitudes of thermal anomalies from the modeling literature (Table 3.1) are the result of numerous factors, including: the type of heat transfer mechanisms incorporated in the models (e.g., conduction only, conduction and advection, conduction and convection), static or mobile salt bodies, inputs for thermal conductivity of sedimentary units modeled, and salt geometry [e.g., *Jensen, 1983; O'Brien and Lerche, 1984; Mello et al., 1995; Petersen and Lerche, 1995*]. The discrepancies between the model studies highlight the difficulty in capturing the

complexities of heat flow within sedimentary basins containing salt bodies. To further understand heat flow within salt containing sedimentary basins, outcrop based studies are necessary to evaluate the predicted size and magnitude of salt thermal anomalies from the modeling literature. However, few studies have documented salt thermal anomalies in the literature using geochemical analyses from either outcrops or drill cuttings [e.g., *Rashid and McAlary, 1977; Hanson, 2014*].

Field based studies incorporate the geologic complexities of a particular sedimentary basin that may be difficult to parameterize and model, and as a result may provide new insight into the size and magnitude of salt thermal anomalies. *Hanson [2014]* used vitrinite reflectance data, a proxy for paleo-temperature, to show the thermal anomaly associated with a diapir in northeastern Mexico may extend into surrounding sedimentary units two to five times the radius of the salt body. This difference between outcrop based findings and modeling results (c.f. Table 3.1) shows the need for new field studies in other sedimentary basins to quantify salt thermal anomalies. Additional research that constrains the size and magnitude of salt thermal anomalies has important applications in the energy industry. Previous work has highlighted the potential impacts of increased or decreased temperatures near salt and the thermal maturation of salt adjacent petroleum source rocks [e.g., *Rashid and McAlary, 1977; O'Brien and Lerche, 1984; Yu et al., 1992; Mello et al., 1995; Petersen and Lerche, 1995*]. Additional work has shown the possible impact of anomalous temperatures near salt on the rates of quartz cementation petroleum reservoir rocks [e.g., *Hanson, 2014*]. Also, *Jensen [1983]* recognized the application of identifying and quantifying thermal anomalies associated with salt to geothermal energy production. As a result, additional research from field based studies that confirm or deny the

predictive capabilities of salt thermal anomaly modeling in sedimentary basins may have important implications for the energy industry.

This study combines petroleum industry standard thermal maturation indicators (vitrinite reflectance, thermal alteration index, and Rock-Eval data) and apatite (U-Th)/He (ApHe) thermochronology to constrain the size and magnitude of a thermal anomaly associated with the Gypsum Valley salt anticline or salt wall [e.g., *Shoemaker et al.*, 1958; *Cater and Craig*, 1970] located in the Paradox Basin of southwestern Colorado, USA (Figure 3.1). The use of ApHe analyses to constrain the extent and magnitude of salt thermal anomalies is a novel approach, and has not been previously applied in this way. The combination of these techniques has the potential to provide information not only on the size and scale of a salt thermal anomaly associated with the Gypsum Valley salt wall (GVSW), but also insight into the locations of paleo-isotherms.

1.1 Application of (U-Th)/He thermochronology and thermal maturation indicators

Vitrinite reflectance (R_o), Rock-Eval pyrolysis (T_{max}), and thermal alteration index (TAI) data have been traditionally used by the petroleum industry to understand both the thermal maturation of potential petroleum source rocks and the thermal histories of sedimentary basins [e.g., *Dow*, 1977; *Waples*, 1980; *Peters*, 1986; *Tissot et al.*, 1987; *Peters and Cassa*, 1994]. The thermal maturity of a rock, typically associated with petroleum source rocks, is classified as thermally immature (never heated >60 °C), thermally mature (heated to oil-generation window, ~ 60 -150 °C), or thermally postmature (heated to gas-generation window, ~ 150 -200 °C) [e.g., *Peters and Cassa*, 1994]. Therefore, the combination of R_o , TAI, and T_{max} analyses can be used as an imprecise proxy for paleo-temperature. As a result, these techniques can be used to quantify the size and the relative magnitude of a salt thermal anomaly by comparing the thermal maturity

levels of analyzed samples near salt to those far from salt [e.g., *Hanson, 2014*]. If analyzed samples were located in a suprasalt position, then higher thermal maturity levels would be expected within the influence of the thermal anomaly and lower thermal maturity levels would be expected outside the extent of the thermal anomaly [e.g., *Selig and Wallick, 1966; Jensen, 1983; O'Brien and Lerche, 1984; Vizgirda et al., 1985; Yu et al., 1992; Mello et al., 1995; Peterson and Lerche, 1995*]. Thus, the size or extent of the thermal anomaly associated with a salt body may be directly measured, and the magnitude of the thermal anomaly could be inferred by the relative differences in thermal maturity levels.

Traditionally (U-Th)/He thermochronology, an isotopic dating technique that relies on the thermally controlled retention of the He daughter product, has been used to understand the cooling and exhumation history of rocks within the upper crust to understand the timing and rates of a variety of tectonic and erosional denudation processes [e.g., *House et al., 1998; Stockli et al., 2002; Stockli et al., 2003; Reiners, 2005; Stockli, 2005; Flowers et al., 2008; Schildgen et al., 2009a and 2009b; Styron et al., 2013; Gorynski et al., 2013; Evans et al., 2015*]. In contrast, this study uses (U-Th)/He thermochronology in a new way to infer the location, and suppression or elevation of paleo-isotherms adjacent to the GVSF due to the chimney effect of salt bodies in sedimentary basins. The inferred locations in paleo-isotherms could then be used to determine the size and magnitude of a past salt thermal anomaly. Figure 3.2 illustrates the expected patterns of (U-Th)/He cooling ages along a horizontal transect adjacent to a currently exposed salt body given either elevation or suppression of paleo-isotherms due to a suprasalt or subsalt thermal anomaly. If collected samples were originally located in a suprasalt position, then the salt thermal anomaly models predict paleo-isotherms would be elevated adjacent to salt with respect to regional paleo-isotherms away from salt [e.g., *Selig and Wallick, 1966; Jensen, 1983; O'Brien*

and Lerche, 1984; Vizgirda *et al.*, 1985 Yu *et al.*, 1992; Mello *et al.*, 1995; Peterson and Lerche, 1995]. As a result, if samples are taken from approximately the same stratigraphic horizon and are exhumed at the same rate, then cooling ages within the salt thermal anomaly's influence would be younger compared to regional ages (Figure 3.2a). In contrast, if samples collected adjacent to salt were originally located in a subsalt position, then the modeling literature predicts paleo-isotherms would be suppressed adjacent to salt [e.g., Selig and Wallick, 1966; Jensen, 1983; O'Brien and Lerche, 1984; Vizgirda *et al.*, 1985 Yu *et al.*, 1992, Mello *et al.*, 1995; Peterson and Lerche, 1995]. Therefore, if samples are collected from the same position in a flat lying stratigraphic horizon and are exhumed at the same rate, then cooling ages will be older within the salt thermal anomaly compared to regional cooling ages (Figure 3.2b). The size or extent of the thermal anomaly can be inferred from the distance from salt where a “break” in ages between anomalously old or young ages and regional ages is located. Absolute temperature increases or decreases, or magnitude of anomaly, associated with salt can only be broadly constrained using thermochronology. If the cooling ages of the ApHe thermochronometer are “reset” by the salt thermal anomaly, then this suggests the magnitude of the anomaly was at least within the ApHe partial retention zone of ~40-80 °C (see section 3.2) [Wolf *et al.*, 1998; House *et al.*, 1999; Stockli *et al.*, 2000; Farley, 2002].

The combination of the industry standard techniques and the novel ApHe approach will provide new information on the size and magnitude of the salt thermal anomaly associated with the GVSF. The modeling literature predicts that thermal anomalies are present within one to three radii of the salt body (Table 3.1) [O'Brien and Lerche, 1984; Jensen, 1990; Petersen and Lerche, 1995]. The width of Big Gypsum Valley, the location of the GVSF, is about 3.2 km (2 miles) along most of the length of the valley [Cater and Craig, 1970]. Therefore, the modeling

literature predicts there is a positive thermal anomaly of up to 30 °C [e.g., *Vizgirda et al.*, 1985; *Yu et al.*, 1992], that extends ~1.6-4.8 km (~1-3 mi) into the suprasalt sediments adjacent to the GVSW. The new data from the thermal maturity indicators and ApHe analyses were used to test this hypothesis, and to evaluate the use of the thermal anomaly modeling predictions in this area of the Paradox Basin.

2. Geologic setting

The study area is located in the Paradox Basin, on the eastern edge of the Colorado Plateau of southwestern Colorado (Figure 3.1). The northeastern section of the Paradox Basin has multiple salt walls and salt domes exposed at the surface [e.g., *Shoemaker et al.*, 1958; *Cater and Craig*, 1970; *Baars and Stevenson*, 1981; *Trudgill*, 2011], including the GVSW (Figure 3.1b, Figure 3.3). These salt walls and domes are the result of the depositional history and evolution of the Paradox Basin, and subsequent surface exposure of the structures by Tertiary deformation and dissolution [e.g., *Cater and Craig*, 1970; *Trudgill*, 2011]. Understanding the depositional history, basin development, and later dissolution provides an important framework for analyzing the data collected in this study. The goal of this study is to understand the GVSW thermal anomaly. Therefore, the review of the geologic background of the GVSW focuses on two relevant stratigraphic intervals: the salt-containing Pennsylvanian Paradox Formation and the salt-adjacent Jurassic Morrison Formation where analytical samples for the study were collected [e.g., *Shawe et al.*, 1968; *Cater and Craig*, 1970]. The timing of salt movement in the area, the burial history, and exposure of the GVSW are also outlined, because this information is relevant to the interpretation of R_o , TAI, T_{max} , and ApHe analyses.

2.1 Formation of the Paradox Basin and relevant stratigraphy

The Paradox Basin is a peripheral foreland basin associated with the Uncompahgre Uplift, a block of metamorphic and igneous basement rocks initially uplifted in the Pennsylvanian to the Permian by the Ancestral Rocky Mountains orogeny [Barbeau, 2003]. The present-day GVSW region was located within the foredeep of this foreland basin, and the area was a restricted marine environment during the deposition of the oldest formation of the basin, the Pennsylvanian Paradox Formation [Barbeau, 2003]. The Paradox Formation is divided into multiple members [e.g., Trudgill, 2011], but the formation may be generally characterized as alternating layers of evaporites, black shale, limestone, and sandstone [e.g., Shawe *et al.*, 1968; Cater and Craig, 1970; Barbeau, 2003; Trudgill, 2011]. Evaporites were the major rock type deposited in the Paradox Formation, and the formation may have contained >70% halite near the GVSW based on well log data [Cater and Craig, 1970]. The original thickness of the Paradox Formation northwest of the study area was around 2500 m (~8202 ft), and the original thickness was influenced by pre-Pennsylvanian structures present on the “floor” of the Paradox Basin [e.g., Trudgill, 2011]. The evaporite rich portion of the Paradox Formation, or Paradox salt, was mobile after burial, and created the salt walls and domes found in the northeastern portion of the Paradox Basin [e.g., Shoemaker *et al.*, 1958; Cater and Craig, 1970; Trudgill, 2011]. Following deposition of the Paradox Formation, the basin transitioned from a marine to terrestrial environment, as recorded by the Pennsylvanian Honaker Trail Formation and the Permian Cutler Group [e.g., Barbeau, 2003; Trudgill, 2011]. During the Permian the sediment supply rate was greater than accommodation in the Paradox Basin, and the Cutler Group filled the foreland basin [Barbeau, 2003]. The thickness of the Honaker Trail Formation and the Cutler Group decreases near many salt walls in the Paradox Basin due to salt movement towards the surface during the

Pennsylvanian and Permian [e.g., *Cater and Craig*, 1970; *Trudgill*, 2011]. The thicknesses of these formations also increase between salt walls in “minibasins,” or areas with increased accommodation due to salt removal in the subsurface during the passive diapirism of the Paradox salt [e.g., *Cater and Craig*, 1970; *Trudgill*, 2011].

Following deposition of the Permian Cutler Group, up to ~1009 m (~3310 ft) [*Shawe et al.*, 1968] of terrestrial sedimentary rocks characteristic of the Colorado Plateau region, were deposited from the Triassic to the Jurassic near the GVSF [e.g., *Shawe et al.*, 1968; *Cater and Craig*, 1970]. The Morrison Formation is the targeted sampling interval for this study, and is the youngest Jurassic unit exposed in the area [*Stokes and Phoenix*, 1948; *Shawe et al.*, 1968; *Cater and Craig*, 1970]. The formation is composed of mostly sandstones, mudstones, and conglomerates deposited in a fluvial environment, and it is divided into two members, the older Salt Wash Member and the younger Brushy Basin Member [e.g., *Stokes and Phoenix*, 1948; *Shawe et al.*, 1968; *Cater and Craig*, 1970]. The Salt Wash Member is primarily composed of sandstones deposited within fluvial channels, whereas the Brushy Basin Member is dominated by mudstones deposited between fluvial channels [*Stokes and Phoenix*, 1948; *Shawe et al.*, 1968; *Cater and Craig*, 1970]. Notably, the Jurassic Morrison Formation is the first unit to completely bury the Paradox salt of the GVSF [*Stokes and Phoenix*, 1948; *Shawe et al.*, 1968; *Cater and Craig*, 1970]. The burial of the GVSF by the Morrison Formation places this unit unequivocally in a suprasalt position. Although, the Morrison Formation covers the GVSF, its thickness may vary up to ~107-167 m (350-550 ft) near the GVSF, with the thickest portion located in the Disappointment Syncline and the thinnest portions over the top of the GVSF and Dolores Anticline (DA) (Figure 3.3) [*Cater and Craig*, 1970]. This suggests the salt was still somewhat mobile during the Jurassic, and influenced the depositional patterns of the Morrison Formation

[*Cater and Craig*, 1970]. Mobile salt may also have been present below the DA, a structure formed over an area of thickened salt in the subsurface, during the Jurassic [e.g., *Shoemaker et al.*, 1958; *Cater and Craig*, 1970]. The published cross sections of *Stokes and Phoenix* [1948] do not document changes in thickness of the Morrison Formation over the GVSW, DA, or within the Disappointment Syncline, possibly because subsurface information was not yet available from drilling (Figure 3.3b).

In the Cretaceous both non-marine and marine sedimentary units, with a minimum thickness of ~536-884 m (~1760-2900 ft), were deposited on top of the Morrison Formation [e.g., *Shawe et al.*, 1968; *Cater and Craig*, 1970]. *Shawe et al.* [1968] hypothesized the area around the GVSW was covered by an additional 1524 m (5000 ft) of late Cretaceous and Tertiary sediments, that were subsequently eroded away during the Tertiary. These data suggest the Jurassic Morrison Formation adjacent to the GVSW was buried by ~2060-2408 m (~6760-7900 ft) of sedimentary material.

2.2 Timing and mechanism of salt movement

Based on variations in thicknesses of strata adjacent to GVSW from the Honaker Trail Formation to the Morrison Formation, *Cater and Craig* [1970] estimated that Paradox salt was mobile from the Pennsylvanian to late Jurassic. The period of salt movement near the GVSW is longer than the estimated 100 m.y. for the northern Paradox Basin salt walls near Moab, Utah [*Trudgill*, 2011]. Despite the possibly diachronous periods of movement, passive diapirism from sediment loading is considered to be the mechanism behind salt movement throughout the basin [e.g., *Cater and Craig*, 1970; *Trudgill*, 2011]. The passive diapirism created exposed salt walls at the surface starting in the Pennsylvanian [e.g., *Cater and Craig*, 1970; *Trudgill*, 2011], and “minibasins” of thickened sequences of sediments between salt walls because of salt removal

[e.g., *Trudgill*, 2011]. The GVSW was probably exposed at the surface from the Pennsylvanian until the Jurassic, when the Morrison Formation was deposited across the exposed salt [*Cater and Craig*, 1970]. Inherited pre-salt structures, mostly normal faults, underlying the Paradox Formation, interpreted from sub-surface data, are also hypothesized to greatly influence the location of salt walls throughout the Paradox Basin [e.g., *Cater and Craig*, 1970; *Baars and Stevenson*, 1981; *Trudgill*, 2011].

2.3 Tertiary surface exposure of the GVSW

Cater and Craig [1970] suggested the Tertiary period of surface exposure of the GVSW began during the late Cretaceous to Eocene Laramide orogeny when the Pennsylvanian to Tertiary stratigraphy was folded over the GVSW and DA salt [e.g., *Dickinson et al.*, 1988]. This folding may have caused minor faulting adjacent to the GVSW and DA (Figure 3.3), and these faults contributed to the eventual exposure of the GVSW [*Cater and Craig*, 1970] during uplift and exhumation of the Colorado Plateau during the Tertiary to Quaternary [e.g., *McMillan et al.*, 2006; *Hoffman*, 2009; *Cather et al.*, 2012; *Karlstrom et al.*, 2012; *Roberts et al.*, 2012; *Lazear et al.*, 2013]. Dissolution of the subsurface salt of the GVSW was hypothesized to increase during exhumation of the Colorado Plateau, and this dissolution and removal of salt caused the faulting and folding of post-salt stratigraphy into Big Gypsum Valley (Figure 3.3) [*Cater and Craig*, 1970]. These geomorphic and structural processes eventually created the current landscape, where the long axis of Big Gypsum Valley is parallel to the GVSW in the subsurface (Figure 3.3) [*Stokes and Phoenix*, 1948; *Cater and Craig*, 1970].

3. Methodology

Seven paired mudstone and sandstone samples, and two individual mudstone samples were collected along an ~16 km (~9.9 mi) horizontal transect perpendicular to the edge of the GVSW

(Figure 3.3). The nine samples were collected either from the Salt Wash Member or the Brushy Basin Member of the Morrison Formation. The mudstone samples collected were analyzed for R_o , TAI, and T_{max} to constrain thermal maturity of sediments adjacent to the GVSF [e.g., Dow, 1977; Waples, 1980; Peters, 1986; Tissot *et al.*, 1987; Peters and Cassa, 1994]. All seven sandstone samples were analyzed using the apatite (U-Th)/He technique to constrain the thermal history of the Morrison Formation near the GVSF. Samples were collected with <409 m of elevation difference in order to mitigate the influence of burial amount or differential exhumation on sample thermal histories.

3.1 T_{max} , R_o , and TAI

StratoChem Services, a petroleum industry service company, analyzed the nine mudstone samples collected from the Morrison Formation for R_o , T_{max} , and TAI. Samples were assigned aliases prior to analysis by StratoChem Services to prevent sequential sample numbering from influencing subjective microscopic analyses [e.g., Hanson, 2014].

Each sample underwent Rock-Eval pyrolysis, a whole rock step heating method that determines the amount of hydrocarbons released at particular heating steps [e.g., Peters, 1986]. T_{max} is recorded at the temperature when the largest amount of hydrocarbons is emitted during the second step of the heating schedule [Peters, 1986]. Whole rock samples analyzed by StratoChem Services varied between 63.0 to 68.5 mg, and were heated from 0-650 °C using a defined heating schedule for 20 minutes. Higher T_{max} values are associated with greater thermal maturity [e.g., Peters, 1986]. T_{max} values <435 °C indicate thermally immature rocks [Peters and Cassa, 1994]. Values between 435 and 470 °C indicate thermally mature rocks, and values >470 °C indicate post mature rocks [Peters and Cassa, 1994]. Errors were not reported for the T_{max}

analyses, but may be between 1-3 °C according to *Peters* [1986]. The measured T_{\max} values for individual samples are reported in Table 3.2.

In preparation for R_o and TAI analyses each whole rock sample was sieved, digested using HCl and HF, and then separated by heavy liquids to concentrate kerogen, or insoluble organic material [e.g., *Dow*, 1977], similar to methods described by *Dow* [1977] and *Peters and Cassa* [1994]. The concentrated kerogen was mounted in an epoxy plug and polished for microscopic analysis [e.g., *Dow*, 1977; *Peters and Cassa*, 1994]. Vitrinite particles, a type of kerogen from land plants, were identified within the polished mount using reflected light microscopy [e.g., *Dow*, 1977; *Peters and Cassa*, 1994]. Increasing temperatures and length of time at elevated temperatures increase the R_o value (% reflectance) of vitrinite within a sample [e.g., *Dow*, 1977; *Waples*, 1980; *Peters and Cassa*, 1994]. R_o values range from ~0.2-0.6 for thermally immature rocks, ~0.6-1.35 for thermally mature rocks, and >1.35 for post-mature rocks [*Peters and Cassa*, 1994]. The mean R_o and standard deviation (1σ) of the analyzed population for each sample are quoted in text and reported in Table 3.2.

Plant spores present in the sample mount were assigned a TAI value (Chevron scale), using methods similar to those described by *Peters and Cassa* [1994]. Similar to vitrinite particles and R_o values, time and paleo-temperature change the color of spores and pollen within a sample in a predictable manner from yellow (lowest temperatures) to black (highest temperatures) [*Dow*, 1977; *Peters and Cassa*, 1994]. The observed color is assigned a numerical value and TAI values range from ~1.5-2.6 for thermally immature rocks, ~2.6-3.3 for thermally mature rocks, and >3.3 for post-mature rocks [*Peters and Cassa*, 1994]. The TAI value or value range is reported in Table 3.2 for each sample, and no errors are reported for TAI data per industry standards.

3.2 (U-Th)/He thermochronology

ApHe analyses can be used to determine the thermal parameters of the upper crust (e.g., past geothermal gradients) and the timing of exhumation of rocks within the upper crust [e.g., *House et al.*, 1998; *Stockli et al.*, 2002; *Stockli et al.*, 2003; *Reiners*, 2005; *Stockli*, 2005; *Flowers et al.*, 2008; *Styron et al.*, 2013; *Gorynski et al.*, 2013]. The ApHe thermochronometer uses the thermally controlled retention of ^4He produced by radioactive decay of U, Th, and Sm isotopes to date the time apatite crystals within a sample cooled through either the closure temperature [Dodson, 1979] or helium partial retention zone (HePRZ) [e.g., *Wolf et al.*, 1998]. For the ApHe thermochronometer the closure temperature is $\sim 70\text{--}75^\circ\text{C}$ [Farley, 2000; Farley, 2002] and the HePRZ is from $\sim 40\text{--}80^\circ\text{C}$ [Wolf et al., 1998; House et al., 1999; Stockli et al., 2000; Farley, 2002]. As a result, for typical geothermal gradients (e.g., $20\text{--}35^\circ\text{C km}^{-1}$) this system records exhumation of rocks in the upper 1.1 to 4 km (0.7–2.5 mi) of the crust.

All seven sandstone samples collected were dated using the ApHe technique. Each sample was dated using three or more single-grain analyses at Group 18 Laboratories at Arizona State University following analytical techniques and mineral separation procedures described by Schildgen et al. [2009a and 2009b] and van Soest et al. [2011]. All of the dates reported in Table 3.3 are corrected for alpha ejection from the outer $\sim 20\text{ }\mu\text{m}$ of the grains as described by Farley et al. [1996], Farley [2002], and Hourigan et al. [2005]. Evans et al. [2015] outlines the error analysis and Hampel outlier identification technique used to assess the ApHe analyses. In addition to the statistical methods, outlier ApHe aliquots were identified based on visual recognition of anomalous date population distributions; these overdispersed aliquot populations, particularly those with dates that are too old, occur due to undetected U, Th, or Sm bearing inclusions in apatite crystals [e.g., Farley, 2002]. Table 3.3 reports the error-weighted mean

dates and uncertainties, and Table A2.1 reports the individual aliquot dates and uncertainties for each sample.

3.3 Salt distance measurements

To identify the size or extent of a thermal anomaly associated with the GVSW, it is necessary to measure the distance of the nine samples from the salt body. For each sample measurements of the distance along the surface to the edge of the GVSW and distance to sub-surface salt were completed in ArcGIS.

3.3.1 Surface measurements

The western side of the GVSW is located at the edge of Big Gypsum Valley based on the geologic map of *Stokes and Phoenix* [1948]. Surface distance from each sample to the edge of GVSW was measured along a line perpendicular to the edge of salt. The samples were also projected onto the cross section A-A' (Figure 3.3b) from *Stokes and Phoenix* [1948], and the distance to the edge of salt was measured. The two methods of surface measurement do not yield appreciably different results (<120 m). Projection of samples along the cross section allows for an easier visual understanding of mapped fault zones in relation to sample locations; as a result, these surface distance measurements are used to assess the thermal anomaly associated with the GVSW.

3.3.2 Sub-surface measurements

The distance measurement from each sample to sub-surface salt are to a modeled “top” of Paradox salt surface. This modeled surface was created through interpolation of measurements of depth to top Paradox salt from publically available drill well data in the study area (Figure 3.4a). Additionally, a depth to base Paradox salt surface using similar methods was created (Figure 3.4b). The combination of these interpolated surfaces was used to create an isopach map of the

Paradox salt for the study area (Figure 3.5a). All surface contours, depth measurements, and thickness measurements (Figure 3.4 and 4.5a) are reported in feet to remain consistent with the original data, and this allows for future comparisons with other drilling data that is typically recorded in feet. Conversions to metric are made where feasible given available space on figures.

The interpolated depth to top and base Paradox salt surfaces were created from 26 drill wells located in the study area (Figure A2.1). The 26 well records document a depth in feet to top Paradox salt, and 25 report a depth in feet to base Paradox salt. The majority of the depths (21 of 26) reported were true vertical depth, and the remaining depths were corrected to true vertical depth based on deviated well reports available in the public record. All true vertical depth measurements were corrected to be relative to ground level using either the kelly bushing height or derrick floor height, and the specific correction chosen was based on well log reports. The true vertical depth measurements to top and base Paradox salt for each well location are shown in Figure 3.4a and Figure 3.4b, and are reported in Table A2.2. The thickness of the Paradox salt at each well was also calculated from these measurements. The values for thickness at each well location are shown in Figure 3.5a and reported in Table A2.2.

The spline interpolation function in ArcGIS was used to create the depth to top and base Paradox salt surfaces using well data and pseudo-well data created from surface exposures of Paradox salt (i.e., where depth to top salt is zero) (Figure 3.4). This type of interpolation method creates a curved surface that is required to intersect all input data and is well suited to modeling “smoothly varying surfaces” [Childs, 2004]. The amount of curve of the interpolated surface (e.g., how much the surface varies up or down between input data points) can be controlled using a “tension” parameter or weight [Childs, 2004]. For the depth to top and base Paradox salt surfaces the spline interpolation tension was increased to a weight of two. This value of two was

chosen by comparing multiple iterations of interpolated surfaces using various tension weights to the expected geologic characteristics from the mapping and cross section of *Stokes and Phoenix* [1948]. Both interpolated surfaces created are bounded by the edge of Big Gypsum Valley, location of the GVSW [e.g., *Stokes and Phoenix*, 1948; *Cater and Craig*, 1970], and the spatial distribution of available well data (Figure 3.4). The depth to base Paradox salt surface (Figure 3.4b) is smaller than the top Paradox salt surface (Figure 3.4a) for two reasons: (1) there are no corresponding pseudo-wells for the base Paradox salt because the base of Paradox salt is not exposed in Big Gypsum Valley, and (2) the southernmost well location never drilled completely through the Paradox Formation. Despite the differences in data between the two surfaces, the area closest to the sample locations has good data coverage.

The isopach map of Paradox salt thickness (Figure 3.5a) was created using the raster algebra tool in ArcGIS. The interpolated depth to top Paradox salt surface (Figure 3.4a) was subtracted from the depth to base Paradox salt surface (Figure 3.4b) to create the isopach map. The smaller depth to base Paradox salt surface controls the extent of the isopach map. Actual measured thicknesses from well data (labels in Figure 3.5a) agree with the isopach map derived from the interpolated depth to top and base salt surfaces. This agreement suggests the interpolations presented in Figure 3.4 are representative of the geology near the GVSW. The derived isopach map (Figure 3.5a) also generally agrees with an isopach map of Paradox salt from *Shawe et al.* [1968]; however, the new map presented in Figure 3.5a contains more well data than was available in 1968. The thickness of Paradox salt in the subsurface is shown along the *Stokes and Phoenix* [1948] cross section in Figure 3.5b.

4. Results

4.1 T_{\max} , R_o , and TAI results

T_{\max} data for the nine analyzed mudstone samples range from 331 to 395 °C. These values indicate the samples are thermally immature ($T_{\max} < 435$ °C) [Peters and Cassa, 1994]. The R_o data range from 0.38 ± 0.10 to 0.62 ± 0.14 . Eight of the nine samples are thermally immature ($R_o < 0.6$), and a single sample (14GV15) may be thermally mature at 0.62 ± 0.14 [Peters and Cassa, 1994]. The total number of R_o analyses for each sample was significantly fewer (1 to 13 analyses) than the suggested 50-100 analyses for reliable data [Peters and Cassa, 1994]. TAI values for the nine samples range from 2.1 to 2.7. Similar to the R_o analyses, eight samples are thermally immature (TAI=1.5-2.6), and single sample (14GV15) is thermally mature (TAI=2.2-3.6) [Peters and Cassa, 1994].

The TAI and R_o data are internally consistent, which suggests that despite the few vitrinite reflectance analyses per sample, these data are reliably recording thermal maturity. The T_{\max} data shows thermal immaturity for all samples, which broadly correlates with the TAI and R_o data; however, a significant exception is the single R_o and TAI thermally mature sample (14GV15). This particular sample has 13 individual vitrinite analyses and the mean R_o is consistent with the TAI value. However, the error associated with the R_o analysis permits the possibility that 14GV15 is thermally immature ($R_o = 0.62 \pm 0.14$), and therefore consistent with the T_{\max} data.

4.2 Apatite (U-Th)/He results

ApHe dates for the seven samples of the horizontal transect are Miocene to Pliocene in age, and vary from 20.2 ± 2.1 Ma to 4.6 ± 1.2 Ma (Table 3.3). Five of the seven samples are less than 10 Ma and the dates range from ~8.4 to 4.6 Ma. Four of the seven samples are overdispersed, and

outlier aliquots were excluded from the final date calculation based on methods described in section 3.2 (Table 3.3 and A2.1). Each sample aliquot population was analyzed for radiation damage, a possible cause for overdispersed ApHe dates, by comparing the effective uranium concentration (eU) and aliquot dates [e.g., *Shuster et al.*, 2006; *Flowers et al.*, 2009]. No correlations between aliquot date and eU were observed in these data. It is more likely the overdispersed sample dates are due to unrecognized U, Th, or Sm bearing inclusions [e.g., *Farley*, 2002] or U, Th, Sm zonation within an analyzed crystal [e.g., *Hourigan et al.*, 2005].

5. Discussion

5.1 T_{\max} , R_o , and TAI interpretations

The thermal maturity analyses (T_{\max} , R_o , TAI; Table 3.2) indicate the sampled section of the Morrison Formation is thermally immature, within error, for ~16 km (~9.9 mi) adjacent to the western edge of the GVSF. For simplicity of the following discussion, R_o will be used as a proxy for all three thermal maturity indicators (T_{\max} , R_o , TAI) because these systems, within error, yielded internally consistent results.

Figure 3.6a shows R_o does not vary with increasing distance from the edge of the GVSF. Sample 14GV15 located within one salt radius, does record a higher average R_o value than the other eight samples located further from salt (Figure 3.6a). However, because this sample may be thermally immature within the error of measurement it is not possible to interpret the presence of a salt thermal anomaly based on this sample alone. Instead, the almost invariable R_o values indicate there is no unequivocal thermal anomaly associated with the GVSF. To understand if any relationship existed between thermal maturity and the nearest salt, which may be in the subsurface, the depth to salt below each sample and R_o were plotted (Figure 3.7a). There is no correlation between depth to salt and thermal maturity of the sample (Figure 3.7a). For example

samples 14GV15 and 14GV13 have similar R_o values, within error of measurement, and very different depths to salt of ~1000 m and ~2500 m (~3280 ft to ~8202 ft). To investigate if salt thickness may have influenced thermal maturity, the isopach map (Figure 3.5a) derived from the interpolated drill data was used to determine thickness of salt below each sample. The plot of salt thickness and R_o shows samples with similar values, within error of measurement (e.g., 14GV15 and 14GV13), are located over different salt thicknesses of <500 m and >1500 m (<1500 ft and ~5000 ft) (Figure 3.5a, Figure 3.8a).

The consistent thermal maturity of the mudstone samples across ~16 km (~9.9 mi) indicates there is no identifiable thermal anomaly related to the GVSW within the suprasalt Morrison Formation. This interpretation directly contrasts with the salt thermal anomaly modeling literature that predicts the thermal maturity of suprasalt samples will be higher than regional thermal maturities within one to three salt radii [O'Brien and Lerche, 1994; Jensen, 1900; Petersen and Lerche, 1995]. Based on the lack of correlation between thermal maturity and distance to salt or thickness of salt, it seems most likely the thermal maturity recorded by R_o , T_{max} , and TAI is solely the result of burial by overlying sedimentary units.

An estimated ~2060-2408 m (~6760-7900 ft) of Cretaceous to Tertiary strata were deposited near GVSW on top of the Morrison Formation [Shawe *et al.*, 1968; Cater and Craig, 1970]. These estimates agree well with Colorado Plateau wide studies that suggest ~1500-2000 m (~4921-6561 ft) of overburden were removed near GVSW in the Cenozoic [Pederson *et al.*, 2002; Lazear *et al.*, 2013]. Using the study area specific estimate, the 60 °C paleo-isotherm, or upper temperature limit for thermal immaturity [Peters and Cassa, 1996], would have been located near or below the collected samples Tertiary prior to erosional denudation (Figure 3.9). This paleo-isotherm reconstruction assumes a 10 °C average surface temperature, and a

geothermal gradient of $20\text{ }^{\circ}\text{C km}^{-1}$, based on paleo-geothermal gradient estimates and present day measurements in the central Colorado Plateau of east-central and southeastern Utah [e.g., *Bodell and Chapman*, 1982; *Hoffman*, 2009]. If these thermal parameters are correct then the maximum burial depth from *Shawe et al.* [1968] and *Cater and Craig* [1970] may be overestimated by up to 260 m, because three thermally immature samples are located below the $60\text{ }^{\circ}\text{C}$ paleo-isotherm for the maximum burial depth (Figure 3.9b). However, this overestimation is not conclusive because the reconstruction makes multiple assumptions that may affect the location of the paleo-isotherm including: the topography of the Jurassic surface, paleo-surface temperature, and paleo-geothermal gradient. *Bodell and Chapman* [1982] showed the outer rim of the Colorado Plateau, where the GVSF is located, currently has higher heat flows than the central portion of the plateau; therefore, a higher paleo-geothermal gradient may be more appropriate near the GVSF. However, significantly higher paleo-geothermal gradients near GVSF would require the depth of burial of the Morrison Formation from multiple studies [e.g., *Shawe et al.*, 1968; *Cater and Craig*, 1970; *Pederson et al.*, 2002; *Lazear et al.*, 2013] to be greatly overestimated, and this seems unlikely given the multiple approaches used to arrive at these estimates. If the average burial depth estimate from these studies is appropriate ($\sim 1954\text{ m}$) and the paleo-geothermal gradient was higher than $\sim 26\text{ }^{\circ}\text{C km}^{-1}$, then the R_o , T_{max} , and TAI would have recorded thermally mature samples (e.g., heated $>60\text{ }^{\circ}\text{C}$) near the GVSF. Because these samples were not thermally mature, it seems unlikely that significantly higher paleo-geothermal gradient estimates are warranted near the GVSF, and that the thickness estimates of Cretaceous to Tertiary strata are generally reasonable.

Despite some uncertainties in the paleo-isotherm interpretations, the R_o , T_{max} , and TAI analyses from the Morrison Formation adjacent to the GVSF are most likely the result of burial

by Cretaceous and Tertiary units. This suggests there is not a suprasalt thermal anomaly associated with the GVSF of sufficient extent or magnitude to affect the thermal maturity of the Morrison Formation. Therefore, the currently published predictive capabilities of the salt thermal anomaly models are poor near the GVSF.

5.2 (U-Th)/He results and distance to salt

The seven ApHe ages may increase in age with increasing distance from the edge of salt (Figure 3.6b) with two exceptions, 14GV14 (5.9 ± 0.2 Ma) and 14GV04 (4.6 ± 1.2 Ma). An alternative, and equally reasonable, interpretation of these ApHe data would be there is no variation in ApHe age with distance from salt with two exceptions, 14GV08 (13.2 ± 4.2 Ma) and 14GV02 (20.2 ± 2.1 Ma). Only sample 14GV08 is located near a mapped fault zone (Figure 3.6b), and this suggests neither faulting within the stratigraphy or hydrothermal fluids flowing along faults are the cause of these “outlier” sample pairs. A simple linear regression of the data does show a positive correlation between ApHe age and distance (Figure 3.6b); however, the correlation is weak ($r^2=0.33$). The “outlier” sample pairs make it difficult to interpret a definitive ApHe age-distance from salt trend. Therefore, these data do not unequivocally show the ApHe age-distance from salt trend expected for a positive suprasalt thermal anomaly extending one to three radii from the edge of salt (Figure 3.2a) [e.g., *O’Brien and Lerche*, 1994; *Jensen*, 1900; *Petersen and Lerche*, 1995]. Similar to the thermal maturity analyses, no ApHe age and depth to salt or ApHe age and thickness of salt correlations exist (Figure 3.7b and 3.8b). The depth to salt for samples 14GV18 and 14GV02 are nearly identical at ~1750 m (~5741 ft), and the ApHe ages recorded by these samples are ~6.3 Ma and ~20.2 Ma respectively (Figure 3.4a and Figure 3.7b). Samples 14GV14 and 14GV16 have similar ApHe ages, and are located over <500 m (<1640 ft) thick salt and ~1500 m (~4921 ft) thick salt respectively (Figure 3.5a and Figure 3.8b).

The equivocal ApHe age-distance to salt trend, and lack of correlations between depths to salt or salt thickness suggest no positive suprasalt thermal anomaly of sufficient extent or magnitude to affect the ApHe thermochronometer was present on the western flank of the GVSF. Instead, the ApHe ages likely reflect cooling below the ApHe PRZ due to the well-documented exhumation of the Colorado Plateau after around 10 Ma [e.g., *McMillan et al.*, 2006; *Hoffman*, 2009; *Cather et al.*, 2012; *Karlstrom et al.*, 2012 and references therein; *Roberts et al.*, 2012; *Lazear et al.*, 2013]. If exhumation of the Colorado Plateau after ~10 Ma is responsible for the timing of cooling recorded by ApHe ages adjacent to the GVSF, then ApHe ages for all samples are expected to be <10 Ma. Although five out of the seven ApHe ages adjacent to the GVSF are <10 Ma, samples 14GV08 and 14GV02 have cooling ages of ~20.2 Ma and ~13.2 Ma respectively. *Hoffman* [2009] documented similar “anomalously old” ApHe ages in samples from the central Colorado Plateau and attributed these ages to cooling within an ApHe PRZ for long periods prior to the <10 Ma exhumation event. This interpretation was based on the idea that long periods of cooling within a HePRZ may cause anomalous ApHe ages due to variability in He diffusivity within individual apatite grains [e.g., *Wolf et al.*, 1996; *Farley*, 2002; *Flowers et al.*, 2009; *Hoffman*, 2009]. Based on the paleo-isotherm reconstruction, the ApHe samples adjacent to the GVSF were likely also located in the upper portion of a paleo-HePRZ prior to erosional removal of overlying Cretaceous and Tertiary units after ~10 Ma (Figure 3.9). Even if a higher geothermal gradient of ~26 °C km⁻¹ is more appropriate, the ApHe samples buried below the maximum estimated ~2408 m (~7900 ft) would still have been within the ApHe PRZ. Therefore, the >10 Ma ApHe ages for samples 14GV08 and 14GV02 may be the result of cooling within the paleo-ApHe PRZ adjacent to the GVSF, similar to samples from the central Colorado Plateau prior to the well documented period of exhumation after ~10 Ma [e.g.,

Hoffman, 2009]. The combination of the paleo-ApHe PRZ adjacent to the GVSW and the majority of samples recording ApHe cooling ages <10 Ma suggests the equivocal ApHe age-distance trend is not due to a salt thermal anomaly, but rather due to exhumation of the Colorado Plateau after ~10 Ma [e.g., *McMillan et al.*, 2006; *Hoffman*, 2009; *Cather et al.*, 2012; *Karlstrom et al.*, 2012 and references therein; *Roberts et al.*, 2012; *Lazear et al.*, 2013].

5.3 Apparent absence of a suprasalt thermal anomaly

Salt thermal anomalies are documented in the literature from well temperature data and thermal maturity indicators, and modeling has suggested suprasalt thermal anomalies increase local temperatures up to 30 °C and extend one to three salt radii into adjacent sediments (Table 3.1) [*Rashid and McAlray*, 1977; *O'Brien and Lerche*, 1984; *Jensen*, 1983; *Vizgirda et al.*, 1985; *Jensen*, 1990; *Yu et al.*, 1992; *Mello et al.*, 1995; *Petersen and Lerche*, 1995; *Hanson*, 2014]. However, the thermal maturity indicators and ApHe data from the suprasalt Morrison Formation adjacent to the GVSW show no evidence of a positive thermal anomaly. However, the total absence of a suprasalt thermal anomaly is not precluded by this study. Interpretations of data from this study suggests that if a positive suprasalt thermal anomaly is present it must extend less than one salt radius, and be of a small enough magnitude that it would not influence the location of paleo-isotherms. Either way, the available data show no compelling evidence for the presence of a positive suprasalt thermal anomaly extending one to three salt radii into sedimentary units adjacent to the GVSW as predicted by the modeling literature [e.g., *O'Brien and Lerche*, 1984; *Jensen*, 1983; *Vizgirda et al.*, 1985; *Jensen*, 1990; *Mello et al.*, 1995; *Petersen and Lerche*, 1995].

The apparent absence of a suprasalt thermal anomaly associated with the GVSW suggests the predictive capabilities of the modeling literature are insufficient near Gypsum Valley. To

examine the possible reasons for the limited applicability of the salt thermal anomaly modeling literature to the GVSF, parameters used in the modeling literature are discussed and compared to the geology of the GVSF. Thermal anomalies associated with specific salt bodies in sedimentary basins may be influenced by the geometry of the salt body, depth of burial, thermal conductivity contrasts between salt and the adjacent sedimentary units, and heat transfer mechanisms [e.g., *Jensen, 1983; O'Brien and Lerche, 1984; Mello et al., 1995; Petersen and Lerche, 1995*]. Understanding the mismatch between parameters used in the modeling literature and the geology of the GVSF provides new information for future modeling studies of salt thermal anomalies, which have important implications for the energy industry.

5.3.1 GVSF geometry and modeling literature

The geometries of salt bodies have been modeled using both simple rectangular or cylindrical shapes [e.g., *Selig and Wallick, 1966; O'Brien and Lerche, 1984; Jensen, 1990*], and by more complex geometries [e.g., *Jensen, 1983; Yu et al., 1992; Mello et al., 1995; Petersen and Lerche, 1995*]. The two-dimensional geometry of the GVSF interpreted from the depth to top and base Paradox salt does not have a complex shape (Figure 3.5b), and at a first-order may be well approximated by a modeled two-dimensional rectangular or rounded salt body attached to a base layer of salt [e.g., *Selig and Wallick, 1966; Jensen, 1990; Mello et al., 1995*]. As a result of the general similarity between the geometries of salt bodies in the modeling literature and the geometry of the GVSF, it is unlikely that a mismatch between the models and the GVSF is the cause of the over predicted extent and magnitude of a suprasalt thermal anomaly associated with the GVSF. One caveat to this interpretation is that in three-dimensions the modeling literature of cylindrical salt bodies is not representative of the elongate GVSF.

However, because three-dimensional models are not available in the literature the impact on suprasalt thermal anomalies is difficult to assess.

5.3.2 Burial depth of the GVSW

Mello et al. [1995] created models that show the burial depth of salt in a basin can have a significant influence on the type of thermal anomaly expected. From these models *Mello et al.* [1995] estimated that salt bodies located within ~1.5-1.8 km of the Earth's surface have a significant reduction in the magnitude of the positive suprasalt thermal anomaly and an increase in the magnitude of the subsalt thermal anomaly. Following the onset of Paradox salt motion in the Pennsylvanian and prior to the deposition of the late Jurassic Morrison Formation the GVSW was probably exposed at the surface or very close to the surface [*Cater and Craig*, 1970]. As a result, any thermal anomaly associated with the GVSW from the Pennsylvanian until the Jurassic would have been confined to subsalt positions [*Mello et al.*, 1995]. However, the GVSW following the deposition of the Cretaceous Mancos Shale was buried by ~753-1393 m (~2505-4480 ft) of overburden [*Shawe et al.*, 1968; *Cater and Craig*, 1970]. As a result, a positive, if possibly reduced, suprasalt thermal anomaly is predicted to be associated with the GVSW following deposition of the Cretaceous Mancos Shale [e.g., *Mello et al.*, 1995]. Sometime during the Tertiary the depth of burial of the GVSW probably exceeded the ~1.5-1.8 km value [e.g., *Shawe et al.*, 1968; *Cater and Craig*, 1970; *Pederson et al.*, 2002; *Lazear et al.*, 2013], and therefore a “full strength” suprasalt thermal anomaly would be expected [*Mello et al.*, 1995]. This positive suprasalt thermal anomaly would then be predicted to persist until erosional denudation removed enough overburden to have exhumed the GVSW to within ~1.5-1.8 km of the surface [*Mello et al.*, 1995]. This exhumation probably occurred sometime after ~10 Ma based on a study of the amount and timing of erosion on the Colorado Plateau [e.g., *Lazear et al.*,

2013]. Based on the burial history of the GVSU, models of *Mello et al.* [1995] predict a suprasalt thermal anomaly would be present during at least part of the Tertiary, and would have disappeared entirely once the GVSU was exposed at the surface. The thermal maturity indicators (R_o , T_{max} , and TAI) record the maximum maturity of a sample, and because these data suggest the Morrison Formation never reached temperatures above those expected for simple burial by overlying strata there is no evidence for a paleo-suprasalt thermal anomaly during the Tertiary. Therefore, the apparently absent suprasalt thermal anomaly associated with the GVSU cannot be explained by insufficient burial or present day exposure at the surface.

5.3.3 Thermal conductivity contrasts

The contrast between salt thermal conductivity and the thermal conductivity of typical sedimentary rocks is a fundamental principle cited for the presence of salt thermal anomalies in sedimentary basins [e.g., *Selig and Wallick*, 1966; *Jensen*, 1983; *O'Brien and Lerche*, 1984; *Blackwell and Steele*, 1989; *Jensen*, 1990; *Yu et al.*, 1992; *Mello et al.*, 1995; *Petersen and Lerche*, 1995]. The amount of thermal conductivity contrast between salt and the sedimentary rock adjacent to salt has a positive correlation with the magnitude of the predicted salt thermal anomaly (e.g., the higher the contrast the higher the thermal anomaly magnitude) [e.g., *O'Brien and Lerche*, 1984; *Jensen*, 1983; *Jensen*, 1990; *Mello et al.*, 1995; *Petersen and Lerche*, 1995]. If the thermal conductivity contrast between the GVSU and adjacent sedimentary units is lower than predicted by the modeling literature, then this may explain the absence of the positive suprasalt thermal anomaly.

There are multiple factors that control the contrast in thermal conductivities between salt and adjacent sedimentary units. Shale has a significantly lower thermal conductivity range (1.05-1.45 $Wm^{-1}K^{-1}$) than either sandstone (2.50-4.20 $Wm^{-1}K^{-1}$) or salt (4.80-6.05 $Wm^{-1}K^{-1}$) at 20 °C

[*Blackwell and Steele, 1989*]. Shale is also known to have variable thermal conductivity, with higher thermal conductivity along beds, but the specific values of the directional thermal conductivity are not known [*Blackwell and Steele, 1989; Waples, 1994*]. As a result, it is difficult to evaluate the specific effect this may have on the extent and magnitude of salt thermal anomalies. If horizontal thermal conductivities of shales adjacent to the GVSF are significantly higher than the values used by the thermal modeling literature, then the apparent absence of the suprasalt thermal anomaly may be due to a lack of significant thermal conductivity contrasts between salt and laterally adjacent shales. However, this hypothesis is highly speculative, and may not be a significant factor in sedimentary basins containing salt.

The thermal conductivity of salt decreases more significantly with increasing temperature than either sandstone or shale, which may affect the thermal anomalies associated with salt bodies [e.g., *O'Brien and Lerche, 1984; Jensen, 1983; Blackwell and Steele, 1989; Lerche, 1991; Mello et al., 1995; Petersen and Lerche, 1995*]. Using data from *Mello et al. [1995]* the thermal conductivity contrast between salt and sandstone or salt and shale is ~1.3 to 3.8 times greater at 0 °C, and the contrast is between ~1.1 to ~2.7 times greater at 100 °C. At the temperatures of interest (<100 °C) near the GVSF, this decrease in thermal conductivity does not alter the contrast between salt and adjacent sedimentary units significantly. Therefore, a temperature dependent alteration of the thermal conductivity contrast between salt and adjacent sedimentary units should not have been an issue near the GVSF.

Mello et al. [1995] specifically addressed the variability in thermal conductivity contrasts between salt and adjacent rock units due to variations in rock type. A sedimentary basin composed of only shale and salt was modeled, and observed to have a higher positive suprasalt thermal anomaly (~25 °C) compared to a basin modeled with only sandstone and salt (~6 °C)

[Mello *et al.*, 1995]. Jensen [1990] and Petersen and Lerche [1995] also varied the relative ratio of thermal conductivity of salt to adjacent sedimentary units, which simulates more realistic scenarios where sedimentary basins include multiple rock types. These researchers found a similar reduction in the positive suprasalt thermal anomalies in basins with lower thermal conductivity contrasts between salt and adjacent sediments. In addition, Vizgirda *et al.* [1985] found that varying the thermal conductivity of salt and adjacent sedimentary units was necessary to accurately model well temperature data near a salt body in the Gulf of Mexico. If the thermal conductivity contrast between the GVSF and adjacent sediments was similar to the lower contrast ratios modeled [e.g., Jensen, 1990; Mello *et al.*, 1995; Petersen and Lerche, 1995], then the apparent absence of a positive suprasalt thermal anomaly may be explained. Mudstones, mostly collected from the mudstone rich Brushy Basin Member of the Morrison Formation [e.g., Stokes and Phoenix, 1948; Shawe *et al.*, 1968; Cater and Craig, 1970], were analyzed for thermal maturity using R_o , T_{max} , and TAI. Sandstones, mostly collected in the predominately sandstone Salt Wash Member of the Morrison Formation [e.g., Stokes and Phoenix, 1948; Shawe *et al.*, 1968; Cater and Craig, 1970], were analyzed using the ApHe thermochronometer. If the apparently absent suprasalt thermal anomaly is due to a low thermal conductivity contrast between the GVSF and adjacent sediments, then the thermal anomaly might be expected to be absent in the sandstone rich Salt Wash Member but present in the mudstone rich Brushy Basin Member. However, neither set of data record the presence of a positive suprasalt thermal anomaly. This suggests that the contrast in thermal conductivity between the GVSF and the Morrison Formation is not the cause of the apparent absence of the positive suprasalt thermal anomaly [e.g., Jensen, 1990; Mello *et al.*, 1995; Petersen and Lerche, 1995]. There is a potentially important caveat to this interpretation. If the thermal conductivity contrast between

the GVSF and the entire package of adjacent sedimentary units averaged out to a low value (e.g., sandstone to salt thermal conductivity contrast) rather than a high value (e.g., shale to salt thermal conductivity contrast), then this may explain the apparent absence of a positive suprasalt thermal anomaly [e.g., *Jensen, 1990; Mello et al., 1995; Petersen and Lerche, 1995*]. However, in the absence of detailed thermal conductivities of all sedimentary units adjacent to the GVSF, including eroded Cretaceous and Tertiary material, the influence of thermal conductivity contrast on the magnitude of a suprasalt thermal anomaly cannot be evaluated.

5.3.4 Potential impact of advective or convective heat transfer

An additional parameter that may create mismatches between observed and modeled salt thermal anomalies are the modeled mechanisms of heat transfer (e.g., conduction, advection, convection) within a basin. Many models suggest only conductive heat transfer, or heat transfer through vibrations between atoms [e.g., *Beardmore and Cull, 2001*], is important adjacent to salt bodies [e.g., *Jensen, 1983; O'Brien and Lerche, 1984; Vizgirda et al., 1985; Jensen, 1990; Nagihara et al., 1992; Petersen and Lerche, 1995*]. However, other researchers have employed convective or advective heat transfer mechanisms, or heat transfer by the movement of fluids or solids within the crust [e.g., *Zhao et al., 2008*], when modeling salt thermal anomalies [e.g., *Yu et al., 1992; Mello et al., 1995*]. If advection and/or convection are an important mechanism of heat transfer within some sedimentary basins, then models employing only conductive heat transfer may not accurately predict the extent and magnitude of a salt thermal anomaly in these basins. The potential influence advective or convective heat transfer may have had on a GVSF suprasalt thermal anomaly is not known. Convection of fluids due to the presence of salt and associated thermal anomalies have been modeled in a sedimentary basin [e.g., *Evans and Nunn, 1989*]; however, these authors suggested that convective heat transfer would be secondary to conductive

heat transfer near salt bodies. Fluid flow near salt walls in the Paradox Basin has been documented [e.g., *Morrison and Parry*, 1986; *Chan et al.*, 2000], but no specific studies regarding the GVSF are known. However, advective and/or convective heat transfer is likely to occur in some sedimentary basins. If these mechanisms played a large role in heat transfer adjacent to the GVSF this may explain the lack of a suprasalt thermal anomaly. This suggests that models of salt thermal anomalies should incorporate advective and conductive heat transfer unless there is compelling geologic evidence that suggests their effects are negligible.

6. Conclusions

The new thermal maturity data and ApHe ages collected adjacent to the western flank of the GVSF show no evidence of a positive suprasalt thermal anomaly extending one to three salt radii from edge of salt as predicted by modeling literature [e.g., *O'Brien and Lerche*, 1984; *Jensen*, 1983; *Vizgirda et al.*, 1985; *Jensen*, 1990; *Mello et al.*, 1995; *Petersen and Lerche*, 1995]. The invariable thermal immaturity of R_o , T_{max} , TAI analyses from samples collected in the suprasalt Morrison Formation adjacent to the GVSF are consistent with burial beneath ~2060-2408 m (~6760-7900 ft) of Cretaceous and Tertiary strata [e.g., *Shawe et al.*, 1968; *Cather and Craig*, 1970]. The new ApHe ages from samples, also located within the suprasalt Morrison Formation, are consistent with burial beneath Cretaceous and Tertiary strata, followed by the well known erosional exhumation of the Colorado Plateau after ~10 Ma [e.g., *McMillan et al.*, 2006; *Hoffman*, 2009; *Cather et al.*, 2012; *Karlstrom et al.*, 2012 and references therein; *Roberts et al.*, 2012; *Lazear et al.*, 2013]. The combination of interpretations from the thermal maturity indicators and ApHe analyses suggests that salt thermal anomaly models are not predictive for the GVSF. A comparison of modeling parameters and geologic information from the study area

suggests that thermal conductivity contrasts and/or heat transfer mechanisms used in the modeling literature may not be representative of the GVSW and adjacent rock units.

The new interpretations from this field-based study suggest that models of salt thermal anomalies are not broadly applicable to all sedimentary basins. This finding is similar to a previous outcrop based study in La Popa basin, Mexico showing an unexpected extent for a salt thermal anomaly associated with the El Gordo diapir [*Hanson, 2014*]. Understanding basin specific salt thermal anomalies, and appropriately modeling their extent and magnitude has important implications for the energy industry because salt thermal anomalies may affect thermal maturation and cementation rates, both critical considerations for petroleum systems [e.g., *Rashid and McAlary, 1977; O'Brien and Lerche, 1984; Yu et al., 1992; Mello et al., 1995; Petersen and Lerche, 1995; Hanson, 2014*]. Additionally, if salt thermal anomalies are to be used as a geothermal resource [e.g., *Jensen, 1983*], understanding basin specific controls for the presence or absence of salt thermal anomalies is important. This suggests future models of basin heat flow where salt is present should be basin specific for accurate predictions of size and magnitude of suprasalt thermal anomalies.

Figures

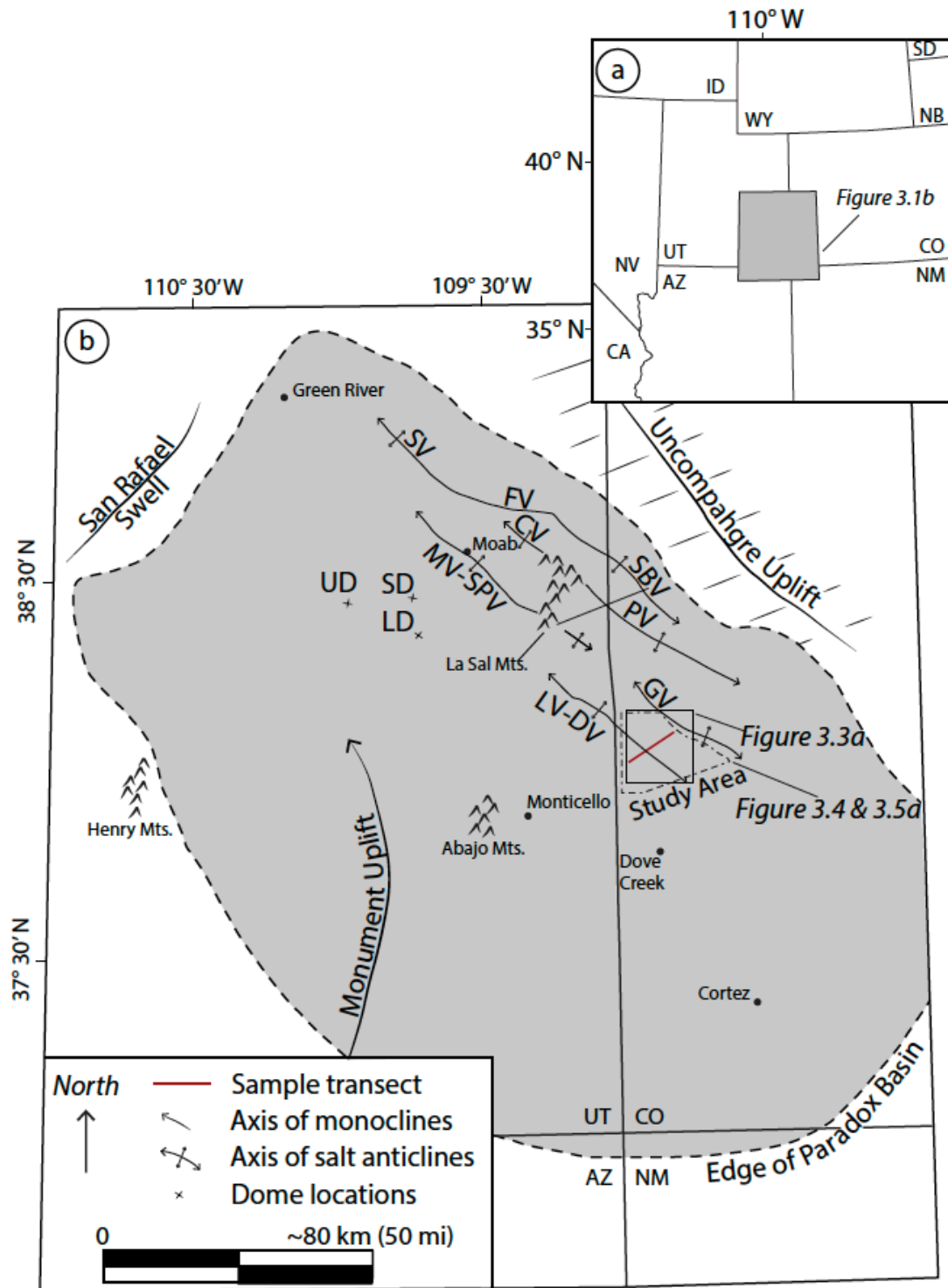


Figure 3.1 Location map of study area

Figure 3.1: Generalized map showing the locations of salt structures and important features of the Colorado Plateau after *Shoemaker et al.* [1958], *Byerly and Joesting* [1959], *Case and Joesting* [1972], and *Lawton and Buck* [2006]. (a) Location of inset map (Figure 3.1b) in the western United States. (b) Outline of the Paradox Basin, with the location of salt structures, laccoliths, and major structures of the central and eastern Colorado Plateau from *Byerly and Joesting* [1959] and *Case and Joesting* [1972]. Location of map in Figure 3.3a is indicated by solid line, locations of maps in Figure 3.4 and 3.5a are indicated by dashed line, and the red line indicates the location of the sample transect. Abbreviations: SV-Salt Valley, FV-Fisher Valley, SBV-Sinbad Valley, CV-Castle Valley, PV-Paradox Valley, MV-SPV-Moab Valley-Spanish Valley/Pine Ridge, GV-Gypsum Valley, LV-DV-Lisbon Valley-Dolores Anticline, UD-Upheaval Dome, SD-Scheafer Dome, LD-Lockhart Dome, Mts.-mountains, AZ-Arizona, CA-California, CO-Colorado, ID-Idaho, NB-Nebraska, NM-New Mexico, NV-Nevada, SD-South Dakota, WY-Wyoming.

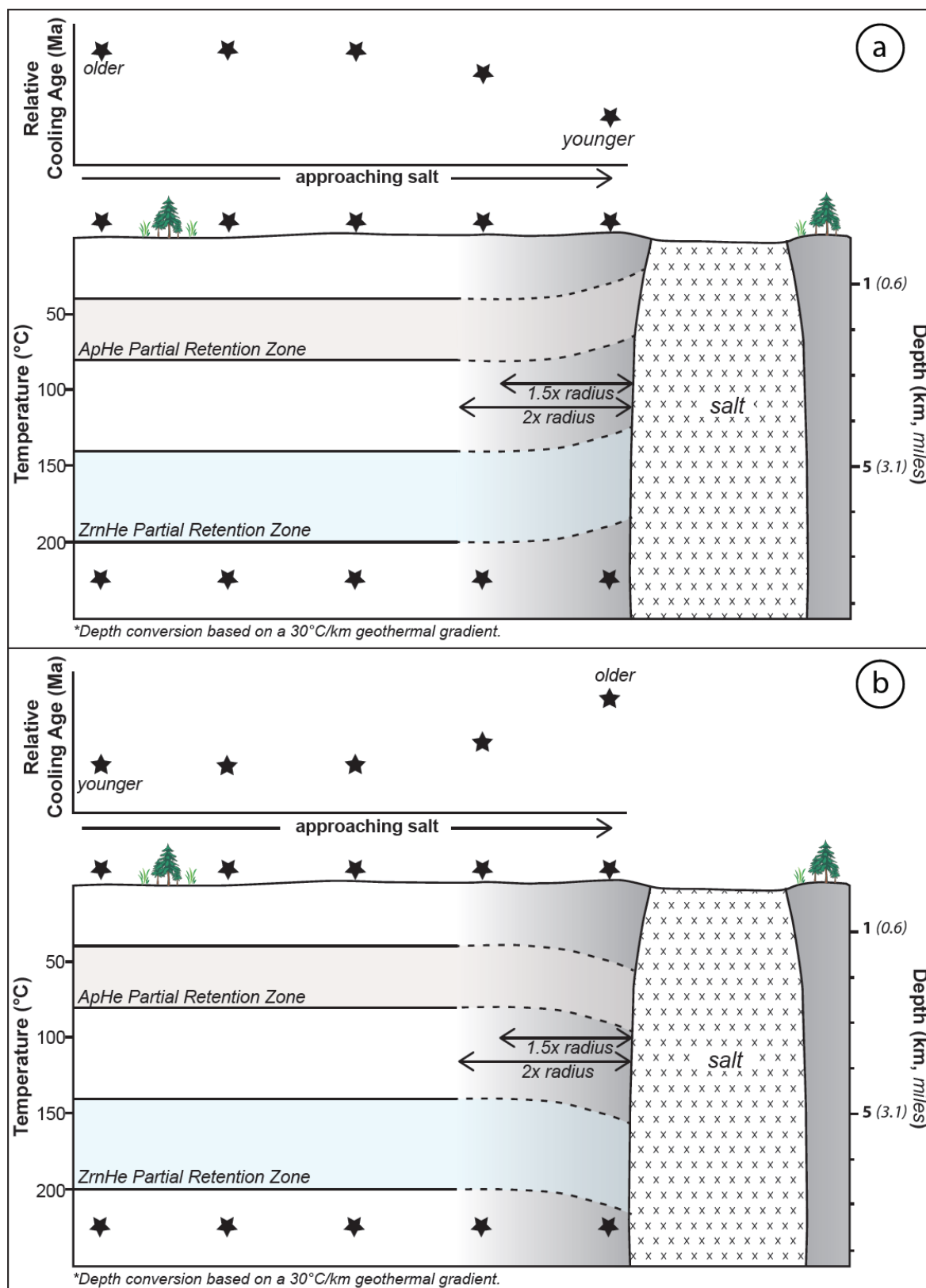


Figure 3.2 Conceptual model for use of (U-Th)/He dating

Figure 3.2: Conceptual diagram of how (U-Th)/He thermochronometry may be used to identify paleo (a) suprasalt and (b) subsalt thermal anomalies associated with a salt body presently exposed at the surface. The cross section shows the present day location of the salt body, and the predicted configuration of paleo-isotherms based on this section of the crust being located in either a suprasalt or subsalt location prior to exhumation and exposure of the salt body at the surface. Stars indicate locations of samples at depth in the past, and their present day location at the surface after exhumation. (a) (U-Th)/He cooling ages are expected to be younger than regional ages adjacent to salt bodies if paleo-isotherms were elevated due to a suprasalt thermal anomaly; (b) (U-Th)/He cooling ages are expected to be older adjacent to salt bodies if paleo-isotherms are suppressed by subsalt thermal anomalies [e.g., *Selig and Wallick, 1966; Jensen, 1983; O'Brien and Lerche, 1984; Vizgirda et al., 1985; Blackwell and Steele, 1989; Yu et al., 1992; Mello et al., 1995; Peterson and Lerche, 1995*]. Abbreviations: ApHe-apatite (U-Th)/He, ZrnHe-zircon (U-Th)/He.

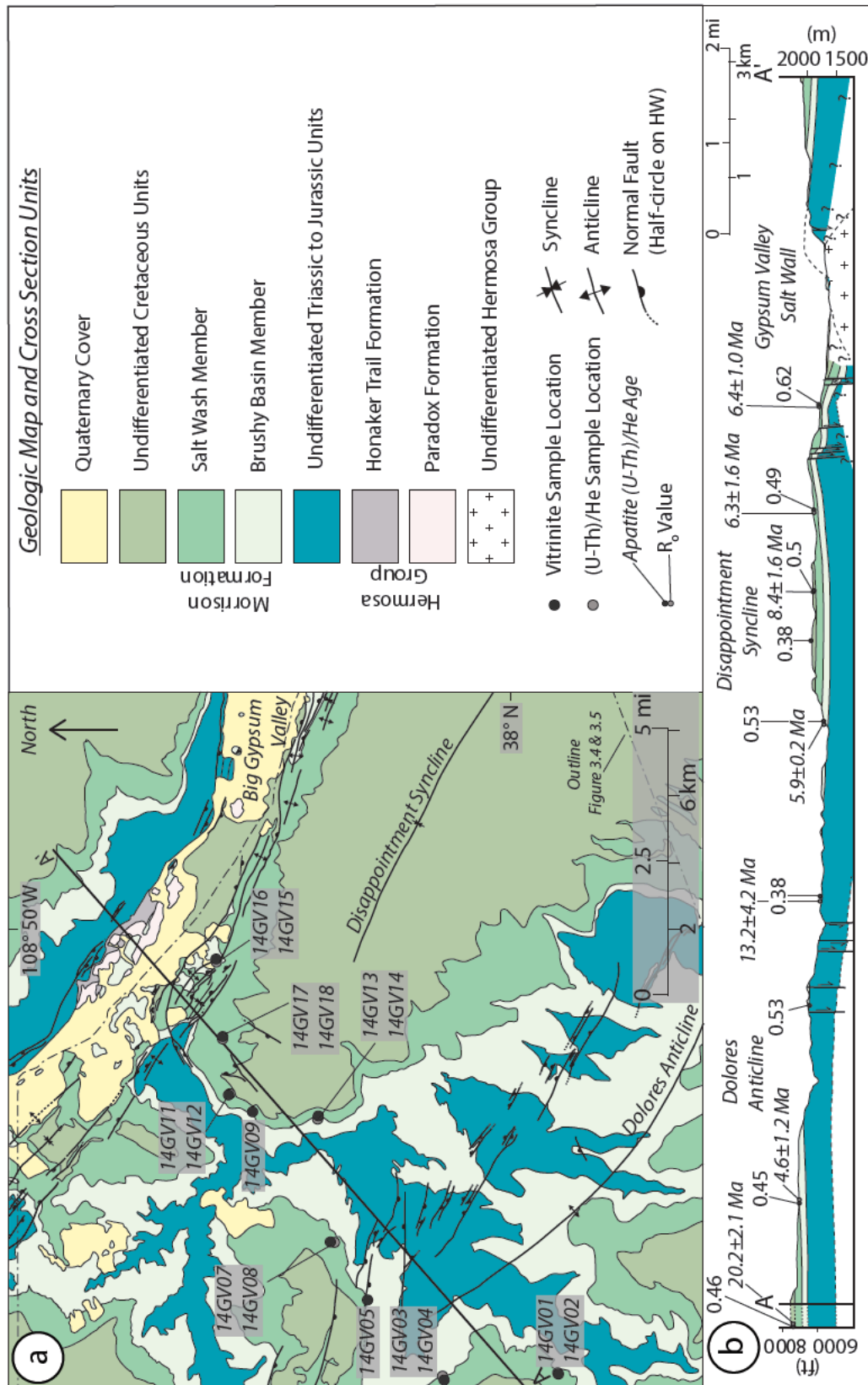


Figure 3.3 Simplified geologic map and cross section

Figure 3.3: Simplified (a) geologic map and (b) cross section showing the sample locations in the Morrison Formation, and their spatial relationship to salt structures near Gypsum Valley, redrawn from *Stokes and Phoenix* [1948]. Apatite (U-Th)/He ages and vitrinite reflectance values for each sample are projected onto the cross section line. Note that the cross section in (b) is extended beyond the original cross section of *Stokes and Phoenix* [1948], indicated by the dashed lines, in order to project samples 14GV01 and 14GV02 into the line of section.

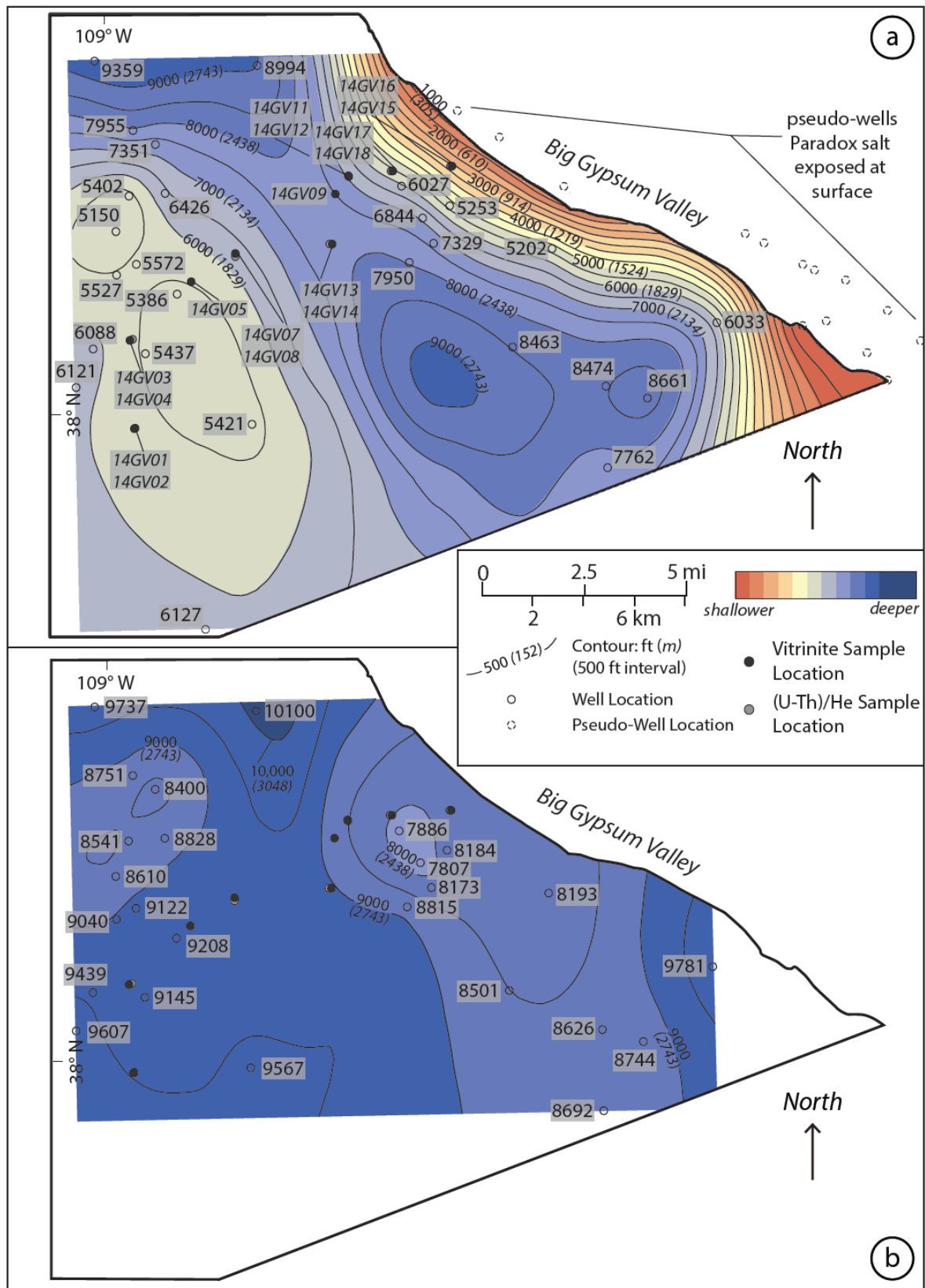


Figure 3.4 Interpolated Paradox salt surfaces

Figure 3.4: Spline interpolated (a) depth to top Paradox salt surface, and (b) depth to base Paradox salt surface from publically available well data. Location of these Paradox salt surface maps is indicated in Figure 3.1b. Depth measurements from each well to top and base Paradox salt are in labeled in feet. The depth measurements are available from Colorado Oil and Gas Conservation Commission, and reported in Table A2.2. Sample locations are labeled in (a), are the same for (b). Interpolation of surfaces and contouring were completed using ArcGIS.

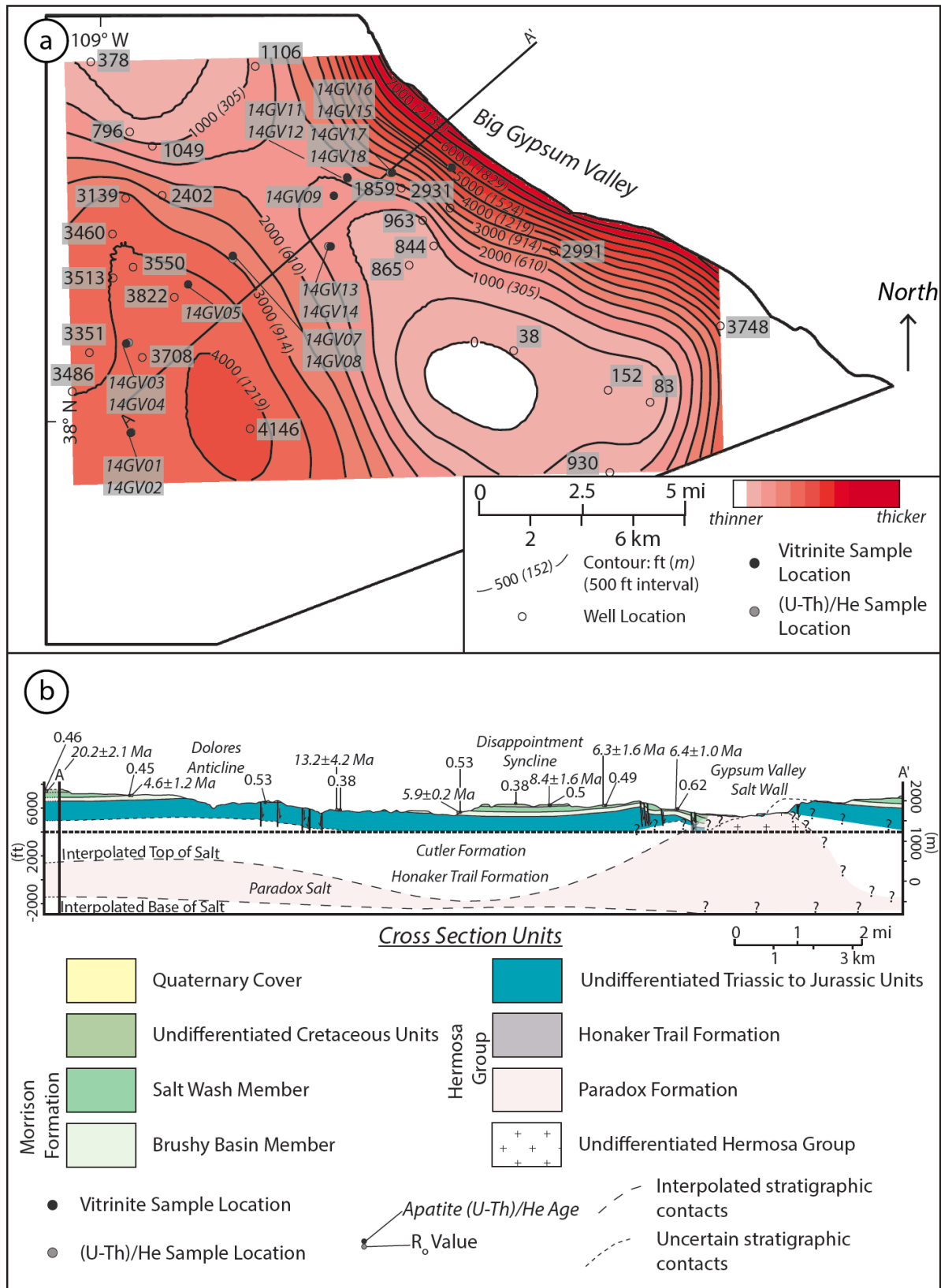


Figure 3.5 Thickness of Paradox salt and interpreted cross section

Figure 3.5: (a) Isopach map for the Paradox salt derived from subtraction of depth to top Paradox salt (Figure 3.4a) from depth to base Paradox salt (Figure 3.4b) in ArcGIS. Contours for the isopach map surface were completed in ArcGIS. Thickness measurements of Paradox salt for each well are labeled in feet. The thicknesses calculated from well measurements (labeled values) and from interpolated surfaces (contoured surface map) are in good agreement. Location of the isopach map is indicated in Figure 3.1b. (b) Interpreted cross section of *Stokes and Phoenix* [1948] (Figure 3.3b) that includes the Paradox salt at depth based on the interpolated maps from Figure 3.4. These top and base Paradox interpolated surfaces show the location of thickened salt below the Dolores Anticline, thin salt below the Disappointment Syncline, and the geometry of the Gypsum Valley salt wall. The apatite (U-Th)/He ages and vitrinite reflectance values along the horizontal transect are projected into the line of section. Note that the cross section is extended beyond the original cross section of *Stokes and Phoenix* [1948], in order to project samples 14GV01 and 14GV02 into the line of section. The dashed black line represents the original base of the *Stokes and Phoenix* [1948] cross section.

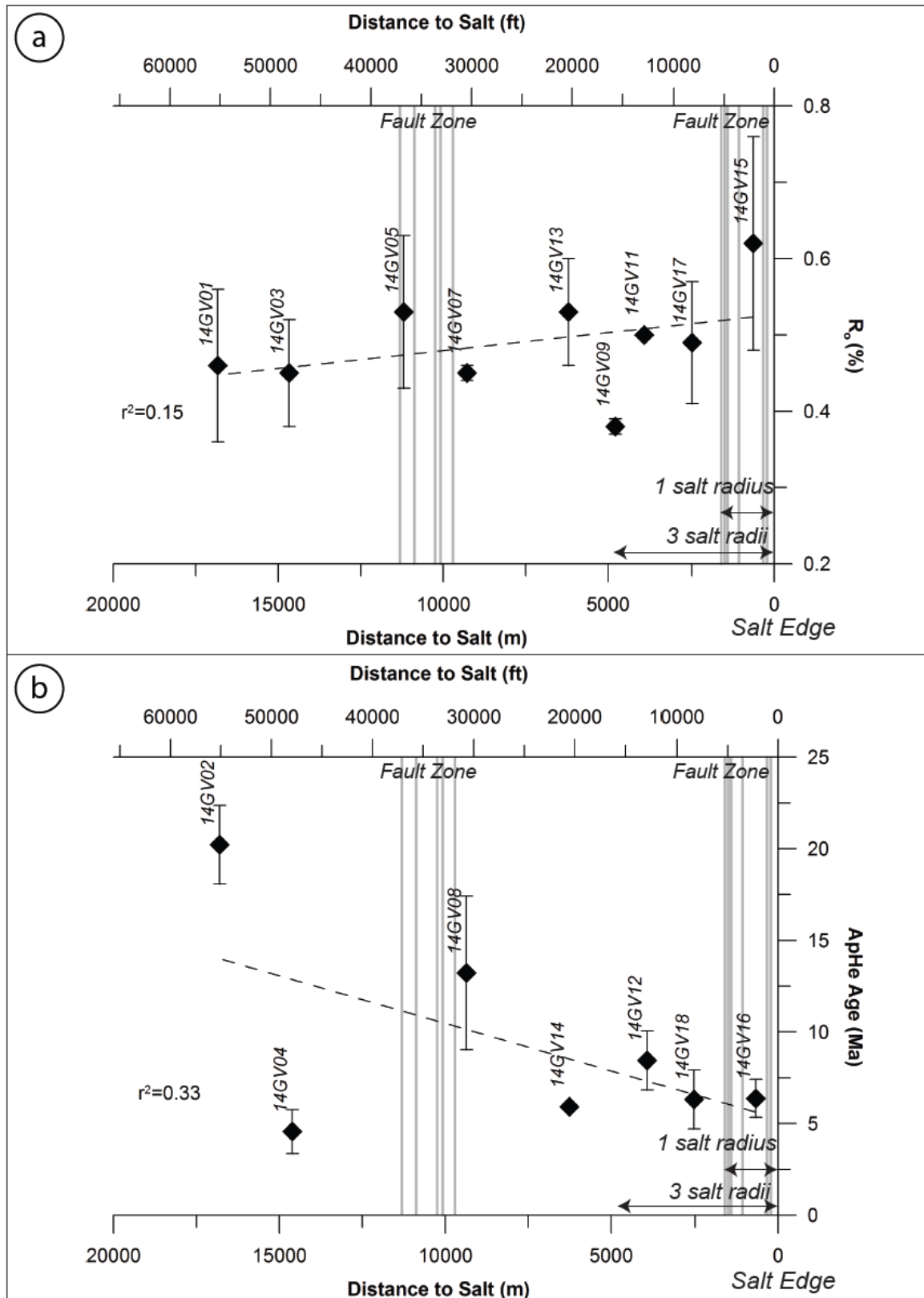


Figure 3.6 Plot of R_0 and (U-Th)/He versus distance to salt

Figure 3.6: (a) Plot of R_o values and distance from the Gypsum Valley salt wall (GVSW). Error bars shown are 1σ of the analyzed population (Table 3.2). Distance to salt was measured from the projected location of samples into the cross section A-A' to the edge of Big Gypsum Valley (Figure 3.3). Within error of measurements there is no relationship between variation in thermal maturity of samples and distance from salt. The dashed line shows a simple linear regression of the data, and the correlation is weak ($r^2=0.15$). (b) Plot of apatite (U-Th)/He (ApHe) age and distance from the GVSW. Error bars shown are $2\sigma_{wm}$ of the included aliquot population (Table 3.3 and A2.1). Distance to salt was measured from the projected location of samples into the cross section A-A' to the edge of Big Gypsum Valley (Figure 3.3). There is no unequivocal trend in these data with distance from the GVSW. The dashed line indicates a simple linear regression of the data, and positive correlation between distance and ApHe age is weak ($r^2=0.33$). The arrows on both plots indicate the width of one to three radii of the GVSW. Gray bars on both plots indicate the location of individual faults along the cross section A-A'.

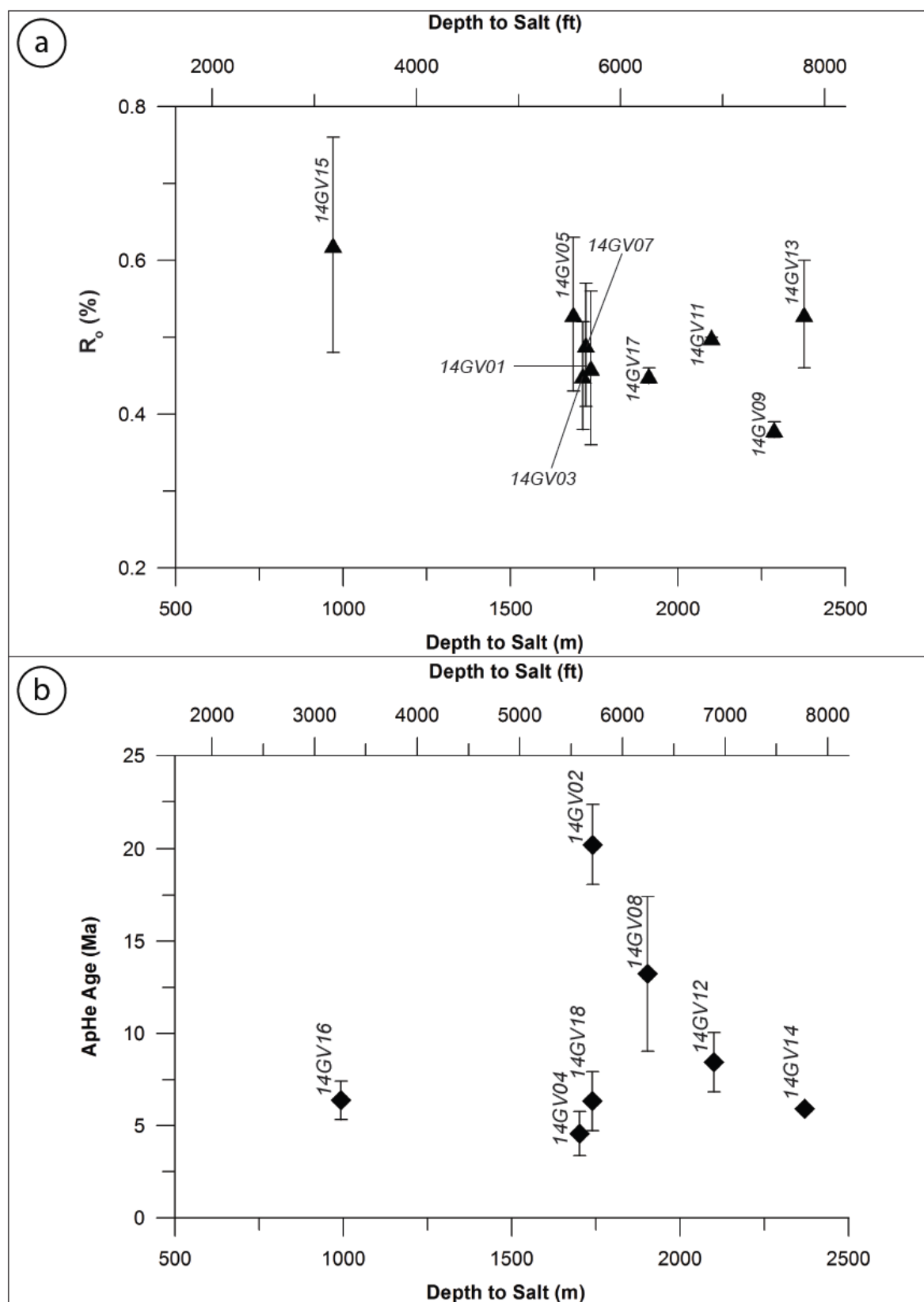


Figure 3.7 Plot of R_o and (U-Th)/He versus depth to salt

Figure 3.7: (a) Plot of depth to Paradox salt and measured R_o for each sample. Error bars shown are 1σ of the analyzed population (Table 3.2). The depth to Paradox salt is from the interpolated depth to top Paradox surface shown in Figure 3.4a. No correlation between depth to Paradox salt and R_o is observed. (b) Plot of depth to Paradox salt and apatite (U-Th)/He (ApHe) age. Error bars shown are $2\sigma_{wm}$ of the included aliquot population (Table 3.3 and A2.1). The depth to Paradox salt is from the interpolated depth to top Paradox surface shown in Figure 3.4a. No correlation between depth to Paradox salt and ApHe age is observed.

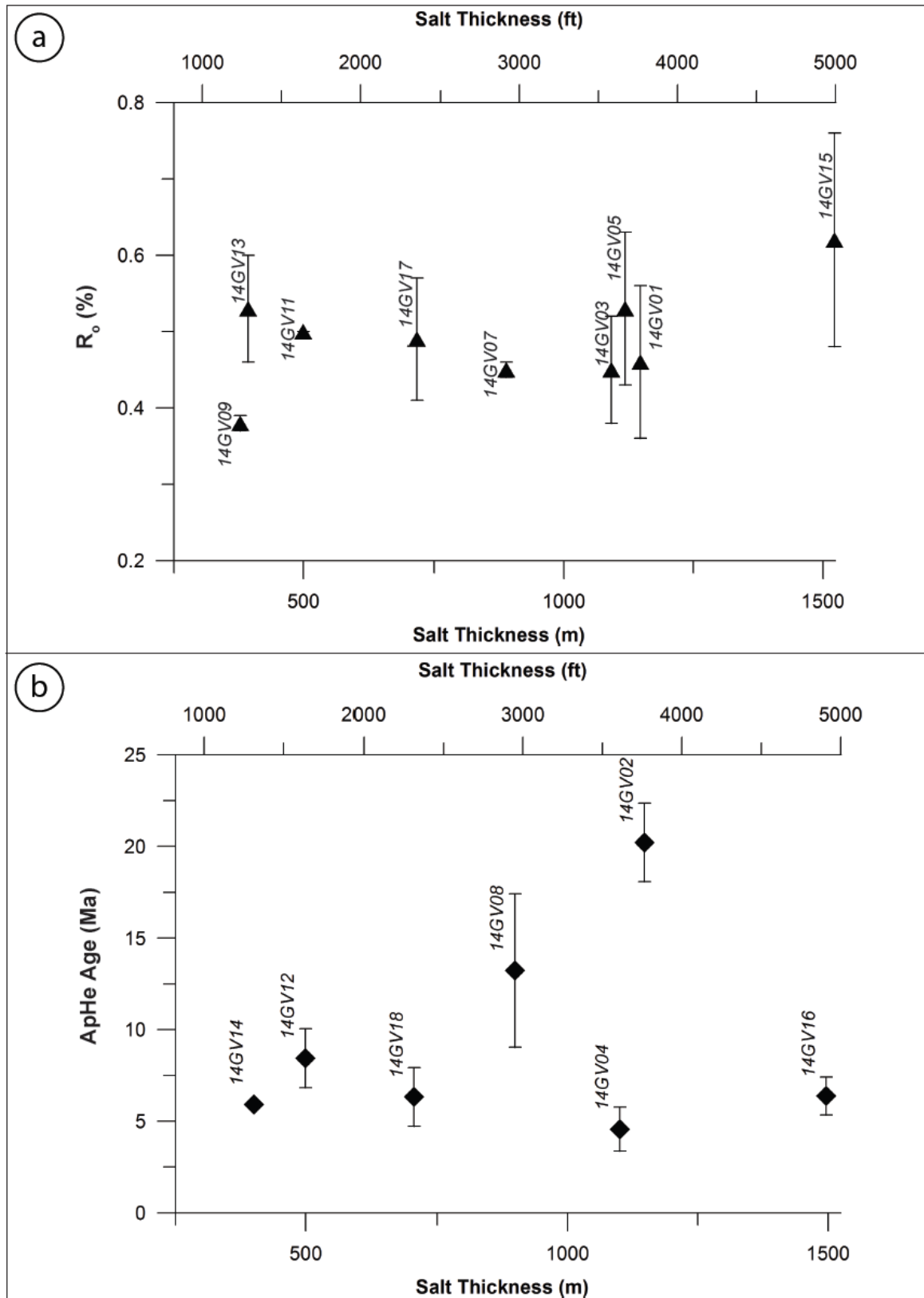


Figure 3.8 Plot of R_o and (U-Th)/He versus salt thickness

Figure 3.8: (a) Plot of thickness of Paradox salt and measured R_o for each sample. Error bars shown are 1σ of the analyzed population (Table 3.2). The thickness of Paradox salt is from the calculated isopach map shown in Figure 3.5a. No correlation between thickness of Paradox salt and R_o is observed. (b) Plot of thickness of Paradox salt and apatite (U-Th)/He (ApHe) age. Error bars shown are $2\sigma_{wm}$ of the included aliquot population (Table 3.3 and A2.1). The thickness of Paradox salt is from the calculated isopach map shown in Figure 3.5a. No correlation between depth to Paradox salt and ApHe age is observed.

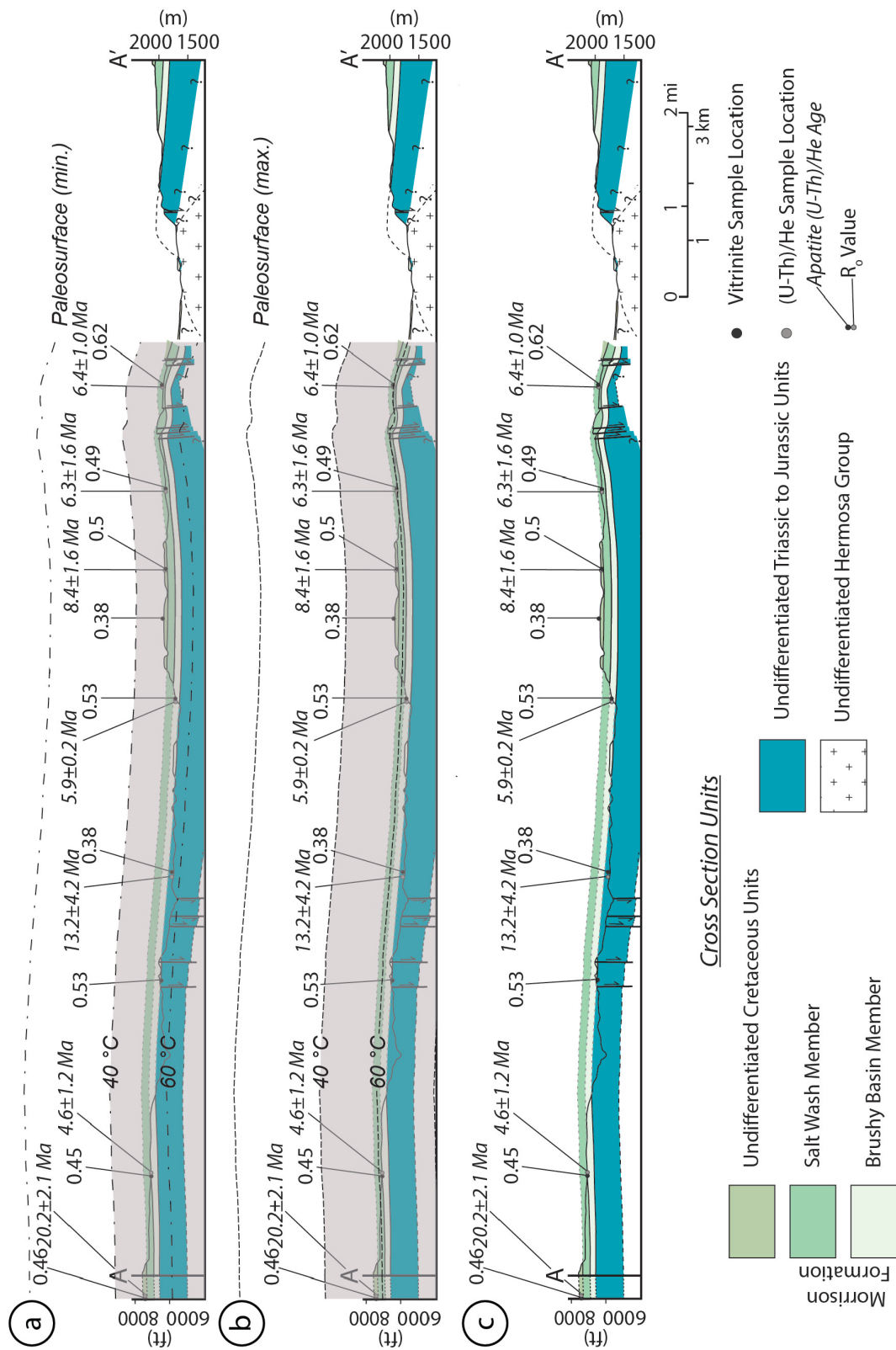


Figure 3.9 Paleo-isotherm interpretations

Figure 3.9: Conceptual reconstructions of paleo-isotherms using the cross section from *Stokes and Phoenix* [1948]. (a) Dashed and dotted lines show the minimum paleo-surface and corresponding paleo-isotherms, and (b) dashed lines show the maximum paleo-surface and corresponding paleo-isotherms. The locations of the paleo-surfaces are estimated by the burial of the Morrison Formation by Cretaceous and Tertiary strata [*Shawe et al.*, 1968; *Cater and Craig*, 1970]. The locations of the paleo-isotherms assume a $20\text{ }^{\circ}\text{C km}^{-1}$ geothermal gradient [e.g., *Bodell and Chapman*, 1982; *Hoffman*, 2009], and an average surface temperature of $10\text{ }^{\circ}\text{C}$. Conceptually, elevating the geothermal gradient will compress isotherms, and move them closer to the paleo-surfaces; however, the general geometry of isotherms will remain the same. Given the assumptions used, the maximum paleosurface (b) from *Shawe et al.* [1968] and *Cater and Craig* [1970] is overestimated because vitrinite values <0.6 are located below the $60\text{ }^{\circ}\text{C}$ paleo-isotherm. (c) Cross section from *Stokes and Phoenix* [1948] showing restoration of post-burial faulting [e.g., *Cater and Craig*, 1970], and the projected tops of the Morrison Formation over modern day topography. This reconstruction assumes thickness changes in the Morrison Formation were not significant enough to sufficiently alter the Jurassic surface prior deposition of Cretaceous and Tertiary strata.

Tables

Table 3.1 Salt thermal anomaly predictions from modeling literature

Reference	Size of Salt Thermal Anomaly	Magnitude of Positive Suprasalt Thermal Anomaly	Magnitude of Negative Subsalt Thermal Anomaly
	(# of salt body radii)	(°C)	(°C)
<i>O'Brien and Lerche [1984]</i>	1	NSP	NSP
<i>Jensen [1983]</i>	NSP	10	20
<i>Yu et al. [1992]</i>	NSP	≤ 30	NSP
<i>Jensen [1990]</i>	3	6-24	6-24
<i>Vizgirda et al. [1985]</i>	NSP	≤ 30	NSP
<i>Petersen and Lerche [1995]</i>	2-3	NSP	NSP
<i>Mello et al. [1995]</i>	NSP	NSP	≤ 85

NSP=No specific prediction

Table 3.2 Mudstone sample data

Sample	Latitude^a (°N)	Longitude^a (°W)	Elevation (m)	R_o (%)	Error^b (±1σ)	Number of R_o Analyses	TAI^c	T_{max} (°C)
14GV01	37.99424	108.99176	2151	0.46	0.1	13	2.4-2.5	390
14GV03	38.02553	108.99290	2165	0.45	0.07	5	2.4-2.5	395
14GV05	38.04588	108.96469	2062	0.53	0.1	8	2.5-2.6	342
14GV07	38.05564	108.94453	1992	0.45	0.01	2	2.4-2.5	364
14GV09	38.07602	108.89899	1826	0.38	0.01	2	2.1-2.3	347
14GV11	38.08249	108.89282	1810	0.50	NA	1	2.5	331
14GV13	38.05822	108.90097	1778	0.53	0.07	5	2.5-2.6	333
14GV15	38.08499	108.84612	1756	0.62	0.14	13	2.6-2.7	339
14GV17	38.08375	108.87289	1897	0.49	0.08	2	2.5	373

^aWGS 1984 datum^bError based on standard deviation of given population of analyses^cThermal Alteration Index (Chevron scale)

Table 3.3 Apatite (U-Th)/He data

Sample	Latitude ^a (°N)	Longitude ^a (°W)	Elevation (m)	Age ^b (Ma)	$\pm 2\sigma_{wm}$ ^c (Ma)	$\pm 2\sigma_{exp}$ ^d (Ma)	MSWD _{wm}	Aliquots
14GV02	37.99435	108.9907	2149	20.2	0.7	2.1	10.4	4 ^e
14GV04	38.02585	108.99091	2144	4.6	1.2	0.9	0.6	3 ^e
14GV08	38.05466	108.94401	1967	13.2	0.3	4.2	201.0	5
14GV12	38.08225	108.89203	1822	8.4	0.5	1.6	11.5	5 ^e
14GV14	38.05836	108.90128	1776	5.9	0.2	0.2	1.5	5 ^e
14GV16	38.08499	108.84612	1756	6.4	1.0	1.5	2.2	5
14GV18	38.08375	108.87289	1897	6.3	0.5	1.6	8.8	5

^aWGS 1984 datum^bWeighted mean of aliquots not excluded by Hampel identifier^cPropagated analytical error of weighted mean; italics indicate appropriate error for a given sample^dExpanded error calculated by multiplying the square root of MSWD_{wm} and σ_{wm} ; italics indicate appropriate error for a given sample^eAn aliquot was excluded from weighted mean age based on the Hampel identifier or outlier identified from age population distribution

Chapter 4: Preliminary map of the Red Ledges 7.5' quadrangle, White Pine and Lincoln Counties, Nevada

1. Introduction

This chapter includes the accompanying unit descriptions and methodology used to produce the new geologic map of the Red Ledges 7.5' quadrangle (Plate A3.1). The map area is located in the southern portion of the Southern Snake Range (SSR), a Cordilleran metamorphic core complex [e.g., *Coney and Harms*, 1984]. The mapped area is within the upper plate of the Southern Snake Range Décollement (SSRD), and was one of the first locations where extension along a detachment was recognized as Tertiary in age [e.g., *Armstrong*, 1972]. Portions of this quadrangle were previously mapped at the 1:147,300 scale (north of the White Pine-Lincoln county line) [*Hose and Blake*, 1970] and at the 1:200,000 scale (south of White Pine-Lincoln county line) [*Tschanz and Pampeyan*, 1961]. *Armstrong* [1972] included a generalized geologic map of the northwest corner of the quadrangle. All of these maps show multiple extensional structures, bedrock composed of Paleozoic carbonates/siliciclastics, and generalized Tertiary volcanic and Quaternary units [*Tschanz and Pampeyan*, 1961; *Hose and Blake*, 1970; *Armstrong*, 1972]. The new geologic mapping at the 1:24,000 scale documented the extensional structures in more detail, differentiated the Tertiary volcanic units using new $^{40}\text{Ar}/^{39}\text{Ar}$ dating, and defined several new Tertiary volcanoclastic and Quaternary units. This new mapping may be useful for future studies regarding the relationship between extension in the region and Tertiary volcanism/sedimentation.

2. Methods

Standard field mapping techniques as outlined by *Compton* [1985] were used to produce a new geologic map of the Red Ledges 7.5' quadrangle at the 1:24,000 scale (Plate A3.1). Two

retrodeformable geologic cross sections were completed based on the new geologic mapping [e.g., *Dahlstrom*, 1969]. Unit descriptions for the area, which are necessary for mapping, are provided below.

Ages assigned to Quaternary units are based on a comparison of the landform characteristics to the well-correlated and dated landforms described by *House et al.* [2010]. The landform characteristics of the Quaternary units documented in the descriptions include: type of geomorphic surface, relative stratigraphic relationships between the surfaces, surface morphology, degree of desert pavement development, soil petrocalcic horizon development exposed in arroyos and washes, and a description of the sedimentary deposits. Nomenclature for the landform types is from *Peterson* [1981]. Stages of petrocalcic development described from natural exposures were based on the classification scheme of *Gile et al.* [1966]. No soil pits were completed within the quadrangle; therefore, age determinations should be treated as best estimates given natural exposures.

Some Cenozoic volcanic units were analyzed using $^{40}\text{Ar}/^{39}\text{Ar}$ analyses performed at the Nevada Isotope Geochronology Lab (NIGL) to determine precise ages of the units. Five analyses were completed, and are reported in Table 4.1 and within the individual map unit descriptions. An overview of analytical procedures and all data used to calculate each $^{40}\text{Ar}/^{39}\text{Ar}$ age are reported in Appendix 4.

Paleozoic units were assigned ages compiled from Lincoln and White Pine counties maps and reports [*Tschanz and Pampeyan*, 1961; *Tschanz and Pampeyan*, 1970 and references therein; *Hose and Blake*, 1976 and references therein], as well as larger scale maps of nearby quadrangles in eastern Nevada and western Utah [*Whitebread*, 1969; *Hintze*, 1986; *Hintze and Best*, 1985].

The ages assigned to each Paleozoic unit are the broadest ranges from the literature, because no new age determinations from fossil compilations were completed in the Red Ledges quadrangle.

3. Description of Map Units

3.1 Quaternary Units

Qa: Active wash and active alluvial deposits (Holocene)

Unconsolidated silt to boulder size sediments deposited within active channels, terraces associated with the active channels, and fine grained sediments in small floodplains associated with the active channels.

Qay: Young Alluvium (Holocene to latest Pleistocene?)

This unit includes the geomorphic surfaces and deposits of inactive inset alluvial fans [e.g., *Peterson*, 1981] in the map area and some topographically higher terraces along currently active washes. These surfaces have planar to muted bar and swale topography. The inset alluvial fans are dissected near their apexes, and have up to 3 m of relief between active channel bottoms and the Qay surfaces. The amount of relief decreases downslope between the active channels and Qay surfaces to <0.25 m near the axial drainage channel of the valley. The amount of topographic relief between the Qay surfaces and the older Qai surfaces are difficult to characterize for the entire quadrangle. Southeast of Murphy's Wash the relief is ~1 m between the surfaces. In other cases, especially downslope from the apexes of the fans, the amount of topographic offset is not discernable. The Qay and Qai alluvium downslope from the apexes of the fans were differentiated on laterally continuous surfaces by using the upslope designation. The undersides of surface clasts generally have discontinuous to continuous carbonate coatings less than a few millimeters thick. Moderate to absent desert pavement is present on the surface. Clasts of reworked petrocalcic horizons and carbonate-coated clasts are present at the surface in

some locations; however, wash cuts and other natural exposures do not contain *in situ* petrocalcic soil development. Among other characteristics (i.e., relief, surface topography) the absence of a well-defined petrocalcic horizon exposed at either the surface or within wash cuts was used to differentiate the Qay and Qai units.

The deposits of the Qay unit consist of unconsolidated, poorly sorted sediment composed of silt to cobble sized material. Clasts are angular to sub-angular and are primarily Paleozoic carbonates and siliciclastic units, fragments of petrocalcic horizons in some locations, and Cenozoic volcanic units are common in fans near volcanic outcrops.

Qai: Intermediate Alluvium (middle to late Pleistocene?)

This unit is composed of the geomorphic surfaces and deposits of the remnant alluvial fans [e.g., *Peterson*, 1981] within the quadrangle. The geomorphic surface is characterized by a planar surface with rounded edges near active washes. The relief between the remnant fan surface and active wash is between ~10 to 24 m in the upper portion of the fan along John's Wash. Further downslope the relief between the active wash and remnant fan surface is ≤ 1 m. Topographic relief between the Qai and Qay unit is variable, with up to ~1 m relief southeast of Murphy's Wash and little discernible relief in other areas of the quadrangle. In these areas Qai is distinguished from Qay primarily by the presence or absence of a well-defined petrocalcic horizon exposed at either the surface or in natural wash exposures. Surface clasts of the Qai alluvium have discontinuous to continuous carbonate coatings. A thick (≤ 1 m) indurated petrocalcic soil horizon (Stage III to IV petrocalcic development [*Gile et al.*, 1966]) is often exposed at the surface or in wash cuts. A laminar horizon is locally present within the petrocalcic horizon. Desert pavement development is weak to moderate on portions of the surface, and absent where the petrocalcic horizon is exposed at the surface. On the surfaces there are angular

petrocalcic horizon fragments. On satellite imagery and in air photos, the Qai unit has a distinctively lighter color compared to the Qay unit due to the prevalence of the exhumed petrocalcic horizon and/or petrocalcic clasts at the surface.

Deposits in the unit consist of unconsolidated to poorly consolidated sediment composed of silt to cobble sized material. Clasts are angular and are primarily Paleozoic carbonates and siliciclastic material, fragments of petrocalcic horizons, and minor Cenozoic volcanic material.

Qao: **Old Alluvium** (early Pleistocene?)

This unit consists of geomorphic surfaces and sedimentary deposits exposed in the northeastern section of the quadrangle and along Murphy's Wash in the northwestern section of the quadrangle. This unit is characterized by a ballena landform morphology [e.g., *Peterson*, 1981], and has been dissected by modern channels. In some locations, the degree of relief between modern channels and the surface is up to several meters. The majority of surface clasts have continuous to discontinuous carbonate coatings. A moderate to moderately-well developed desert pavement is present on the top of the surface, and may also be present along the rounded sides of the surface near Murphy's Wash.

The deposits within the northeastern section of the quadrangle are well bedded and indurated containing angular pebble to boulder-sized clasts of Paleozoic carbonates and siliciclastic units, and Cenozoic volcanic units. In the wash cuts of deposits in the northeastern section, a sandy matrix with calcite cement surrounds the clasts. Along Murphy's Wash the deposits are unconsolidated granule to boulder sized angular clasts and sediments derived from local Paleozoic carbonates and siliciclastic units.

3.2 Cenozoic Units

Tsy: **Volcaniclastic sandstone, younger** (Oligocene?)

Poorly exposed, typically thinly bedded, medium to coarse grained, white to light green or gray lithic arkose. Contains subangular to subrounded clasts and the sandstone is moderately to moderately well sorted. Age relative to surrounding units is difficult to determine due to limited exposure. The unit is < 10 m thick in the map area.

Tv4: Volcanic unit of unknown age (Oligocene?)

White to light gray rhyolite (?) of unknown age or correlation, that contains 20 to 30% phenocrysts up to 1 mm in size. The phenocrysts include quartz and sanidine. Pumice up to 1 mm is also present. The unit is thin (<5 m), and is exposed in isolated pockets in the map area.

Tv3: Volcanic unit of unknown age (Oligocene?)

Orange to green weathering dacite of unknown age or correlation to other known volcanic units of the region; phenocryst assemblage is hornblende, quartz, sanidine, and plagioclase. Pumice is also present in this unit. This unit is not extensive and is only present in an isolated section of the map area.

Tv2: Volcanic unit of unknown correlation (Oligocene)

Ledge to cliff forming crystal-rich dacite that weathers a pink-purple to red, and is purple-reddish to red on fresh surfaces. Orientations of this unit were taken along compaction foliation defined by eroded voids from elongated pumice, fiamme, or flow banding. Phenocryst assemblage is somewhat variable, but includes quartz, plagioclase, amphibole, biotite, and sanidine. The tuff also includes pumice that varies in size from ~10-0.5 cm. A $^{40}\text{Ar}/^{39}\text{Ar}$ weighted mean age of 28.20 ± 0.55 Ma (14SR02) was determined for this unit from 21 single crystal fusion ages of plagioclase. This unit is ~130 m thick in the map area.

Tww: Wah Wah Springs Formation (Oligocene)

Light purple to pink dacitic tuff that forms cliffs and ledges. The upper portion of this unit is less resistant and weathers into more rounded outcrops. At the base of the unit, a thin vitrophyre is locally present. Orientations of this unit were taken along compaction foliation defined by eroded voids from elongated pumice, fiamme, or flow banding. Overall, the unit contains abundant phenocrysts and pumice. The phenocryst assemblage includes quartz, sanidine, plagioclase, amphibole, and biotite. The biotite crystals are significantly smaller compared to the Cottonwood Wash Tuff. Two $^{40}\text{Ar}/^{39}\text{Ar}$ age analyses were completed in the unit within the map area. Near the base of the unit an amphibole plateau age of 30.28 ± 0.35 Ma (12SR08) was determined. The upper portion of the unit is 30.13 ± 0.33 Ma (12SR09) based on a plagioclase plateau age. These ages are in good agreement with the recognized age of 30.06 ± 0.05 [Best *et al.*, 2013a]. This unit is > 152 m thick in the map area.

Tcw: **Cottonwood Wash Tuff** (Oligocene)

Light pink, pink-gray, pink-red to purple-pink dacitic tuff that contains abundant crystals and pumice. Forms cliffs and ledges; some portions contain numerous vertical joints. Some portions of the unit also form slopes, and have platy weathering. Orientations of this unit were taken along compaction foliation defined by eroded voids from elongated pumice, fiamme, or flow banding. Phenocryst assemblage includes quartz, sanidine, plagioclase, amphibole, and large biotite. Two $^{40}\text{Ar}/^{39}\text{Ar}$ weighted mean ages were determined for this unit. The basal portion of the unit is 31.54 ± 0.07 Ma based on 13 single crystal fusions of sanidine (12SR03). This age is slightly older than the age of the Cottonwood Wash Tuff [Best *et al.*, 2013a], but this unit has been included because it is too thin to map throughout the quadrangle. The middle portion of the unit is 31.05 ± 0.10 Ma based on 14 single crystal fusions of sanidine (14SR01). The latter age is

in good agreement with the established age of 31.13 ± 0.09 [Best *et al.*, 2013a]. The unit is up to ~213 m thick in the map area.

Tvb: **Volcanic breccia and sandstone** (Oligocene?)

White sandstone and volcanic breccia that is characterized by boulder to pebble sized white clasts and a pink colored matrix. Clasts within the sandstone portion of the unit contain quartz, biotite, and sanidine. Forms a white, rubble-covered slope below the cliff forming Cottonwood Wash Tuff.

Tv1: **Volcanic unit of unknown age** (Oligocene)

Pumice-rich white reworked rhyolitic tuff (?) that contains crystals of quartz, sanidine, and lithic fragments. This unit is very thin (~4 m), and is only present in one section of the map area. Mapping indicates this unit underlies the Cottonwood Wash Tuff and caps the Tco near John's Wash.

Tvc: **Volcaniclastic sandstone and mudstones, undifferentiated** (late Eocene? to Oligocene?)

Medium to coarse grained, poorly bedded, poorly exposed sandstones, and a thinly laminated mudstone derived from nearby volcanic units. The unit weathers into low rounded and banded pink, green, orange, white, and red mounds. Stratigraphic thickness is difficult to determine based on limited outcrop exposure.

Tso: **Volcaniclastic sandstones, older** (late Eocene to Oligocene?)

Light green to white and medium green, thinly bedded lithic arkose that is typically poorly exposed. The sandstone is moderately sorted, and contains subangular to subrounded clasts derived from surrounding volcanic material. Thickness is ~40 m based on cross section B-B'.

Tco: **Conglomerate** (late Eocene? to Oligocene?)

Polymict, clast-supported, pebble to boulder conglomerate that is homogeneous and indistinctly bedded. Matrix is composed of red to pink sandy matrix and is cemented with calcite. The subangular to subrounded clasts are primarily composed of carbonates, minor chert and sandstones derived from surrounding sediments, and rare felsic plutonic material. In the map area, this unit is poorly exposed and covered by Quaternary deposits. Directly north of the map area the conglomerate unit is ~40 m thick. This unit was mapped as Tco by *Whitebread* [1969].

3.3 Paleozoic Units

MPe: **Ely Limestone** (late Mississippian to Permian)

Light grey to medium grey wackestone to packstone, which forms a stair-step outcrop pattern and varies from thickly laminated to thickly bedded. Limestone ledges contain abundant chert nodules and are generally fossiliferous. Fossils include bivalves, gastropods, brachiopods, and some crinoids. The Ely Limestone is up to ~708 m thick in the map area; however, this is a minimum estimate because the regionally overlying Arcturus Formation is not present in this area.

Msw: **Scotty Wash Quartzite** (late Mississippian to early Permian)

Medium to fine grained sandstone that is reddish orange, purple-orange or brown-orange, on weathered surfaces, and tan to buff on fresh surfaces. The sandstone is a well-sorted quartz arenite that contains rounded to well-rounded grains. A distinct sugary texture is present in this unit, along with some small scale cross stratification. Overall the unit is medium to thick-bedded. Typically forms a resistant cliff that has a blocky weathering morphology. Thickness of the unit is estimated to be ~305 m in the map area.

Mc: **Chainman Shale** (Mississippian)

Dark brown to black, on fresh surfaces, thinly to thickly laminated shale. The shale is grey to orangish-grey on weathered surfaces. This unit forms topographic bowls and slopes. In general, this unit is very poorly exposed in the map area. A minimum estimate for thickness is ~216 m.

Mj: **Joana Limestone** (Mississippian)

Light grey to light bluish grey wackestone to grainstone that typically forms a prominent rounded cliff overlying the slope-forming Pilot Shale. In some parts of the map area, the more massive section of the Joana overlays a few meter thick section of thin to medium bedded limestone. The unit contains significant amounts of broken crinoids, rugose corals, and some bivalves. Some cross stratification and chert nodules are present, along with abundant calcite-filled veins. Weathered surfaces commonly have well-developed rillenkarren morphology. Due to structural complexities, it is only possible to estimate the minimum thickness of the Joana limestone at ~101 m from map pattern. The cross sections suggest the Joana may be as thick as ~122 m thick.

MDp: **Pilot Shale** (late Devonian to early Mississippian)

Light orangish yellow to light greenish grey calcareous siltstone to shale, that varies from thinly laminated to thinly bedded. Typically forms slopes and topographic bowls in the map area, and is usually poorly exposed. The fragments of rocks exposed on slopes make a distinct clinking sound when moved. In the map area it is up to 202 m thick.

Dg: **Guilmette Formation** (middle to late Devonian)

Dark to medium grey to purple-grey thinly to thickly bedded and massive limestone and dolostone that alternately forms ledgy slopes and rounded resistant cliffs. Some rounded resistant cliffs correspond to ancient bioherms, and some sections of the formation are fossiliferous. Fossils present include abundant gastropods, crinoids, stromatoporoids, and brachiopods. Locally

red and yellow altered and brecciated zones are present. White and yellowish sparry calcite occurs in some veins and fractures. Poorly to moderately developed rillenkarren is present in exposures in rounded cliffs. The unit is ~704 m thick in the map area.

Ds: **Simonson Dolomite** (middle Devonian)

Alternating medium to dark brown and light to medium grey dolostone that is thinly laminated to thinly bedded. Wavy laminae are present, but even laminations and bedding are more common. Some layers contain smooth shelled brachiopods. This unit typically weathers into stair-step, laterally continuous ledges. Thickness of this unit is ~291 m, but this is likely an underestimate of true stratigraphic thickness due to structural complexities in the map area.

Dse: **Sevy Dolomite** (early to middle Devonian)

Light grey, unfossiliferous mostly thickly bedded dolostone. Generally has a homogeneous crystalline or sugary texture. The unit weathers into laterally continuous, evenly bedded ledges. The Sevy Dolomite is up to ~116 m thick in the map area; however, this is only a minimum estimate since the base of the unit is never exposed. *Whitebread* [1969] estimated a thickness of ~244 m for the SSR, and this value was used when constructing cross sections.

SOLF: **Laketown and Fish Haven Dolomite, undivided** (late Ordovician to Silurian)

Dark gray to dark brown weathering dolostone that contains thick tan chert bands that give outcrops an overall light and dark banded appearance. Fresh surfaces of the unit are extremely dark, almost black, and are finely crystalline. Stratigraphic thickness of the unit is impossible to estimate in the map area due to structural complexities. A thickness of ~198 m was used in cross section construction based on an estimate from *Drewes* [1958] for the SSR.

Oe: **Eureka Quartzite** (middle Ordovician)

Light whitish grey to orangish white sandstone that is heavily altered along faults in the map area. Due to alteration it is difficult to distinguish primary sedimentary structures and characteristics. Typically has red and orange silica-filled fractures. Stratigraphic thickness is not possible to estimate in the map area because the unit is heavily faulted. *Drewes* [1958] estimated a thickness of ~110 m for the SSR, and this estimate was used for cross sections.

Op: Pogonip Group, undivided (early to middle Ordovician)

The undivided Pogonip Group mostly consists of the medium gray to dark gray, thickly bedded, crystalline House Limestone in the map area. This unit typically contains orange-red or yellow-red mottling, with sparse chert nodules present. The contact between the underlying Notch Peak Formation and Pogonip Group was mapped at the transition from a more rounded outcrop characteristic below to a ledgy outcrop characteristic above. This morphologic change coincides with a greater amount of chert present, a regionally recognized marker for the transition from the Notch Peak Formation to the House Limestone. The Pogonip Group was mapped as undivided, because near the Murphy Wash Fault zone the rock units are not easily differentiated into the constituent members of the Pogonip Group due to deformation. These undifferentiated units consist of an unfossiliferous, thinly laminated dark gray carbonate and a thinly bedded, unfossiliferous, cherty dark blue-gray carbonate. The Pogonip Group is at least 170 m thick in the map area; however, this is a minimum estimate because the contact with the overlying Eureka Quartzite is not exposed. A thickness of ~914 m was estimated by *Drewes* [1958] for the Pogonip Group in the SSR, and this value was used in the cross sections.

OCnp: Notch Peak Formation (late Cambrian)

Medium gray to dark gray, coarsely to finely crystalline, massive to thinly bedded, carbonate that contains calcite veining and rare chert nodules. This unit typically forms sheer cliff faces, but

may also form more rounded cliff sections interrupted by small slopes. The upper portion of the unit, near the contact with the overlying Pogonip Group, has a rounded outcrop characteristic and contains stromatolites. The unit is ~264 m thick in the map area; however, the Murphy Wash Fault truncates the base of the section. *Whitebread* [1969] estimated the thickness of the Notch Peak Formation at ~518 m directly north of the map in the SSR, and this estimate was used in cross section construction.

4. Structure

4.1 Pre-Oligocene unconformity

Previous researchers have suggested that Tertiary volcanic units near the map area were deposited on relatively unfaulted, low-relief Paleozoic units [e.g., *Armstrong*, 1972; *Miller et al.*, 1983]. The new mapping shows instead that the pre-Tertiary or pre-Oligocene unconformity is variable. Locally the unconformity occurs between Tertiary volcanic units and the Devonian Guilmette Formation. In other locations in the map area it occurs between Tertiary sedimentary units and Mississippian to Permian units. Based on typical unit thicknesses in the map area, locally up to ~1237 m of Devonian to Permian stratigraphy must have been removed prior to Tertiary volcanism. This finding is in agreement with the exhumation map of *Long* [2012]. These interpretations indicate that the map area was not an unfaulted low-relief region as previously suggested [e.g., *Armstrong*, 1972; *Miller et al.*, 1983].

4.2 Cross section A-A'

The A-A' cross section is retrodeformable given material moving in and out of the plane of section as indicated on the structures. Oblique motion on the easternmost east-dipping normal fault and a west-dipping normal fault in the central portion of the cross section are consistent with slickenlines measured within these fault zones. The mean vector of these measurements are

indicated on the map. Fault bends near the cross section location provide additional evidence for oblique motion along normal faults within the line of section. This section also indicates that the Paleozoic stratigraphy within the northern portion of the map area were folded prior to later normal faulting. The folding of the Paleozoic stratigraphy shown in A-A' may be related to folding in the Late Jurassic to Eocene western Utah thrust belt [*Greene, 2014*] to the east of the map area.

4.3 Cross section B-B'

This cross section is retrodeformable given oblique slip, as indicated in the cross section, along a presently east-dipping thrust fault. Although, this currently east-dipping thrust appears to be a normal fault, restoration of the pre-Oligocene unconformity to horizontal is consistent with a west-dipping thrust fault. The retrodeformation of the cross section shows that thrust faulting occurred in the map area prior to the Oligocene. The thrust faults located in B-B' are also consistent with a thrust fault in the north-central portion of the map. The thrust faults within B-B' and mapped in the north-central portion of the quadrangle may be related to thrust faulting documented within the Late Jurassic to Eocene western Utah thrust belt of *Greene [2014]* located directly east of the map area.

Tables

Table 4.1 $^{40}\text{Ar}/^{39}\text{Ar}$ ages of volcanic units in the Red Ledges quadrangle

Sample	Latitude ^a (°N)	Longitude ^a (°W)	Age (Ma)	$\pm 1\sigma$ (Ma)	Age Type	Mineral Phase Analyzed	Analysis Type	Interpreted Volcanic Unit ^b
12SR03	38.6573	114.2818	31.54	0.07	Weighted Mean Age	Sanidine	Single Crystal Fusion	Cottonwood Wash Tuff
14SR01	38.7103	114.2687	31.05	0.10	Weighted Mean Age	Sanidine	Single Crystal Fusion	Cottonwood Wash Tuff
12SR08	38.6585	114.2777	30.28	0.35	Plateau Age	Amphibole	Bulk Sample	Wah Wah Springs Formation
12SR09	38.6570	114.2757	30.13	0.33	Plateau Age	Plagioclase	Bulk Sample	Wah Wah Springs Formation
14SR02	38.7099	114.2649	28.20	0.55	Weighted Mean Age	Plagioclase	Single Crystal Fusion	Unknown

^aWGS 1984 datum

^bBased on ages reported for volcanic units by *Best and Grant* [1987] and *Best et al.* [2013a]

Appendix 1: Supplemental material for Chapter 2

1. Overview of Contents

This appendix contains a supplementary figure (Figure A1.1) and two tables referenced in Chapter 2 (Table A1.1 and A1.2). This appendix also contains information about reprinting of the article presented in Chapter 2 (Figure A1.2).

1.2 Paleodepth Reconstruction

Figure A1.1 is a paleodepth reconstruction of the zircon and apatite (U-Th)/He data from this study (ZrnHe; ApHe) and zircon and apatite fission track data from *Miller et al.* [1999] (ZrnFT; ApFT) using the retrodeformable cross sections from *McGrew* [1993]. The depth errors associated with the reconstruction are difficult to quantify based on the method of reconstruction. The use of the retrodeformable cross section requires projecting spatially distributed samples in the Southern Snake Range into the present day cross section line. It is difficult to estimate how accurate these projections are for samples located far from the line of section given possible structural complexity of the footwall of the Southern Snake Range Décollement (SSRD). Following projection of samples into the post-extensional cross section, the locations of the samples were determined in the pre-extensional cross section by placing them based on their relative positions to the Snake Creek-Williams Canyon pluton, and surrounding strata. The errors associated with this methodology are difficult to estimate. From the pre-extensional cross section paleodepths were measured from the sample to the top of the uppermost strata. However, it is not clear from the pre-extensional cross section if the interpretation includes the youngest Paleozoic units of the Southern Snake Range (e.g., Joana Limestone, Chainman Shale) in the upper plate of the SSRD. The presence or absence of these units would increase or decrease the overburden for several of the samples. As a result of these issues, the data are plotted without depth error bars.

There are no clear trends in the cooling ages that show partial retention zones or partial annealing zones that could be used to understand rates and timing of exhumation. Additionally, the ZrnFT and ApHe cooling ages are small data populations to analyze. ApFT ages do not clearly show a trend, other than most cooling ages agree within error over ~2 km of paleodepth. The ZrnHe cooling ages may show the characteristic decrease in age with increase in depth [e.g., *Stockli et al.*, 2003]; however, there are three Eocene ages that are clear outliers in this trend.

1.3 Reprint permission

Please see Figure A1.2 for correspondence with *Tectonics* for permission to reprint the previously published journal article in this dissertation.

1.4 Supporting Tables

The supporting tables A1.1 and A1.2 contain the individual aliquot dates for each zircon and apatite (U-Th)/He analysis. These individual aliquot dates were used to calculate the error-weighted mean dates for each sample shown in Table 2.1 of Chapter 2. See section 4 of Chapter 2 for sample collection explanation. See section 4.1 of Chapter 2 for an explanation of the (U-Th)/He analytical procedures, treatment of outliers, and error-weighted mean age calculation used by the Group 18 Laboratories at Arizona State University.

Appendix 1 Figures

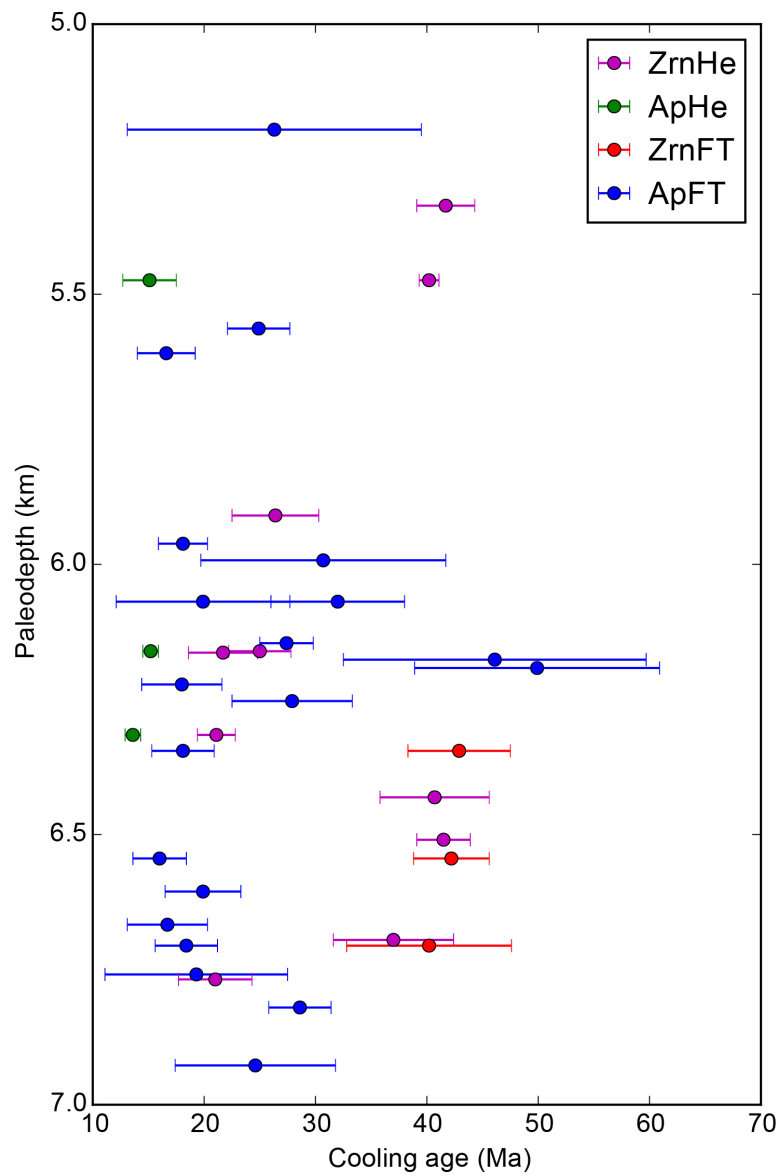


Figure A1.1 Paleodepth reconstruction

Figure A1.1: Zircon and apatite (U-Th)/He data from this study and zircon and apatite fission track data from *Miller et al.* [1999] were used to create a paleodepth reconstruction using the retrodeformable cross sections of *McGrew* [1993]. Ages and errors for (U-Th)/He data are quoted in Table 2.1 of the text. Ages and errors for the fission track data are from *Miller et al.* [1999]; however, errors were plotted as 2σ . Depth errors are difficult to quantify using the reconstruction method due to uncertainties in overburden amounts and placement of samples in the pre-extensional cross section of *McGrew* [1993]. No definable age trends are present in the ZrnFT, ApHe, or ApFT data. A possible decrease in ZrnHe ages with depth is present, except for three significant Eocene aged outliers. Abbreviations: ZrnHe-zircon (U-Th)/He, ApHe-apatite (U-Th)/He, ZrnFT-zircon fission track, ApFT-apatite fission track.

publications <publications@agu.org>
To: Sarah Evans <evanss3@unlv.nevada.edu>

Thu, Nov 19, 2015 at 7:33 AM

Dear Sarah,

Thank you for your note. AGU does not require formal permission to reproduce articles for educational purposes provided that full attribution is provided. This includes inclusion in dissertations.

Please let us know if you need anything further.

Best regards,

Joan Minnehan

From: Sarah Evans [mailto:evanss3@unlv.nevada.edu]
Sent: Wednesday, November 18, 2015 4:39 PM
To: publications <publications@agu.org>
Subject: Publication Question

Dear Publications Team at AGU,

I have question regarding the use of published material from the AGU journal *Tectonics*. I am Ph.D. student, and I have a published article (doi:10.1002/2015TC003913) that I need to include as a chapter of my dissertation in order to complete my degree.

My question is do I need to have a special publication permission, or some sort of release form, in order to have the material published without infringing on copyrights in my dissertation? The published material in the dissertation will not be in the same format as the journal article, but it will be the same exact material. I read the information on the website about publication on the author's website, but I didn't find anything explicit for republishing in dissertations. If I need to direct this question to another party please let me know. Thank you for your help in this matter.

Best,

Sarah Evans

--

Sarah L. Evans
Ph.D. Candidate

Department of Geoscience
University of Nevada, Las Vegas

TEC 122B

evanss3@unlv.nevada.edu

Figure A1.2 Previously published journal article reprint permission

Appendix 1 Tables

Table A1.1 Replicate zircon (U-Th)/He analyses

Aliquot ^a	Age ^b	±2σ ^c	U	±1σ ^d	Th	±1σ ^d	Th/U	eU ^e	⁴ He ^f	±1σ ^c	Radius (1) ^g	Radius (2) ^g	Length ^h	Termination Length (1) ⁱ	Termination Length (2) ⁱ	Mass	Fr ^j
(Ma)	(Ma)	(μmol/g)	(μmol/g)	(μmol/g)	(μmol/g)	(μmol/g)	(μmol/g)	(μmol/g)	(μmol/g)	(μmol/g)	(μm)	(μm)	(μm)	(μm)	(μm)	(μg)	
<i>Snake Creek Samples</i>																	
12SC01: 38.94442°N, 114.29828°W; 3316 m																	
12SC01 z01	39.3	1.1	3.338	0.027	0.849	0.004	0.25	3.54	0.178	0.002	30.1	30.3	181.2	26.0	21.7	2.5	0.696
12SC01 z02	42.0	1.2	2.611	0.021	1.666	0.007	0.64	3.00	0.162	0.002	30.3	30.1	164.8	22.7	17.9	2.3	0.689
12SC01 z03	41.0	1.2	20.130	0.161	7.654	0.031	0.38	21.93	1.155	0.014	38.6	33.8	248.1	20.7	19.8	5.4	0.746
12SC01 z04	45.8	1.4	1.470	0.012	0.820	0.004	0.56	1.66	0.098	0.001	34.5	39.0	189.2	49.0	39.0	3.3	0.730
12SC03: 38.94246°N, 114.28855°W; 3224 m																	
12SC03 z01	41.1	1.2	6.438	0.050	2.206	0.009	0.34	6.96	0.367	0.004	42.3	45.0	266.8	32.3	22.4	8.2	0.784
12SC03 z02	34.7	1.0	5.457	0.043	1.653	0.007	0.30	5.85	0.260	0.003	37.2	37.7	253.4	21.1	23.4	5.8	0.755
12SC03 z03	39.7	1.1	7.043	0.054	2.070	0.010	0.29	7.53	0.384	0.005	61.8	57.8	276.1	32.1	39.9	15.2	0.833
12SC03 z04	39.9	1.1	2.938	0.024	0.824	0.004	0.28	3.13	0.160	0.002	56.2	60.4	353.2	61.6	52.9	17.5	0.835
12SC04: 38.94184°N, 114.27149°W; 2944 m																	
12SC04 z01	22.0	0.6	3.213	0.026	1.241	0.005	0.39	3.50	0.099	0.001	45.4	73.4	177.6	49.4	64.1	6.3	0.792
12SC04 z02	34.7	1.0	3.680	0.029	1.066	0.005	0.29	3.93	0.175	0.002	36.2	31.8	214.3	30.6	20.1	3.9	0.728
12SC04 z03	25.8	0.7	0.901	0.007	0.699	0.003	0.78	1.07	0.035	0.000	45.4	47.2	371.7	72.9	70.5	11.0	0.796
12SC04 z04	26.6	0.7	1.372	0.011	1.150	0.005	0.84	1.64	0.056	0.001	54.2	44.2	385.7	75.0	77.2	12.7	0.804
12SC04 z05	29.3	0.9	4.026	0.037	0.889	0.006	0.22	4.24	0.159	0.002	34.0	42.1	224.2	28.1	33.8	4.9	0.751
12SC05: 38.93781°N, 114.26141°W; 2666 m																	
12SC05 z01	25.5	0.7	3.876	0.033	1.071	0.005	0.28	4.13	0.135	0.002	53.0	59.9	320.9	72.3	40.1	14.5	0.827
12SC05 z02	24.9	0.7	5.276	0.048	1.739	0.009	0.33	5.68	0.182	0.002	62.9	56.0	451.7	35.1	52.9	25.8	0.843
12SC05 z03	27.6	0.8	6.119	0.053	1.395	0.006	0.23	6.45	0.228	0.003	47.8	42.2	373.6	23.6	31.9	12.6	0.798
12SC05 z04	21.1	0.6	3.940	0.035	0.987	0.004	0.25	4.17	0.113	0.001	47.9	48.7	301.3	31.1	58.4	10.5	0.803
12SC05 z05	28.9	0.9	3.488	0.033	0.824	0.006	0.24	3.68	0.136	0.002	45.0	47.1	361.9	58.2	55.5	11.3	0.799
12SC06: 38.93544°N, 114.25247°W; 2671 m																	
12SC06 z01	26.7	0.7	3.280	0.025	1.217	0.006	0.37	3.57	0.122	0.001	33.1	35.9	282.1	41.2	36.4	5.1	0.738
12SC06 z02	19.2	0.5	2.356	0.018	0.904	0.005	0.38	2.57	0.063	0.001	58.0	48.7	464.2	69.2	78.8	19.2	0.825
12SC06 z03	18.9	0.5	4.547	0.035	1.466	0.007	0.32	4.89	0.118	0.001	37.7	31.1	254.5	24.0	24.4	4.8	0.735
12SC06 z04	27.6	0.8	5.025	0.039	1.788	0.008	0.36	5.45	0.193	0.002	40.8	41.3	280.4	41.1	37.9	7.2	0.774
12SC06 z05	19.7	0.6	2.690	0.025	0.968	0.006	0.36	2.92	0.074	0.001	33.6	34.7	239.4	37.7	33.8	4.2	0.731
12SC06 z06	25.2	0.7	5.757	0.053	1.089	0.007	0.19	6.01	0.194	0.002	43.7	38.4	332.8	31.3	27.3	9.2	0.779
12SC07: 38.92962°N, 114.24306°W; 2538 m																	
12SC07 z01	20.6	0.6	4.239	0.034	1.804	0.009	0.43	4.66	0.123	0.001	53.0	49.1	315.2	34.8	40.4	12.8	0.814
12SC07 z02	19.6	0.6	3.206	0.026	1.202	0.006	0.38	3.49	0.088	0.001	39.9	33.2	384.6	33.2	38.7	8.3	0.757
12SC07 z03	21.4	0.6	2.633	0.021	1.103	0.005	0.42	2.89	0.079	0.001	53.7	47.3	303.0	31.6	38.0	12.1	0.811
12SC07 z04	23.9	0.7	2.641	0.022	1.215	0.006	0.46	2.93	0.090	0.001	45.9	47.7	344.0	51.8	44.3	11.4	0.801
12SC08: 38.92229°N, 114.2328°W; 2373 m																	
12SC08 z01	18.2	0.5	2.132	0.016	0.704	0.003	0.33	2.30	0.054	0.001	64.7	62.5	348.4	69.8	74.4	19.0	0.844
12SC08 z02	20.6	0.6	2.977	0.024	1.129	0.005	0.38	3.24	0.085	0.001	35.7	34.0	307.3	43.3	40.0	5.7	0.742
12SC08 z03	21.9	0.6	3.333	0.025	0.936	0.004	0.28	3.55	0.100	0.001	38.2	34.7	211.8	28.7	40.8	4.1	0.740
12SC08 z04	26.6	0.7	3.205	0.025	1.891	0.008	0.59	3.65	0.124	0.002	37.5	34.9	280.4	22.4	33.4	5.9	0.748
<i>Williams Canyon Samples</i>																	
12WC01: 38.94735°N, 114.32922°W; 2710 m																	
12WC01 z01	33.3	0.9	8.013	0.061	5.164	0.026	0.64	9.23	0.393	0.005	34.5	36.6	231.4	24.1	22.3	4.7	0.739
12WC01 z03	38.0	1.1	2.755	0.021	0.818	0.006	0.30	2.95	0.144	0.002	43.2	35.2	182.1	51.7	52.9	3.2	0.735
12WC01 z04	42.8	1.3	5.823	0.054	1.765	0.013	0.30	6.24	0.343	0.004	47.6	41.8	222.5	35.3	34.6	6.5	0.781
12WC02: 38.94838°N, 114.33656°W; 2567 m																	
12WC02 z01	40.4	1.1	1.946	0.015	0.759	0.004	0.39	2.12	0.110	0.001	43.2	40.3	213.9	52.9	42.2	4.9	0.763
12WC02 z02	40.4	1.1	3.489	0.027	0.966	0.005	0.28	3.72	0.193	0.002	34.9	37.2	205.9	30.0	44.0	3.8	0.736
12WC02 z03	26.3	0.7	18.684	0.144	5.170	0.026	0.28	19.90	0.672	0.008	31.6	26.8	202.5	23.9	28.3	2.6	0.690
12WC02 z04	44.0	1.2	8.688	0.066	3.271	0.016	0.38	9.46	0.534	0.006	36.4	38.8	257.4	30.9	27.7	5.7	0.755
12WC03: 38.95118°N, 114.34489°W; 2472 m																	
12WC03 z01	35.2	1.0	2.993	0.023	0.698	0.003	0.23	3.16	0.143	0.002	39.5	34.0	222.4	20.2	29.6	4.7	0.746
12WC03 z02	44.3	1.3	5.218	0.041	1.526	0.006	0.29	5.58	0.317	0.004	40.5	37.5	242.5	31.6	49.5	5.3	0.758
12WC03 z03	50.1	1.4	4.368	0.034	1.161	0.005	0.27	4.64	0.299	0.004	46.2	39.3	258.0	28.0	44.4	7.1	0.778
12WC03 z04	39.6	1.1	4.573	0.036	1.050	0.005	0.23	4.82	0.245	0.003	46.1	46.4	252.9	22.3	34.4	8.6	0.793
12WC03 z05	39.5	1.2	4.572	0.044	0.734	0.005	0.16	4.74	0.240	0.003	32.1	30.4	187.6	28.5	32.3	2.7	0.704

^aAliquots used to calculate weighted mean age in Chapter 2. Italicized rows are excluded outliers based on Hampe's identifier.

^bAlpha ejection corrected zircon (U-Th)/He age.

^cPropagated analytical error; does not take into account error induced by natural U and Th zoning.

^dAnalytical error of measurement.

^eEffective U concentration (eU) calculated based on equation $eU = U + 0.235Th$ from Shuster *et al.* [2006]

^f F_T corrected ⁴He concentration.

^gAverage radius from three measurements on a grain face. (1) and (2) indicate averages from two grain faces measured.

^hAverage grain length from two measurements.

ⁱAverage termination length from measurements on two faces of the zircon grain. (1) and (2) indicate the averaged measurements for each termination on the zircon grain.

^j F_T correction following method outlined in Hourigan *et al.* [2005]

Table A1.2 Replicate apatite (U-Th)/He analyses

Aliquot ^a	Age ^b (Ma)	$\pm 2\sigma^c$ (Ma)	U ($\mu\text{mol/g}$)	$\pm 1\sigma^d$ ($\mu\text{mol/g}$)	Th ($\mu\text{mol/g}$)	$\pm 1\sigma^d$ ($\mu\text{mol/g}$)	Th/U	eU ^e ($\mu\text{mol/g}$)	⁴ He ^f ($\mu\text{mol/g}$)	$\pm 1\sigma^e$ ($\mu\text{mol/g}$)	Radius ^g (μm)	Length ^h (μm)	Mass (μg)	F _T ^h
<i>Snake Creek Samples</i>														
12SC03: 38.94246°N, 114.28855°W; 3224 m														
12SC03 a01	17.6	0.8	0.025	0.00037	0.069	0.0009	2.7864	0.0410	0.0009	0.000020	40.7	175.2	2.4	0.66
12SC03 a02	13.0	0.4	0.076	0.00071	0.077	0.0008	1.0126	0.0938	0.0016	0.000021	61.1	162.0	5.0	0.75
12SC03 a03	16.1	0.7	0.041	0.00058	0.087	0.0011	2.1473	0.0610	0.0013	0.000024	41.7	135.7	2.0	0.66
12SC03 a04	17.5	0.9	0.038	0.00068	0.082	0.0011	2.1379	0.0574	0.0013	0.000028	38.2	142.7	1.7	0.64
12SC03 a05	21.1	1.3	0.031	0.00091	0.060	0.0013	1.9514	0.0448	0.0013	0.000031	30.6	125.4	1.0	0.57
12SC05: 38.93781°N, 114.26141°W; 2666 m														
12SC05 a01	15.7	0.7	0.064	0.00070	0.105	0.0012	1.6238	0.0891	0.0018	0.000035	41.8	170.1	2.5	0.67
12SC05 a02	15.5	0.9	0.034	0.00034	0.080	0.0009	2.3407	0.0528	0.0011	0.000031	53.6	134.4	3.2	0.71
12SC05 a03	14.7	0.5	0.036	0.00039	0.071	0.0007	1.9767	0.0524	0.0010	0.000016	66.3	124.1	4.5	0.74
12SC07: 38.92962°N, 114.24306°W; 2538 m														
12SC07 a01	13.1	0.7	0.045	0.00052	0.113	0.0014	2.5430	0.0712	0.0012	0.000032	44.8	148.8	2.5	0.68
12SC07 a02	14.3	0.7	0.032	0.00043	0.063	0.0008	1.9385	0.0470	0.0009	0.000021	49.6	136.5	2.8	0.70
12SC07 a03	13.5	0.6	0.037	0.00043	0.087	0.0013	2.3511	0.0574	0.0010	0.000019	32.9	170.5	1.5	0.61

^aAliquots used to calculate weighted mean age in Chapter 2 of text.^bAlpha ejection corrected apatite (U-Th)/He age.^cPropagated analytical error; does not take into account error induced by natural U and Th zoning.^dAnalytical error of measurement.^eEffective U concentration (eU) calculated based on equation $eU = U + 0.235\text{Th}$ from Shuster *et al.* [2006]^fF_T corrected ⁴He concentration.^gAveraged measurements from two faces of analyzed apatite grain.^hF_T correction following method outlined in Hourigan *et al.* [2005]

Appendix 2: Supplemental material for Chapter 3

1. Overview of Contents

This appendix contains Table A2.1 and A2.2, as well as Figure A2.1. Table A2.1 contains all replicate aliquot analyses of reported ApHe dates in Table 3.2. Table A2.2 contains of all well data used to interpolate depth to top and base Paradox salt surfaces and thickness of Paradox salt in the study area (Figures 3.4 and 3.5). The included figure (Figure A2.1) depicts the locations of the wells in the study area. All well data used in this study is publically available at <http://dnrwebmapgdev.state.co.us/mg2012app/>.

Appendix 2 Figure

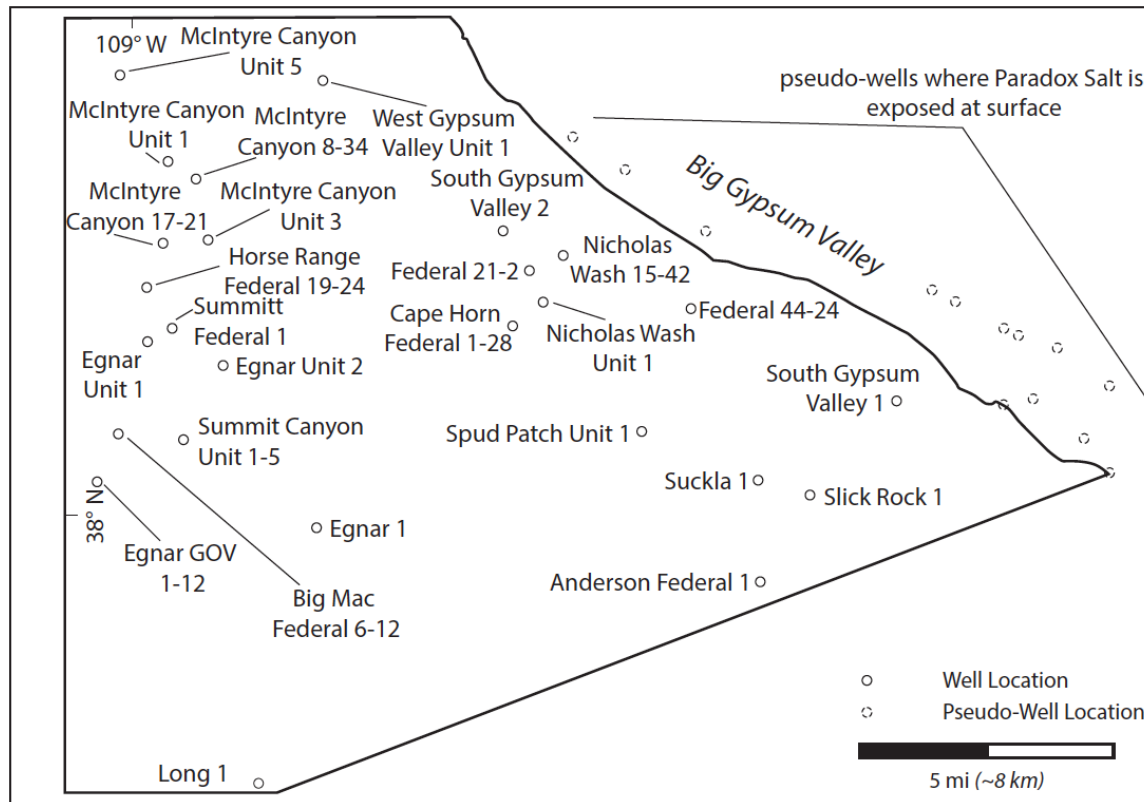


Figure A2.1 Well locations

Figure A2.1: Names and locations of wells used in Chapter 3 to interpolate top, base, and thickness of Paradox salt.

Appendix 2 Tables

Table A2.1 Replicate apatite (U-Th)/He analyses

Aliquot ^a	Age ^b (Ma)	$\pm 2\sigma^c$ (Ma)	U ($\mu\text{mol/g}$)	$\pm 1\sigma^d$ ($\mu\text{mol/g}$)	Th ($\mu\text{mol/g}$)	$\pm 1\sigma^d$ ($\mu\text{mol/g}$)	Th/U	⁴ He ^e ($\mu\text{mol/g}$)	$\pm 1\sigma^c$ ($\mu\text{mol/g}$)	Radius ^f (μm)	Mass (μg)	F _T ^g	eU ^h ($\mu\text{mol/g}$)
<u>14GV02: 37.99435, -108.9907</u>													
14GV02 a001	19.6	1.0	0.03464	0.00040	0.14187	0.00286	4.09536	0.00172	0.000037	32.7	1.0	0.57	0.0680
<i>14GV02 a002</i>	<i>67.5</i>	<i>5.9</i>	<i>0.00835</i>	<i>0.00020</i>	<i>0.02722</i>	<i>0.00214</i>	<i>3.25970</i>	<i>0.00132</i>	<i>0.000034</i>	<i>29.7</i>	<i>1.2</i>	<i>0.57</i>	0.0147
14GV02 a003	18.7	1.3	0.02231	0.00029	0.02476	0.00172	1.11000	0.00068	0.000021	30.7	1.4	0.60	0.0281
14GV02 a004	22.6	1.3	0.03630	0.00052	0.21829	0.00387	6.01352	0.00254	0.000065	31.0	0.7	0.54	0.0876
<u>14GV04: 38.02585, -108.99091</u>													
14GV04 a001	4.8	1.4	0.02274	0.00055	0.32082	0.00678	14.10689	0.00061	0.000088	26.2	0.4	0.45	0.0981
<i>14GV04 a002</i>	<i>10.9</i>	<i>1.2</i>	<i>0.03366</i>	<i>0.00066</i>	<i>0.28523</i>	<i>0.00609</i>	<i>8.47372</i>	<i>0.00142</i>	<i>0.000074</i>	<i>26.6</i>	<i>0.4</i>	<i>0.47</i>	0.1007
14GV04 a003	3.8	2.3	0.00249	0.00032	0.13215	0.00437	53.16348	0.00016	0.000049	29.1	0.6	0.49	0.0335
<u>14GV08: 38.05466, -108.94401</u>													
14GV08 a001	22.0	0.82	0.10192	0.00101	0.08444	0.00083	0.82849	0.00349	0.000058	31.7	1.2	0.60	0.1218
14GV08 a002	12.7	0.54	0.01165	0.00015	0.09965	0.00075	8.55528	0.00059	0.000012	56.3	4.7	0.73	0.0351
14GV08 a003	9.6	0.45	0.01812	0.00022	0.09302	0.00084	5.13348	0.00050	0.000011	45.3	3.4	0.69	0.0400
14GV08 a004	17.0	3.3	0.00573	0.00020	0.02137	0.00179	3.72748	0.00024	0.000021	39.7	1.4	0.62	0.0108
14GV08 a005	17.0	0.79	0.03132	0.00041	0.16883	0.00134	5.38998	0.00154	0.000034	41.9	1.8	0.64	0.0710
<u>14GV12: 38.08225, -108.89203</u>													
<i>14GV12 a001</i>	<i>22.3</i>	<i>1.0</i>	<i>0.04001</i>	<i>0.00046</i>	<i>0.18877</i>	<i>0.00305</i>	<i>4.71791</i>	<i>0.00240</i>	<i>0.000049</i>	<i>35.2</i>	<i>0.9</i>	<i>0.58</i>	0.0844
14GV12 a002	9.1	0.56	0.03268	0.00038	0.20947	0.00279	6.40968	0.00097	0.000028	36.1	1.1	0.59	0.0819
14GV12 a003	6.8	1.0	0.01506	0.00026	0.07944	0.00199	5.27462	0.00029	0.000021	40.3	1.3	0.62	0.0337
14GV12 a004	6.0	2.1	0.00642	0.00022	0.05643	0.00244	8.78906	0.00016	0.000027	35.0	1.0	0.58	0.0197
<i>14GV12 a005</i>	<i>99.8</i>	<i>3.0</i>	<i>0.02938</i>	<i>0.00035</i>	<i>0.17946</i>	<i>0.00194</i>	<i>6.10857</i>	<i>0.00939</i>	<i>0.00012</i>	<i>39.0</i>	<i>1.7</i>	<i>0.63</i>	0.0716
<u>14GV14: 38.05836, -108.90128</u>													
14GV14 a001	6.3	0.77	0.00828	0.00024	0.07921	0.00141	9.56941	0.00023	0.000013	41.5	1.6	0.63	0.0269
14GV14 a002	5.1	1.3	0.01147	0.00037	0.05721	0.00202	4.98676	0.00017	0.000021	32.5	1.0	0.57	0.0249
14GV14 a003	5.4	0.76	0.01188	0.00028	0.06819	0.00145	5.73831	0.00020	0.000013	47.0	1.5	0.63	0.0279
14GV14 a004	5.9	0.18	0.11441	0.00095	0.69572	0.00510	6.08073	0.00212	0.000031	38.7	1.8	0.63	0.2779
<i>14GV14 a005</i>	<i>11.8</i>	<i>0.53</i>	<i>0.02552</i>	<i>0.00031</i>	<i>0.12620</i>	<i>0.00154</i>	<i>4.94562</i>	<i>0.00085</i>	<i>0.000018</i>	<i>44.1</i>	<i>1.9</i>	<i>0.65</i>	0.0552
<u>14GV16: 38.08499, -108.84612</u>													
<i>14GV16 a001</i>	<i>26.0</i>	<i>1.6</i>	<i>0.01695</i>	<i>0.00038</i>	<i>0.10107</i>	<i>0.00281</i>	<i>5.96274</i>	<i>0.00136</i>	<i>0.000032</i>	<i>40.8</i>	<i>1.6</i>	<i>0.63</i>	0.0407
14GV16 a002	5.8	1.4	0.02198	0.00067	0.13651	0.00462	6.21013	0.00041	0.000048	33.6	0.9	0.57	0.0541
<i>14GV16 a003</i>	<i>22.6</i>	<i>4.2</i>	<i>0.01591</i>	<i>0.00071</i>	<i>0.04447</i>	<i>0.00526</i>	<i>2.79565</i>	<i>0.00079</i>	<i>0.000060</i>	<i>31.2</i>	<i>0.8</i>	<i>0.55</i>	0.0264
14GV16 a004	7.1	1.6	0.02235	0.00067	0.11194	0.00437	5.00943	0.00044	0.000047	32.4	1.0	0.57	0.0487
<i>14GV16 a005</i>	<i>56.8</i>	<i>6.2</i>	<i>0.01171</i>	<i>0.00065</i>	<i>0.07218</i>	<i>0.00489</i>	<i>6.16561</i>	<i>0.00209</i>	<i>0.000062</i>	<i>30.6</i>	<i>0.8</i>	<i>0.55</i>	0.0287
<u>14GV18: 38.08375, -108.87289</u>													
14GV18 a001	5.7	1.7	0.00769	0.00068	0.21049	0.00543	27.35818	0.00043	0.000063	28.6	0.8	0.52	0.0572
14GV18 a002	6.6	0.72	0.01565	0.00029	0.11085	0.00198	7.08106	0.00036	0.000019	40.5	2.3	0.65	0.0417
14GV18 a003	8.0	1.3	0.00767	0.00046	0.15879	0.00364	20.70065	0.00048	0.000037	36.2	1.2	0.58	0.0450
14GV18 a004	3.5	1.4	0.00930	0.00076	0.28317	0.00638	30.45081	0.00035	0.000070	32.3	0.7	0.52	0.0758
<i>14GV18 a005</i>	<i>12.4</i>	<i>2.2</i>	<i>0.02667</i>	<i>0.00101</i>	<i>0.18475</i>	<i>0.00755</i>	<i>6.92761</i>	<i>0.00113</i>	<i>0.000094</i>	<i>28.4</i>	<i>0.6</i>	<i>0.50</i>	0.0701

^aAliquots used to calculate weighted mean age in Table 3.1 of text. Bold rows are excluded outliers based on Hampel's identifier, and outliers excluded based on age population distributions are in italics.

^bAlpha ejection corrected zircon (U-Th)/He age.

^cPropagated analytical error; does not take into account error induced by natural U and Th zoning.

^dAnalytical error of measurement.

^eF_T corrected ⁴He concentration.

^fAverage radius from two sides of apatite grain.

^gF_T correction following method outlined in *Hourigan et al.* [2005]

^hEffective U concentration (eU) calculated based on equation $eU = U + 0.235Th$ from *Shuster et al.* [2006]

Table A2.2 Well data from Chapter 3

Well Name	Latitude	Longitude	Well Completion Date	True Vertical Depth to Top Paradox Salt ^a	True Vertical Depth to Base Paradox Salt ^a	Paradox Salt Thickness
	(°)	(°)		(ft)	(ft)	(ft)
Egnar 1	37.99512	-108.938287	11/20/55	5421	9567	4146
South Gypsum Valley 2	38.07874	-108.868486	6/3/60	6027	7886	1859
Summit Canyon Unit 1-5	38.02104	-108.985529	12/4/76	5437	9145	3708
Egnar GOV 1-12	38.00957	-109.01696	12/23/68	6121	9607	3486
Egnar Unit 1	38.04926	-108.99761	11/16/60	5527	9040	3513
Summitt Federal 1	38.053	-108.988639	5/16/79	5572	9122	3550
Horse Range Federal 19-24	38.06467	-108.99751	5/4/03	5150	8610	3460
Federal 21-2	38.06728	-108.859266	6/15/81	6844	7807	963
Nicholas Wash 15-42	38.07136	-108.847015	10/14/01	5253	8184	2931
West Gypsum Valley Unit 1	38.12279	-108.932248	10/24/60	8994	10100	1106
McIntyre Canyon Unit 3	38.078	-108.974939	8/17/60	6426	8828	2402
McIntyre Canyon 17-21	38.07722	-108.99138	6/19/01	5402	8541	3139
McIntyre Canyon 8-34	38.09555	-108.978929	4/7/03	7351	8400	1049
McIntyre Canyon Unit 1	38.10069	-108.98875	4/14/60	7955	8751	796
McIntyre Canyon Unit 5	38.1256	-109.00542	2/26/62	9359	9737	378
Egnar Unit 2	38.04205	-108.970549	3/17/61	5386	9208	3822
Big Mac Federal 6-12	38.02314	-109.008869	10/10/02	6088	9439	3351
Cape Horn Federal 1-28	38.05146	-108.865786	1/31/79	7950	8815	865
Anderson Federal 1	37.97689	-108.778942	6/14/73	7762	8692	930
Spud Patch Unit 1	38.02054	-108.820284	9/17/75	8463	8501	37.98
Federal 44-24	38.05528	-108.801434	4/30/91	5202	8193	2991
Nicholas Wash Unit 1	38.0582	-108.854685	5/19/77	7329	8173	844
Suckla 1	38.00583	-108.778683	7/23/74	8474	8626	152
Slick Rock 1	38.00126	-108.760192	8/31/71	8661	8744	83
South Gypsum Valley 1	38.02754	-108.728041	3/9/59	6033	9781	3748
Long 1	37.92257	-108.961047	6/23/69	6127	No Data	-

^aDepth is relative to ground level.

Appendix 3: Plate of preliminary geologic map of the Red Ledges 7.5' quadrangle

The plate (A3.1) associated with Chapter 4 is located in attached supplementary material labeled “Plate A3.1-Preliminary geologic map of the Red Ledges 7.5' quadrangle, White Pine and Lincoln Counties, Nevada.”

Appendix 4: $^{40}\text{Ar}/^{39}\text{Ar}$ data from Chapter 4

1. Overview of Contents

Five rock samples (12SR03, 12SR08, 12SR09, 14SR01, 14SR02) were collected from volcanic units in the Red Ledges quadrangle and were dated at the Nevada Isotope Geochronology Laboratory (NIGL) at the University of Nevada, Las Vegas. The locations and preferred ages of these samples are presented in Table 4.1 of the main text of Chapter 4. Plots of either the ^{39}Ar release plateau spectrum from furnace step heated analyses or cumulative probability of single crystal fusions for each sample are shown in Figures A4.1 to A4.5. Data used to calculate the ages reported in Table 4.1 are available in the Tables A4.1 to A4.5. Analytical procedures followed for these analyses are outlined below.

2. Analytical Procedures

Samples were collected in the field using standard techniques, and were selected to avoid alteration due to weathering processes. Each sample was crushed and sieved at the University of Nevada, Las Vegas, and individual crystals, free of matrix and relatively free of inclusions, were selected using a binocular microscope. Sanidine samples (12SR03, 14SR01) and a single plagioclase sample (14SR02) were single crystal fusion analyses. Amphibole (12SR08) and plagioclase (12SR09) samples were multi-crystal (bulk) fractions, and step heated in a furnace. *Spell et al.* [2001] outlines the standard analytical procedures used at NIGL that are applicable to these samples.

Appendix 4 Figures

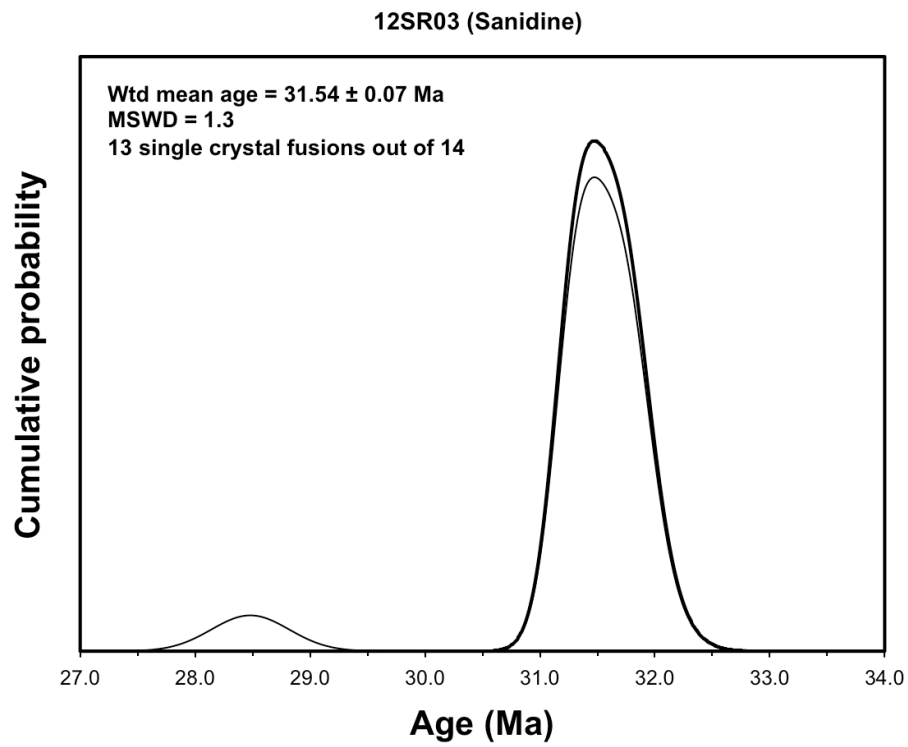


Figure A4.1 12SR03 (sanidine)

Figure A4.1: Cumulative probability plot of sanidine single crystal fusion ages for sample 12SR03. The black line indicates all the cumulative probability plot of all single crystal fusion ages, and the bold black line indicates the 13 analyses used to calculate the weighted mean age.

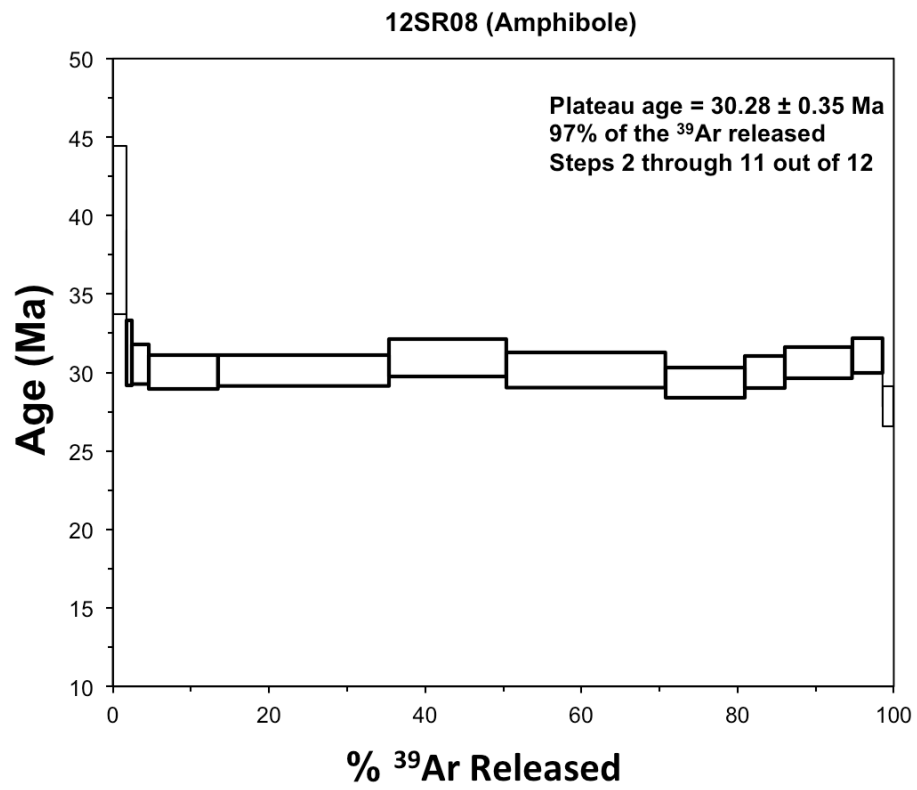


Figure A4.2 12SR08 (amphibole)

Figure A4.2: ^{39}Ar release spectrum from furnace step heating of a bulk amphibole fraction (22.18 mg) from sample 12SR08. Bold lines indicate the steps used to define the plateau age.

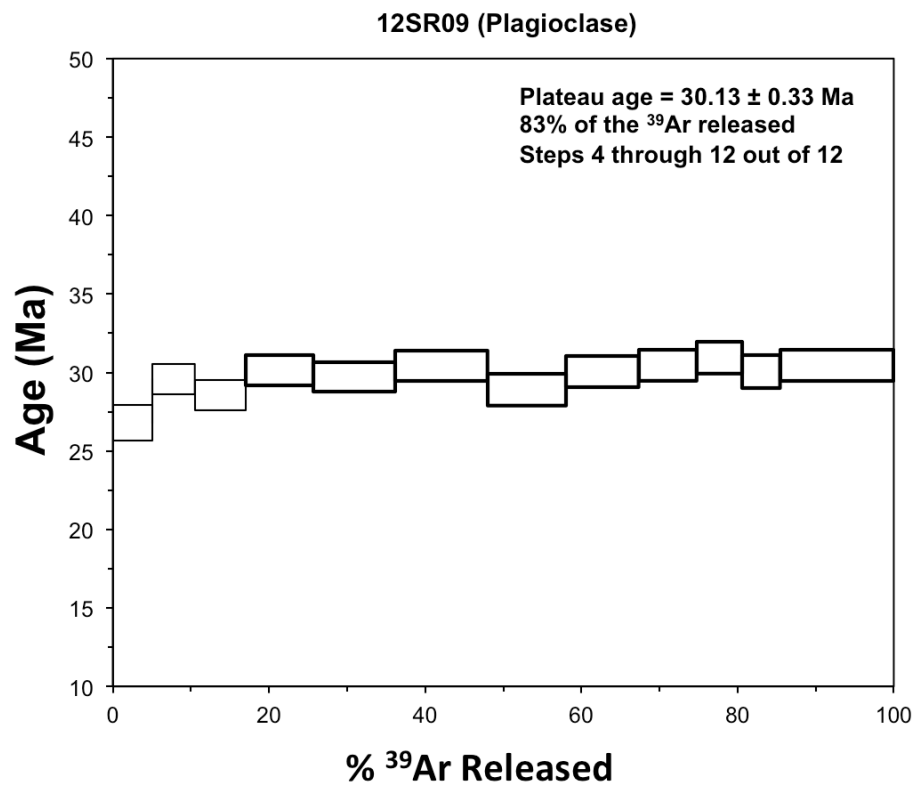


Figure A4.3 12SR09 (plagioclase)

Figure A4.3: ^{39}Ar release spectrum from furnace step heating of a bulk plagioclase fraction (17.90 mg) from sample 12SR09. Bold lines indicate the steps used to define the plateau age.

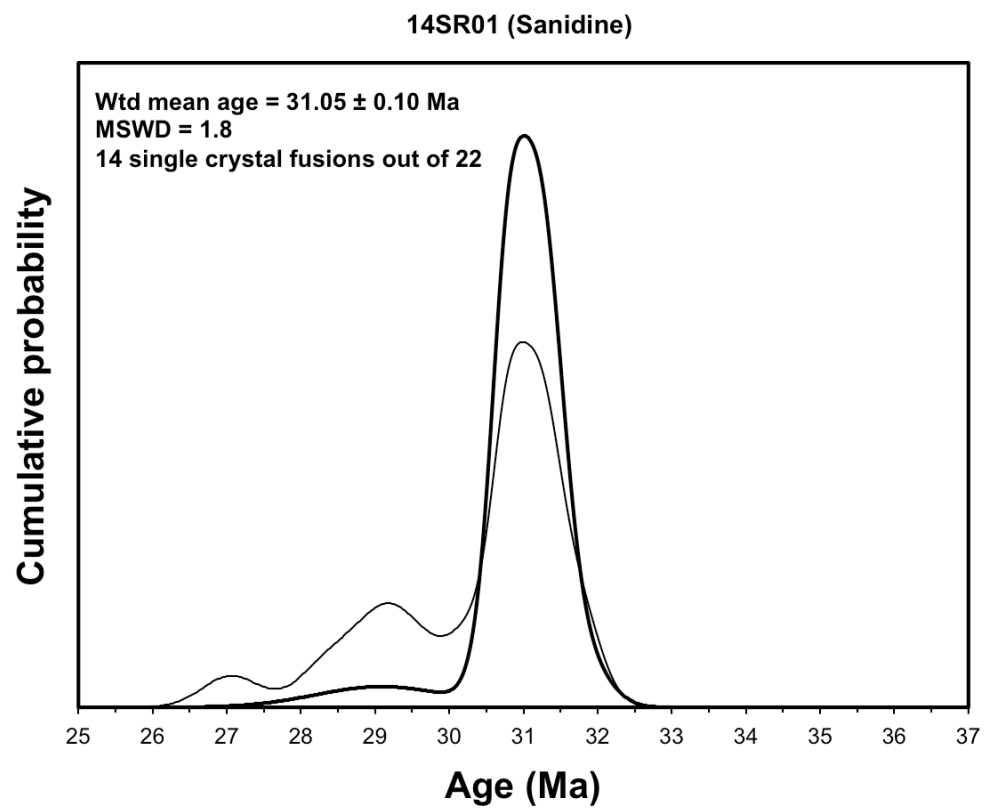


Figure A4.4 14SR01 (sanidine)

Figure A4.4: Cumulative probability plot of sanidine single crystal fusion ages for sample 14SR01. The black line indicates all the cumulative probability plot of all single crystal fusion ages, and the bold black line indicates the 14 analyses used to calculate the weighted mean age.

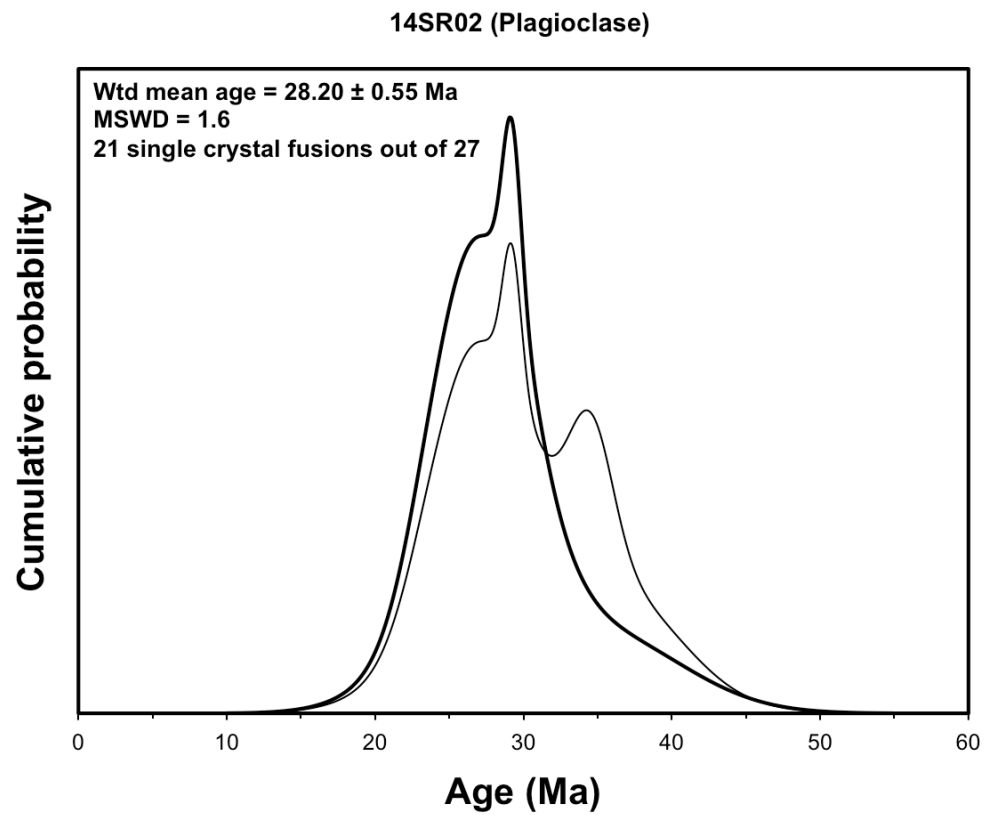


Figure A4.5 14SR02 (plagioclase)

Figure A4.5: Cumulative probability plot of plagioclase single crystal fusion ages for sample 14SR02. The black line indicates all the cumulative probability plot of all single crystal fusion ages, and the bold black line indicates the 21 analyses used to calculate the weighted mean age.

Appendix 4 Tables

Table A4.1 12SR03, sanidine, single crystal fusion^a

Crystal	T (°C)	t (min.)	³⁶ Ar	³⁷ Ar	³⁸ Ar	³⁹ Ar	⁴⁰ Ar	% ⁴⁰ Ar*	Ca/K	⁴⁰ Ar*/ ³⁹ ArK	Age (Ma)	1s.d.
1	1600	2	0.091	0.325	1.522	114.927	1174.80	98.3	0.01861	10.14466	31.84	0.20
2	1600	2	0.048	0.208	0.890	67.579	685.596	99.0	0.02025	10.09548	31.68	0.20
3	1600	2	0.067	0.199	0.891	67.663	688.224	98.2	0.01935	10.04309	31.52	0.19
4	1600	2	0.203	0.150	0.639	46.218	512.660	90.1	0.02135	10.02348	31.46	0.21
5	1600	2	0.088	0.405	1.234	94.233	949.269	98.0	0.02828	9.95599	31.25	0.19
6	1600	2	0.166	0.306	1.143	83.795	879.887	95.4	0.02403	10.09452	31.68	0.20
7	1600	2	0.066	0.504	0.730	56.042	580.592	97.9	0.05917	10.18549	31.96	0.26
8	1600	2	0.052	0.217	0.870	65.941	663.136	98.8	0.02165	9.98395	31.34	0.18
9	1600	2	0.047	0.182	0.737	55.546	558.440	98.8	0.02156	9.96756	31.29	0.19
10	1600	2	0.062	0.234	0.825	63.332	582.940	98.1	0.02431	9.06651	28.48	0.34
11	1600	2	0.072	0.151	0.568	42.818	447.635	96.9	0.02320	10.14338	31.83	0.21
12	1600	2	0.045	0.214	1.006	76.199	764.148	99.2	0.01848	10.00902	31.42	0.24
13	1600	2	0.072	0.179	0.880	66.039	669.231	97.9	0.01783	9.97720	31.32	0.19
14	1600	2	0.054	0.214	0.938	71.873	729.958	98.8	0.01959	10.09419	31.68	0.21
Mean ± s.d. =											31.34	0.82
Wtd mean age =											31.54	0.07
(13 fusions)												
Isochron age =											31.48	0.11
(12 fusions)												

^aJ = 0.001755 ± 0.009%, 4 amu discrimination = 1.0622 ± 0.46%, ⁴⁰/³⁹K = 0.0104 ± 19.23%, ³⁶/³⁷Ca = 0.000264 ± 4.93%, ³⁹/³⁷Ca = 0.0006595 ± 6.11%

note: isotope beams in mV rlsd = released, error in age includes J error, all errors 1 sigma
(³⁶Ar through ⁴⁰Ar are measured beam intensities, corrected for decay in age calculations)

Table A4.2 12SR08, amphibole, 22.18 mg^a

step	T (°C)	t (min.)	³⁶ Ar	³⁷ Ar	³⁸ Ar	³⁹ Ar	⁴⁰ Ar	% ⁴⁰ Ar ⁺	% ³⁹ Ar rlsd	Ca/K	⁴⁰ Ar ⁺ / ³⁹ ArK	Age (Ma)	Is.d.
1	850	12	1.271	3.068	0.468	5.966	431.948	17.6	1.7	3.139321	12.465759	39.07	2.68
2	950	12	0.099	1.470	0.238	2.471	51.115	66.1	0.7	3.632198	9.945827	31.24	1.03
3	1050	12	0.156	11.502	1.299	7.393	111.771	72.8	2.1	9.514999	9.717839	30.53	0.63
4	1090	12	0.309	67.596	6.058	30.515	360.072	83.1	8.9	13.56333	9.554770	30.02	0.54
5	1110	12	0.481	171.353	14.727	75.705	815.583	89.2	22.0	13.85998	9.587509	30.12	0.49
6	1120	12	0.867	117.953	10.546	51.615	722.709	71.0	15.0	13.9941	9.842098	30.91	0.60
7	1130	12	0.434	162.789	14.374	70.254	754.730	90.1	20.4	14.19026	9.601632	30.16	0.57
8	1140	12	0.236	81.172	7.083	35.139	374.008	90.6	10.2	14.14646	9.336881	29.34	0.47
9	1160	12	0.170	42.065	4.067	17.597	206.109	87.9	5.1	14.64113	9.555091	30.02	0.51
10	1210	12	0.235	73.542	7.405	29.678	336.734	89.1	8.6	15.17958	9.743523	30.61	0.50
11	1270	12	0.141	32.737	3.063	13.478	164.883	88.8	3.9	14.87767	9.887698	31.06	0.55
12	1400	12	0.150	12.372	1.161	4.966	83.167	69.8	1.4	15.26168	8.853583	27.83	0.63
Cumulative % ³⁹ Ar rlsd =										Total gas age =			
										Plateau age =			
										(steps 2-11)			
										Isochron age =			
										(steps 1-11)			

^aJ = 0.001756 ± 0.007%, 4 amu discrimination = 1.0483 ± 1.20%, ⁴⁰β³⁹K = 0.0104 ± 19.23%, ³⁶/β³⁷Ca = 0.000264 ± 4.93%, ³⁹/β³⁷Ca = 0.0006595 ± 6.11%

note: isotope beams in mV, rlsd = released, error in age includes J error, all errors 1 sigma

(³⁶Ar through ⁴⁰Ar are measured beam intensities, corrected for decay for the age calculations)

Table A4.3 12SR09, plagioclase, 17.90 mg^a

step	T (°C)	t (min.)	³⁶ Ar	³⁷ Ar	³⁸ Ar	³⁹ Ar	⁴⁰ Ar	% ⁴⁰ Ar*	% ³⁹ Ar rlsd	Ca/K	⁴⁰ Ar*/ ³⁹ ArK	Age (Ma)	Is.d.
1	650	12	0.181	4.033	0.124	7.429	114.124	62.6	5.1	3.203699	8.567476	26.79	0.57
2	730	12	0.081	8.223	0.122	7.962	96.617	89.6	5.4	6.099892	9.464900	29.57	0.49
3	810	12	0.100	20.013	0.159	9.654	112.240	88.2	6.6	12.26548	9.141629	28.57	0.49
4	890	12	0.099	34.601	0.193	12.702	142.757	93.4	8.7	16.13527	9.646616	30.13	0.49
5	960	12	0.112	45.142	0.233	15.319	165.368	95.0	10.4	17.46122	9.509436	29.71	0.48
6	1020	12	0.131	50.485	0.274	17.357	192.694	93.3	11.8	17.2339	9.739272	30.42	0.49
7	1070	12	0.113	45.738	0.241	14.797	156.881	94.6	10.1	18.32036	9.253560	28.92	0.51
8	1120	12	0.117	41.092	0.222	13.614	154.306	94.0	9.3	17.88745	9.615627	30.04	0.50
9	1170	12	0.111	32.962	0.191	10.905	129.957	92.7	7.4	17.91298	9.747989	30.45	0.49
10	1220	12	0.113	25.581	0.169	8.573	110.933	89.1	5.8	17.68219	9.910094	30.95	0.51
11	1270	12	0.121	20.916	0.147	7.115	97.918	83.2	4.8	17.41897	9.622406	30.06	0.53
12	1400	12	0.202	59.422	0.460	21.394	250.844	89.4	14.6	16.45335	9.752832	30.46	0.50
Cumulative % ³⁹ Ar rlsd =										Total gas age =			
										Plateau age =			
										(steps 4-12)			
										30.13			
										Isochron age =			
										28.60			
										(steps 4-10)			
										0.33			

^aJ = 0.001746 ± 0.008%, 4 amu discrimination = 1.0483 ± 1.20%, ⁴⁰39K = 0.0104 ± 19.23%, ³⁶37Ca = 0.000264 ± 4.93%, ³⁹37Ca = 0.0006595 ± 6.11%

note: isotope beams in mV, rlsd = released, error in age includes J error, all errors 1 sigma
(³⁶Ar through ⁴⁰Ar are measured beam intensities, corrected for decay for the age calculations)

Table A4.4 14SR01, single crystal sanidine^a

Crystal	T (°C)	t (min.)	³⁶ Ar	³⁷ Ar	³⁸ Ar	³⁹ Ar	⁴⁰ Ar	% ⁴⁰ Ar [±]	Ca/K	⁴⁰ Ar/ ³⁹ ArK	Age (Ma)	Is.d.
1	1600	2	0.059	0.126	0.571	42.149	426.081	97.3	0.017537	9.9122	31.27	0.20
2	1600	2	0.143	0.136	0.327	22.630	257.041	86.3	0.035256	9.8381	31.04	0.25
3	1600	2	0.036	0.029	0.093	6.754	73.698	92.9	0.025189	9.9132	31.28	0.29
4	1600	2	0.087	0.142	0.163	10.616	127.481	84.6	0.078471	10.0881	31.82	0.24
5	1600	2	0.059	0.079	0.179	13.127	143.297	91.9	0.035305	9.9823	31.49	0.21
6	1600	2	0.026	0.050	0.167	12.199	116.405	97.3	0.024045	9.1968	29.03	0.31
7	1600	2	0.037	0.051	0.166	12.528	131.100	95.2	0.023882	9.8972	31.23	0.29
8	1600	2	0.071	0.064	0.232	16.887	180.793	91.2	0.022233	9.7572	30.79	0.23
9	1600	2	0.037	0.036	0.077	5.450	58.350	89.0	0.038751	9.2134	29.09	0.89
10	1600	2	0.056	0.894	0.286	19.828	205.751	94.4	0.264525	9.8071	30.94	0.23
11	1600	2	0.034	0.024	0.115	7.713	80.278	95.9	0.043567	9.4673	29.88	0.36
12	1600	2	0.031	0.022	0.121	8.128	84.376	97.1	0.037898	9.5987	30.29	0.27
13	1600	2	0.054	0.025	0.107	7.606	83.778	88.8	0.046021	9.3111	29.39	0.31
14	1600	2	0.052	0.033	0.225	16.073	168.196	95.0	0.028747	9.7434	30.74	0.19
15	1600	2	0.078	0.037	0.213	13.873	153.857	89.5	0.037343	9.7086	30.64	0.24
16	1600	2	0.031	0.025	0.128	9.094	88.113	97.3	0.038491	8.9925	28.39	0.38
17	1600	2	0.062	0.016	0.066	3.383	44.603	72.1	0.066221	8.5639	27.05	0.39
18	1600	2	0.032	0.016	0.116	8.126	86.672	96.9	0.027569	9.8512	31.08	0.29
19	1600	2	0.037	0.017	0.129	8.561	92.144	95.4	0.027803	9.8285	31.01	0.39
20	1600	2	0.035	0.017	0.101	7.515	83.139	95.6	0.031673	10.0641	31.75	0.34
21	1600	2	0.037	0.011	0.079	5.990	67.186	93.6	0.025712	9.8416	31.05	0.30
22	1600	2	0.057	0.030	0.083	5.411	63.520	83.5	0.077628	9.1505	28.89	0.52
										Mean ± s.d. =	30.37	1.20
										Wtd mean age =	31.05	0.10
										(14 fusions)		
										Isochron age =	30.44	0.24

^aJ = 0.001764 ± 0.16%, 4 amu discrimination (1-10) = 1.0596 ± 0.45%, 4 amu discrimination (11-22) = 1.0414 ± 0.40%, ⁴⁰/β³⁹K =0.0002 ± 150.00%, ³⁶β³⁷Ca = 0.000228 ± 10.28%, ³⁹β³⁷Ca = 0.000792 ± 11.04%note: isotope beams in mV rlsd = released, error in age includes J error, all errors 1 sigma
(³⁶Ar through ⁴⁰Ar are measured beam intensities, corrected for decay in age calculations)

Table A4.5 14SR02, single crystal plagioclase^a

Crystal	T (°C)	t (min.)	³⁶ Ar	³⁷ Ar	³⁸ Ar	³⁹ Ar	⁴⁰ Ar	% ⁴⁰ Ar*	Ca/K	⁴⁰ Ar*/ ³⁹ ArK	Age (Ma)	1s.d.
1	1600	2	0.029	0.942	0.016	0.606	11.289	80.4	22.22625	9.4876	29.79	1.99
2	1600	2	0.033	0.801	0.010	0.578	11.232	63.2	19.80093	7.7537	24.38	1.96
3	1600	2	0.028	0.851	0.015	0.743	12.175	85.9	16.34873	9.2738	29.13	1.55
4	1600	2	0.032	0.744	0.010	0.619	12.070	70.6	17.16044	9.0768	28.51	1.83
5	1600	2	0.030	0.490	0.012	0.389	9.349	63.7	17.98861	8.4899	26.68	2.86
6	1600	2	0.029	0.776	0.011	0.484	9.454	72.0	22.92943	7.8226	24.60	4.45
7	1600	2	0.033	0.841	0.023	0.633	11.653	65.5	18.97881	7.7819	24.47	1.99
8	1600	2	0.028	0.804	0.021	0.635	12.136	85.6	18.08195	10.8098	33.91	1.83
9	1600	2	0.036	1.542	0.031	1.100	16.547	74.7	20.03095	8.4966	26.70	1.42
10	1600	2	0.025	0.754	0.015	0.572	11.651	95.9	18.82925	12.6365	39.57	2.86
11	1600	2	0.039	0.028	0.109	6.791	70.879	93.4	0.058573	9.3024	29.22	0.62
12	1600	2	0.027	1.088	0.017	0.741	12.936	91.4	20.98658	10.8929	34.16	1.62
13	1600	2	0.027	0.950	0.018	0.678	12.606	87.3	20.02178	11.0896	34.77	1.35
14	1600	2	0.029	0.532	0.017	0.361	8.666	59.2	21.06421	7.5249	23.67	2.21
15	1600	2	0.035	0.574	0.013	0.451	11.889	55.0	18.1765	9.7166	30.51	3.24
16	1600	2	0.027	0.677	0.021	0.398	9.644	78.3	24.33663	11.0474	34.64	2.68
17	1600	2	0.028	0.783	0.016	0.524	10.725	73.9	21.36037	9.4392	29.64	2.98
18	1600	2	0.029	0.630	0.013	0.384	8.779	61.1	23.46682	7.4698	23.50	3.63
19	1600	2	0.029	0.837	0.014	0.570	10.459	73.0	20.98852	8.1960	25.77	1.69
20	1600	2	0.025	0.449	0.003	0.310	8.296	82.8	20.70043	11.2876	35.39	4.24
21	1600	2	0.026	0.371	0.015	0.300	8.020	73.2	17.65884	9.5849	30.10	2.68
22	1600	2	0.030	0.418	0.008	0.312	9.761	61.7	19.13897	11.4735	35.97	2.66
23	1600	2	0.028	0.395	0.013	0.307	8.281	61.0	18.37634	8.3642	26.29	2.81
24	1600	2	0.027	0.377	0.012	0.342	9.562	75.9	15.73187	12.3296	38.62	4.88
25	1600	2	0.023	0.482	0.006	0.343	7.795	96.9	20.08025	10.3360	32.43	6.58
26	1600	2	0.029	0.540	0.015	0.362	9.212	63.9	21.32352	9.1329	28.69	3.41
27	1600	2	0.025	0.412	0.004	0.257	7.687	79.3	22.92665	11.1385	34.93	5.26
Mean ± s.d. =											30.22	4.59
Wtd mean age =											28.20	0.55
(21 fusions)												
No isochron												

^aJ = 0.001755 ± 0.17%, 4 amu discrimination = 1.0733 ± 1.47%, ⁴⁰/³⁹K = 0.0002 ± 150.00%, ³⁶/³⁷Ca = 0.000228 ± 10.28%, ³⁹/³⁷Ca = 0.000792 ± 11.04%

note: isotope beams in mV rlsd = released, error in age includes J error, all errors 1 sigma
(³⁶Ar through ⁴⁰Ar are measured beam intensities, corrected for decay in age calculations)

References

- Allmendinger, R. W., J. W. Sharp, D. Von Tish, L. Serpa, L. Brown, S. Kaufman, J. Oliver, and R. B. Smith (1983), Cenozoic and Mesozoic structure of the eastern Basin and Range province, Utah, from COCORP seismic-reflection data, *Geology*, *11*(9), 532-536, doi: 10.1130/0091-7613(1983)11<532:CAMSOT>2.0.CO;2.
- Armstrong, R. L. (1972), Low-angle (denudation) faults, hinterland of the Sevier orogenic belt, eastern Nevada and western Utah, *Geol. Soc. Am. Bull.*, *83*(6), 1729-1754, doi: 10.1130/0016-7606(1972)83[1729:LDFHOT]2.0.CO;2.
- Axen, G. J., W. J. Taylor, and J. M. Bartley (1993), Space-time patterns and tectonic controls of Tertiary extension and magmatism in the Great Basin of the western United States, *Geol. Soc. Am. Bull.*, *105*(1), 56-76, doi: 10.1130/00167606(1993)105<0056:STPATC>2.3.CO;2.
- Baars, D. and G. Stevenson (1981), Tectonic evolution of the Paradox basin, Utah and Colorado, *Rocky Mountain Association of Geologists 1981 Field Conference*, 23-31.
- Barbeau, D. (2003), A flexural model for the Paradox Basin: Implications for the tectonics of the Ancestral Rocky Mountains, *Basin Res.*, *15*(1), 97-115, doi:10.1046/j.1365-2117.2003.00194.x.
- Bartley, J. M. and B. P. Wernicke (1984), The Snake Range décollement interpreted as a major extensional shear zone, *Tectonics*, *3*(6), 647-657, doi:10.1029/TC003i006p00647.
- Beardsmore, G. R. and J. P. Cull (2001), *Crustal Heat Flow: A Guide to Measurement and Modelling*, Cambridge, Cambridge University Press, 324 p.
- Best, M. G. and E. H. Christiansen (1991), Limited extension during peak Tertiary volcanism, Great Basin of Nevada and Utah, *J. Geophys. Res.: Sol. Ea. (1978-2012)*, *96*(B8), 13509

13528, doi:10.1029/91JB00244.

- Best, M. G., E. H. Christiansen, A. L. Deino, C. Gromme, E. H. McKee, and D. C. Noble (1989), Eocene through Miocene volcanism in the Great Basin of the western United States, *New Mexico Bureau of Mines and Mineral Resources Memoir*, 47, 91-133.
- Best, M. G., E. H. Christiansen, A. L. Deino, S. Gromme, G. L. Hart, and D. G. Tingey (2013a), The 36–18 Ma Indian Peak–Caliente ignimbrite field and calderas, southeastern Great Basin, USA: Multicyclic super-eruptions, *Geosphere*, 9(4), 864-950, doi:10.1130/GES00902.1.
- Best, M. G., E. H. Christiansen, and S. Gromme (2013b), Introduction: The 36–18 Ma southern Great Basin, USA, ignimbrite province and flareup: Swarms of subduction-related supervolcanoes, *Geosphere*, 9(2), 260-274, doi: 10.1130/GES00870.1.
- Best, M. G. and S. K. Grant (1987), Stratigraphy of the volcanic Oligocene Needles Range Group in southwestern Utah and eastern Nevada, *U.S. Geol. Surv. Prof. Pap.* 1433A, 3-28.
- Blackwell, D. D. and J. L. Steele (1989), Thermal conductivity of sedimentary rocks: Measurement and significance, *Thermal History of Sedimentary Basins Methods and Case Histories*, edited by N. D. Naeser and T.H. McCulloh, 13-36, Springer Verlag, New York, doi 10.1007/978-1-4612-3492-0_2.
- Bodell, J. M. and D. S. Chapman (1982), Heat flow in the north-central Colorado Plateau, *J. Geophys. Res.-Sol. Ea.*, 87(B4), 2869-2884, doi:10.1029/JB087iB04p02869.
- Braun, J. (2003), Pecube: A new finite-element code to solve the 3D heat transport equation including the effects of a time-varying, finite amplitude surface topography, *Comput. Geosci.*, 29(6), 787-794, doi:10.1016/S0098-3004(03)00052-9.

- Braun, J., P. Van Der Beek, P. Valla, X. Robert, F. Herman, C. Glotzbach, V. Pedersen, C. Perry, T. Simon-Labric, and C. Prigent (2012), Quantifying rates of landscape evolution and tectonic processes by thermochronology and numerical modeling of crustal heat transport using PECUBE, *Tectonophysics*, 524-525, 1-28, doi:10.1016/j.tecto.2011.12.035.
- Buck, W. R. (1991), Modes of continental lithospheric extension, *J. Geophys. Res.: Sol. Ea.* (1978–2012), 96(B12), 20161-20178, doi:10.1029/91JB01485.
- Byerly, P. E. and H. R. Joesting (1959), Regional geophysical investigations of the Lisbon Valley area Utah and Colorado, *U.S. Geol. Surv. Prof. Pap.*, 316-C, 1-50.
- Case, J. E. and H. R. Joesting (1972), Regional geophysical investigations in the central Colorado Plateau, *U.S. Geol. Surv. Prof. Pap.*, 736, 1-36.
- Cater, F. W. and L. C. Craig (1970), Geology of the salt anticline region in southwestern Colorado, with a section on stratigraphy, *U.S. Geol. Surv. Prof. Pap.*, 637, 1-79.
- Cather, S. M., C. E. Chapin, and S. A. Kelley (2012), Diachronous episodes of Cenozoic erosion in southwestern North America and their relationship to surface uplift, paleoclimate, paleodrainage, and paleoaltimetry, *Geosphere*, 8(6), 1177-1206, doi: 10.1130/GES00801.1.
- Chan, M. A., W. Parry, and J. Bowman (2000), Diagenetic hematite and manganese oxides and fault-related fluid flow in Jurassic sandstones, southeastern Utah, *AAPG Bull.*, 84(9), 1281-1310.
- Childs, C. (2004), Interpolating surfaces in ArcGIS spatial analyst, *ArcUser*, July-September, 32-35.
- Colgan, J. P., T. A. Dumitru, P. W. Reiners, J. L. Wooden, and E. L. Miller (2006), Cenozoic tectonic evolution of the Basin and Range Province in northwestern Nevada, *Am. J. Sci.*,

- 306(8), 616-654, doi: 10.2475/08.2006.02.
- Colgan, J. P. and C. D. Henry (2009), Rapid middle Miocene collapse of the Mesozoic orogenic plateau in north-central Nevada, *Int. Geol. Rev.*, 51(9-11), 920-961, doi:10.1080/00206810903056731.
- Colgan, J. P., K. A. Howard, R. J. Fleck, and J. L. Wooden (2010), Rapid middle Miocene extension and unroofing of the southern Ruby Mountains, Nevada, *Tectonics*, 29(6), TC6022, doi:10.1029/2009TC002655.
- Compton, R. R. (1985), *Geology in the Field*, John Wiley and Sons, New York, New York, United States of America, 398 p.
- Coney, P. J. and T. A. Harms (1984), Cordilleran metamorphic core complexes: Cenozoic extensional relics of Mesozoic compression, *Geology*, 12(9), 550-554, doi:10.1130/0091-7613(1984)12<550:CMCCCE>2.0.CO;2.
- Cooper, F., J. Platt, R. Anczkiewicz, and M. Whitehouse (2010), Footwall dip of a core complex detachment fault: Thermobarometric constraints from the northern Snake Range (Basin and Range, USA), *J. Metamorph. Geol.*, 28(9), 997-1020, doi:10.1111/j.1525-1314.2010.00907.x.
- Dahlstrom, C. (1969), Balanced cross sections, *Can. J. Earth Sci.*, 6(4), 743-757, doi: 10.1139/e69-069.
- Dallmeyer, R., A. Snoke, and E. McKee (1986), The Mesozoic-Cenozoic tectonothermal evolution of the Ruby Mountains, East Humboldt Range, Nevada: A Cordilleran metamorphic core complex, *Tectonics*, 5(6), 931-954, doi:10.1029/TC005i006p00931.
- DeCelles, P. G. (2004), Late Jurassic to Eocene evolution of the Cordilleran thrust belt and foreland basin system, western USA, *Am. J. Sci.*, 304(2), 105-168, doi:10.2475/

ajs.304.2.105.

- DeCelles, P. G. and J. C. Coogan (2006), Regional structure and kinematic history of the Sevier fold-and-thrust belt, central Utah, *Geol. Soc. Am. Bull.*, 118(7-8), 841-864, doi: 10.1130/B25759.1.
- DePolo, C. (2008), Quaternary Faults of Nevada, *Nevada Bureau of Mines and Geology Map M167*, 1:1,000,000 scale, 1 p.
- Dickinson, W. R. (2006), Geotectonic evolution of the Great Basin, *Geosphere*, 2(7), 353-368, doi: 10.1130/GES00054.1.
- Dickinson, W. R., M. A. Klute, M. J. Hayes, S. U. Janecke, E. R. Lundin, M. A. McKittrick, and M. D. Olivares (1988), Paleogeographic and paleotectonic setting of Laramide sedimentary basins in the central Rocky Mountain region, *Geol. Soc. Am. Bull.*, 100(7), 1023-1039, doi: 10.1130/0016-7606(1988)100<1023:PAPSOL>2.3.CO;2.
- Dodson, M. (1979), Theory of cooling ages, in *Lectures in Isotope Geology*, edited by E. Jager and J.C. Hunziker, pp. 194-202, Springer-Verlag.
- Dohrenwend, J. C., B. A. Schell, C. M. Menges, B. C. Moring, and M. A. McKittrick (1996), Reconnaissance photogeologic map of young (Quaternary and late Tertiary) faults in Nevada, *Nevada Bureau of Mines and Geology Open-File Report*, 96-2, 9-1-9-12.
- Dow, W. G. (1977), Kerogen studies and geological interpretations, *J. Geochem. Explor.*, 7, 79-99, doi:10.1016/0375-6742(77)90078-4.
- Drewes, H. (1958), Structural geology of the southern Snake Range, Nevada, *Geol. Soc. Am. Bull.*, 69(2), 221-240, doi: 10.1130/0016-7606(1958)69[221:SGOTSS]2.0.CO;2.
- Druschke, P., A. D. Hanson, M. L. Wells, T. Rasbury, D. F. Stockli, and G. Gehrels (2009), Synconvergent surface-breaking normal faults of Late Cretaceous age within the Sevier

- hinterland, east-central Nevada, *Geology*, 37(5), 447-450, doi:10.1130/G25546A.1.
- Ehlers, T. A. and K. A. Farley (2003), Apatite (U–Th)/He thermochronometry: Methods and applications to problems in tectonic and surface processes, *Earth Planet. Sci. Lett.*, 206(1), 1-14, doi:10.1016/S0012-821X(02)01069-5.
- Evans, D. G. and J. A. Nunn (1989), Free thermohaline convection in sediments surrounding a salt column, *J. Geophys. Res.-Sol. Ea.*, 94(B9), 12413-12422, doi:10.1029/JB094iB09p12413.
- Evans, S. L., R. H. Styron, M. C. Soest, K. V. Hodges, and A. D. Hanson (2015), Zircon and apatite (U-Th)/He evidence for Paleogene and Neogene extension in the Southern Snake Range, Nevada, USA, *Tectonics*, 34(10), 2142-2164, doi:10.1002/2015TC003913.
- Farley, K. (2000), Helium diffusion from apatite: General behavior as illustrated by Durango fluorapatite, *J. Geophys. Res.: Sol. Ea. (1978–2012)*, 105(B2), 2903-2914, doi:10.1029/1999JB900348.
- Farley, K., R. Wolf, and L. Silver (1996), The effects of long alpha-stopping distances on (U-Th)/He ages, *Geochim. Cosmochim. Acta*, 60(21), 4223-4229, doi:10.1016/S0016-7037(96)00193-7.
- Farley, K. A. (2002), (U-Th)/He dating: Techniques, calibrations, and applications, *Rev. Mineral. Geochem.*, 47(1), 819-844, doi: 10.2138/rmg.2002.47.18.
- Farr, T. G., P. A. Rosen, E. Caro, R. Crippen, R. Duren, S. Hensley, M. Kobrick, M. Paller, E. Rodriguez, and L. Roth (2007), The shuttle radar topography mission, *Rev. Geophys.*, 45(2), RG2004, doi:10.1029/2005RG000183.
- Flowers, R. M., R. A. Ketcham, D. L. Shuster, and K. A. Farley (2009), Apatite (U–Th)/He thermochronometry using a radiation damage accumulation and annealing model,

- Geochim. Cosmochim. Acta*, 73(8), 2347-2365, doi:10.1016/j.epsl.2006.07.028.
- Flowers, R., B. Wernicke, and K. Farley (2008), Unroofing, incision, and uplift history of the southwestern Colorado Plateau from apatite (U-Th)/He thermochronometry, *Geol. Soc. Am. Bull.*, 120(5-6), 571-587, doi: 10.1130/B26231.1.
- Foster, D. A. and B. E. John (1999), Quantifying tectonic exhumation in an extensional orogeny with thermochronology: Examples from the southern Basin and Range Province, *Geological Society, London, Special Publications*, 154(1), 343-364, doi: 10.1144/GSL.SP.1999.154.01.16.
- Gans, P., E. Miller, J. McCarthy, and M. Ouldcott (1985), Tertiary extensional faulting and evolving ductile-brittle transition zones in the northern Snake Range and vicinity: New insights from seismic data, *Geology*, 13(3), 189-193, doi:10.1130/0091-7613(1985)13<189:TEFAED>2.0.CO;2.
- Gans, P. B. (1987), An open-system, two-layer crustal stretching model for the Eastern Great Basin, *Tectonics*, 6(1), 1-12, doi:10.1029/TC006i001p00001.
- Gans, P. B., G. A. Mahood, and E. Schermer (1989), Synextensional magmatism in the Basin and Range Province; A case study from the eastern Great Basin, *Geol. Soc. Am. Spec. Pap.*, 233, 1-53, doi: 10.1130/SPE233-p1.
- Gébelin, A., A. Mulch, C. Teyssier, M. Heizler, T. Vennemann, and N. C. Seaton (2011), Oligo-Miocene extensional tectonics and fluid flow across the Northern Snake Range detachment system, Nevada, *Tectonics*, 30(5), doi:10.1029/2010TC002797.
- Geertsma, J. (1971), Finite-element analysis of shallow temperature anomalies, *Geophys. Prospect.*, 19(4), 662-681, doi: 10.1111/j.1365-2478.1971.tb00909.x.
- Gile, L. H., F. F. Peterson, and R. B. Grossman (1966), Morphological and genetic sequences of

- carbonate accumulation in desert soils., *Soil Sci.*, *101*(5), 347-360.
- Gorynski, K. E., D. F. Stockli, and J. D. Walker (2013), Thermochronometrically constrained anatomy and evolution of a Miocene extensional accommodation zone and tilt domain boundary: The southern Wassuk Range, Nevada, *Tectonics*, *32*(3), 516-539, doi:10.1002/tect.20044.
- Greene, D. C. (2014), The Confusion Range, west-central Utah: Fold-thrust deformation and a western Utah thrust belt in the Sevier hinterland, *Geosphere*, *10*(1), 148-169, doi: 10.1130/GES00972.1.
- Guenther, W. R., P. W. Reiners, R. A. Ketcham, L. Nasdala, and G. Giester (2013), Helium diffusion in natural zircon: Radiation damage, anisotropy, and the interpretation of zircon (U-Th)/He thermochronology, *Am. J. Sci.*, *313*(3), 145-198, doi: 10.2475/03.2013.01.
- Hanson, A. D. (2014), A surprising asymmetric paleothermal anomaly around El Gordo diapir, La Popa Basin, Mexico, *AAPG Bull.*, *98*(2), 213-226, doi:10.1306/06171312226.
- Hintze, L. F. and M. G. Best (1987), Geologic Map of the Mountain Home Pass and Miller Wash Quadrangles, Millard and Beaver Counties, Utah and Lincoln County, Nevada, *Misc. Field Studies Map 1950*, scale 1:24,000, 1 p.
- Hintze, L. (1986), Geologic Map of the Mormon Gap and Tweedy Wash Quadrangles, Millard County, Utah and Lincoln and White Pine Counties, Nevada, *Misc. Field Studies Map 1872*, 1:24,000, 1 p.
- Hodges, K. and J. Walker (1992), Extension in the Cretaceous Sevier orogen, North American Cordillera, *Geol. Soc. Am. Bull.*, *104*(5), 560-569, doi: 10.1130/0016-7606(1992)104<0560:EITCSO>2.3.CO;2.
- Hoffman, M. (2009), Mio-Pliocene erosional exhumation of the central Colorado Plateau,

- eastern Utah: New insights from apatite (U-Th)/He thermochronometry, M.S. thesis, Dep. of Geol., Univ. of Kansas, Lawrence, Kansas, United States of America.
- Hose, R. K., and M. Blake Jr. (1976), Geology and mineral resources of White Pine County, Nevada Part I, *Nevada Bureau of Mines and Geology Bulletin*, 85(1), 1-35.
- Hose, R. and M. Blake Jr. (1970), Geologic map of White Pine County, Nevada, *U.S. Geol. Surv. Open-File Report OF-70-166*, scale 1:147,300, 4 p.
- Hourigan, J. K., P. W. Reiners, and M. T. Brandon (2005), U-Th zonation-dependent alpha ejection in (U-Th)/He chronometry, *Geochim. Cosmochim. Ac.*, 69(13), 3349-3365, doi:10.1016/j.gca.2005.01.024.
- House, M. A., K. A. Farley, and B. P. Kohn (1999), An empirical test of helium diffusion in apatite: Borehole data from the Otway basin, Australia, *Earth Planet. Sci. Lett.*, 170(4), 463-474, doi:10.1016/S0012-821X(99)00120-X.
- House, M. A., B. P. Wernicke, and K. A. Farley (1998), Dating topography of the Sierra Nevada, California, using apatite (U-Th)/He ages, *Nature*, 396(6706), 66-69, doi:10.1038/23926.
- House, P. K., B. J. Buck, and A. R. Ramelli (2010), Geologic assessment of piedmont and playa flood hazards in the Ivanpah Valley area, Clark County, Nevada, *NBMG Report 53*, <http://data.nbmг.unr.edu/Public/freedownloads/r/r053/>.
- Jensen, P. K. (1990), Analysis of the temperature field around salt diapirs, *Geothermics*, 19(3), 273-283, doi:10.1016/0375-6505(90)90047-F.
- Jensen, P. K. (1983), Calculations on the thermal conditions around a salt diapir, *Geophys. Prospect.*, 31(3), 481-489, doi:10.1111/j.1365-2478.1983.tb01064.x.
- John, B. E. and D. A. Foster (1993), Structural and thermal constraints on the initiation angle of detachment faulting in the southern Basin and Range: The Chemehuevi Mountains case

- study, *Geol. Soc. Am. Bull.*, 105(8), 1091-1108, doi: 10.1130/0016-7606(1993)105<1091:SATCOT>2.3.CO;2.
- Karlstrom, K., D. Coblenz, K. Dueker, W. Ouimet, E. Kirby, J. Van Wijk, B. Schmandt, S. Kelley, G. Lazear, and L. Crossey (2012), Mantle-driven dynamic uplift of the Rocky Mountains and Colorado Plateau and its surface response: Toward a unified hypothesis, *Lithosphere*, 4(1), 3-22, doi: 10.1130/L150.1.
- Ketcham, R. A. (2005), Forward and inverse modeling of low-temperature thermochronometry data, *Rev. Mineral. Geochem.*, 58(1), 275-314, doi: 10.2138/rmg.2005.58.11.
- Konstantinou, A., A. Strickland, E. L. Miller, and J. P. Wooden (2012), Multistage Cenozoic extension of the Albion–Raft River–Grouse Creek metamorphic core complex: Geochronologic and stratigraphic constraints, *Geosphere*, GES00778.1, doi:10.1130/GES00778.1.
- Kreemer, C., G. Blewitt, and W. C. Hammond (2010), Evidence for an active shear zone in southern Nevada linking the Wasatch fault to the Eastern California shear zone, *Geology*, 38(5), 475-478, doi:10.1130/G30477.1.
- Lawton, T. F. and B. J. Buck (2006), Implications of diapir-derived detritus and gypsic paleosols in Lower Triassic strata near the Castle Valley salt wall, Paradox Basin, Utah, *Geology*, 34(10), 885-888, doi:10.1130/G22574.1.
- Lazear, G., K. Karlstrom, A. Aslan, and S. Kelley (2013), Denudation and flexural isostatic response of the Colorado Plateau and southern Rocky Mountains region since 10 Ma, *Geosphere*, 9(4), 792-814, doi:10.1130/GES00836.1.
- Lee, D. and E. Christiansen (1983), The granite problem as exposed in the southern Snake Range, Nevada, *Contrib. Mineral. Petr.*, 83(1-2), 99-116.

- Lee, D., R. Marvin, and H. Mehnert (1980), Geologic studies in White Pine County, Nevada: A radiometric age study of Mesozoic-Cenozoic metamorphism in eastern White Pine County, Nevada, and nearby Utah, *U.S. Geol. Surv. Prof. Pap. 1158*, 17-28.
- Lee, D., J. Stacey, and L. Fischer (1986), Muscovite phenocrystic two mica granites of northeastern Nevada are Late Cretaceous in age, in *Shorter Contributions to Isotope Research* edited by Z.E. Peterman and D.C. Schanbel, *U.S. Geol. Surv. Bull.*, B1622, 31-39.
- Lee, D. E., R. F. Marvin, T. Stern, and Z. E. Peterman (1970), Modification of potassium-argon ages by Tertiary thrusting in the Snake Range, White Pine County, Nevada, *U.S. Geol. Surv. Prof. Pap. 700-D*, D92-D102.
- Lee, D. E., T. Stern, R. Mays, and R. Van Loenen (1968), Accessory zircon from granitoid rocks of the Mount Wheeler mine area, Nevada, *U.S. Geol. Surv. Prof. Pap. 600-D*, D197-D203.
- Lee, D. E., R. E. Van Loenen, and R. Mays (1973), Accessory apatite from hybrid granitoid rocks of the southern Snake Range, Nevada, *Jour. Research U.S. Geol. Surv.*, 1, 89-98.
- Lee, J. (1995), Rapid uplift and rotation of mylonitic rocks from beneath a detachment fault: Insights from potassium feldspar $^{40}\text{Ar}/^{39}\text{Ar}$ thermochronology, northern Snake Range, Nevada, *Tectonics*, 14(1), 54-77, doi:10.1029/94TC01508.
- Lee, J. and J. F. Sutter (1991), Incremental $^{40}\text{Ar}/^{39}\text{Ar}$ thermochronology of mylonitic rocks from the northern Snake Range, Nevada, *Tectonics*, 10(1), 77-100, doi:10.1029/90TC01931.
- Lewis, C. J., B. P. Wernicke, J. Selverstone, and J. M. Bartley (1999), Deep burial of the footwall of the northern Snake Range décollement, Nevada, *Geol. Soc. Am. Bull.*, 111(1),

- 39-51, doi: 10.1130/0016-7606(1999)111<0039:DBOTFO>2.3.CO;2.
- Long, S. P. (2012), Magnitudes and spatial patterns of erosional exhumation in the Sevier hinterland, eastern Nevada and western Utah, USA: Insights from a Paleogene paleogeologic map, *Geosphere*, 8(4), 881-901, doi: 10.1130/GES00783.1.
- Long, S. P., S. N. Thomson, P. W. Reiners, and R. V. Di Fiori (2015), Synorogenic extension localized by upper-crustal thickening: An example from the Late Cretaceous Nevadaplano, *Geology*, 43(4), 351-354, doi:10.1130/G36431.1.
- MacCready, T., A. W. Snoke, J. E. Wright, and K. A. Howard (1997), Mid-crustal flow during Tertiary extension in the Ruby Mountains core complex, Nevada, *Geol. Soc. Am. Bull.*, 109(12), 1576-1594, doi: 10.1130/0016-7606(1997)109<1576:MCFDTE>2.3.CO;2.
- Mankinen, E. A. and S. N. W. Authority (2007), Geophysical Data from Spring Valley to Delamar Valley, East-Central Nevada, *U.S. Geol. Surv. Open-File Report*, 2007-1190, pp. 42.
- Martinez, C. M. (2001), Characteristics of sedimentary basins formed above low-angle detachment faults: Examples from the Basin and Range province, western US, paper 1610 presented at Geological Society of America Abstracts with Program, Annual meeting, 5-8 November.
- McGrew, A. J. (1993), The origin and evolution of the southern Snake Range décollement, east central Nevada, *Tectonics*, 12(1), 21-34, doi:10.1029/92TC01713.
- McGrew, A. J., J. L. Brown, and E. L. Miller (1995), Geologic Map of Kiou Spring and Garrison 7.5' Quadrangles, White Pine County, Nevada and Millard County, Utah, *U.S. Geol. Surv. Open-File Report OF-95-10*, scale 1:24,000, 20 p.
- McGrew, A. J. and L. W. Snee (1994), $^{40}\text{Ar}/^{39}\text{Ar}$ thermochronologic constraints on the

- tectonothermal evolution of the Northern East Humboldt range metamorphic core complex, Nevada, *Tectonophysics*, 238(1), 425-450, doi:10.1016/0040-1951(94)90067-1.
- McMillan, M. E., P. L. Heller, and S. L. Wing (2006), History and causes of post-Laramide relief in the Rocky Mountain orogenic plateau, *Geol. Soc. Am. Bull.*, 118(3-4), 393-405, doi: 10.1130/B25712.1.
- Mello, U. T., G. D. Karner, and R. N. Anderson (1995), Role of salt in restraining the maturation of subsalt source rocks, *Mar. Pet. Geol.*, 12(7), 697-716, doi:10.1016/0264-8172(95)93596-V.
- Miller, E. L., P. B. Gans, J. E. Wright, and J.F. Sutter (1988), Metamorphic history of the east-central Basin and Range province: Tectonic setting and relationship to magmatism, in *Metamorphism and Crustal Evolution, Western Conterminous United States*, edited by W. G. Ernst, pp. 649-682.
- Miller, E. L., T. A. Dumitru, R. W. Brown, and P. B. Gans (1999), Rapid Miocene slip on the Snake Range–Deep Creek Range fault system, east-central Nevada, *Geol. Soc. Am. Bull.*, 111(6), 886-905, doi:10.1130/0016-7606(1999)111<0886:RMSOTS>2.3.CO;2.
- Miller, E. L. and P. B. Gans (1989), Cretaceous crustal structure and metamorphism in the hinterland of the Sevier thrust belt, western US Cordillera, *Geology*, 17(1), 59-62, doi: 10.1130/0091-7613(1989)017<0059:CCSAMI>2.3.CO;2.
- Miller, E. L., P. B. Gans, and J. Garing (1983), The Snake Range décollement: An exhumed mid-Tertiary ductile-brittle transition, *Tectonics*, 2(3), 239-263 doi:10.1029/TC002i003p00239.
- Miller, E. L., M. M. Miller, C. H. Stevens, J. E. Wright, and R. Madrid (1992), Late Paleozoic

- paleogeographic and tectonic evolution of the western US Cordillera in *The Cordilleran Orogen: Conterminous U.S.*, vol. G-3, edited by B. C. Burchfiel, P. W. Lipman, and M. L. Zoback, pp. 57-106, Geological Society of America, Boulder, Colorado.
- Misch, P. (1960), Regional structural reconnaissance in central-northeast Nevada and some adjacent areas: Observations and interpretations, Intermountain Association of Petroleum Geologists Guidebook for 11th Annual Field Conference, 17-42.
- Morrison, S. and W. Parry (1986), Formation of carbonate-sulfate veins associated with copper ore deposits from saline basin brines, Lisbon Valley, Utah; Fluid inclusion and isotopic evidence, *Econ. Geol.*, 81(8), 1853-1866, doi: 10.2113/gsecongeo.81.8.1853.
- Mosegaard, K. and A. Tarantola (1995), Monte Carlo sampling of solutions to inverse problems, *J. Geophys. Res.: Sol. Ea. (1978–2012)*, 100(B7), 12431-12447, doi: 10.1029/94JB03097.
- Mueller, K. J. and A. W. Snoke (1993), Progressive overprinting of normal fault systems and their role in Tertiary exhumation of the East Humboldt-Wood Hills Metamorphic Complex northeast Nevada, *Tectonics*, 12(2), 361-371, doi:10.1029/92TC01967.
- Nagihara, S. (2003), Three-dimensional inverse modeling of the refractive heat-flow anomaly associated with salt diapirism, *AAPG Bull.*, 87(7), 1207-1222.
- Nagihara, S., J. G. Sclater, L. M. Beckley, E. W. Behrens, and L. A. Lawver (1992), High heat flow anomalies over salt structures on the Texas continental slope, Gulf of Mexico, *Geophys. Res. Lett.*, 19(16), 1687-1690, doi:10.1029/92GL00976.
- O'Brien, J. and I. Lerche (1984), The influence of salt domes on paleotemperature distributions, *Geophysics*, 49(11), 2032-2043, doi:10.1190/1.1441614.
- Pearson, R. K. (2011), *Exploring Data in Engineering, the Sciences, and Medicine*, New York,

- Oxford University Press, 792 p.
- Pederson, J. L., R. D. Mackley, and J. L. Eddleman (2002), Colorado Plateau uplift and erosion evaluated using GIS, *GSA TODAY*, 12(8), 4-10.
- Peters, K. (1986), Guidelines for evaluating petroleum source rock using programmed pyrolysis, *AAPG Bull.*, 70(3), 318-329.
- Peters, K. E. and M. R. Cassa (1994), Applied source rock geochemistry, *The petroleum system From source to trap: AAPG Memoir 60*, edited by L.B. Magoon and W.G. Dow, 93-120.
- Petersen, K. and I. Lerche (1995), Quantification of thermal anomalies in sediments around salt structures, *Geothermics*, 24(2), 253-268, doi:10.1016/0375-6505(94)00051-D.
- Peterson, F. F. (1981), Landforms of the Basin & Range province defined for soil survey, *Nevada Agricultural Experiment Station Max C. Fleischmann College of Agriculture University of Reno Technical Bulletin 28*, 1-56.
- Poole, F. G., J. H. Stewart, A. R. Palmer, C. A. Sandberg, R. J. Madrid, R. J. Ross, L. F. Hintze, M. M. Miller, and C. T. Wrucke (1992), Latest Precambrian to Devonian time: Development of a continental margin, in *The Cordilleran Orogen: Conterminous U.S.*, vol. G-3, edited by B. C. Burchfiel, P. W. Lipman, and M. L. Zoback, pp. 9-56, Geological Society of America, Boulder, Colorado.
- Portenga, E. W. and P. R. Bierman (2011), Understanding Earth's eroding surface with ¹⁰ Be, *GSA Today*, 21(8), 4-10, doi: 10.1130/G111A.1.
- Rashid, M. and J. McAlary (1977), Early maturation of organic matter and genesis of hydrocarbons as a result of heat from a shallow piercement salt dome, *J. Geochem. Explor.*, 8(3), 549-569, doi:10.1016/0375-6742(77)90098-X.
- Reiners, P. W. (2005), Zircon (U-Th)/He thermochronometry, *Rev. Mineral. Geochem.*,

- 58(1936), 151-179, doi:10.2138/rmg.2005.58.6.
- Reiners, P. W. and M. T. Brandon (2006), Using thermochronology to understand orogenic erosion, *Annu. Rev. Earth Planet. Sci.*, *34*, 419-466, doi:10.1146/annurev.earth.34.031405.125202.
- Roberts, G., N. White, G. Martin-Brandis, and A. Crosby (2012), An uplift history of the Colorado Plateau and its surroundings from inverse modeling of longitudinal river profiles, *Tectonics*, *31*(4), TC4022, doi: 10.1029/2012TC003107.
- Saltzer, S. and K. Hodges (1988), The Middle Mountain shear zone, southern Idaho: Kinematic analysis of an early Tertiary high-temperature detachment, *Geol Soc. Am. Bull.*, *100*(1), 96-103.
- Sambridge, M. (1999), Geophysical inversion with a neighbourhood algorithm—I. Searching a parameter space, *Geophys. J. Int.*, *138*(2), 479-494, doi:10.1046/j.1365-246X.1999.00876.x.
- Sambridge, M. and K. Mosegaard (2002), Monte Carlo methods in geophysical inverse problems, *Rev. Geophys.*, *40*(3), 1009, doi:10.1029/2000RG000089.
- Sawyer, T.L., compiler (1998), Fault number 1430, Wheeler Peak fault zone, in Quaternary fault and fold database of the United States: U.S. Geological Survey website, <http://earthquakes.usgs.gov/hazards/qfaults>, accessed February 15, 2014.
- Schildgen, T. F., T. A. Ehlers, D. M. Whipp, M. C. van Soest, K. X. Whipple, and K. V. Hodges (2009a), Quantifying canyon incision and Andean Plateau surface uplift, southwest Peru: A thermochronometer and numerical modeling approach, *J. Geophys. Res.: Ea. Surf.* (2003–2012), *114*(F4), F04014, doi:10.1029/2009JF001305.
- Schildgen, T. F., K. V. Hodges, K. X. Whipple, M. S. Pringle, M. van Soest, and K. Cornell

- (2009b), Late Cenozoic structural and tectonic development of the western margin of the Central Andean Plateau in southwest Peru, *Tectonics*, 28(4), doi:10.1029/2008TC002403.
- Selig, F. and G. C. Wallick (1966), Temperature distribution in salt domes and surrounding sediments, *Geophysics*, 31(2), 346-361, doi:10.1190/1.1439777.
- Shawe, D. R., G. C. Simmons, and N. L. Archbold (1968), Stratigraphy of Slick Rock District and vicinity, San Miguel and Dolores Counties, Colorado, *U.S. Geol. Surv. Prof. Pap.*, 576-A, A1-A108.
- Shoemaker, E. M., J. Case, and D. Elston (1958), Salt anticlines of the Paradox basin, *Ninth Annual Field Conference Intermountain Association of Petroleum Geologists*, 39-59.
- Shuster, D. L., R. M. Flowers, and K. A. Farley (2006), The influence of natural radiation damage on helium diffusion kinetics in apatite, *Earth Planet. Sci. Lett.*, 249(3), 148-161, doi:10.1016/j.epsl.2006.07.028.
- Snell, K. E., P. L. Koch, P. Druschke, B. Z. Foreman, and J. M. Eiler (2014), High elevation of the 'Nevadaplano' during the Late Cretaceous, *Earth Planet. Sci. Lett.*, 386, 52-63, doi:10.1016/j.epsl.2013.10.046.
- Sonder, L. J. and C. H. Jones (1999), Western United States extension: How the west was widened, *Ann. Rev. Earth Planet. Sci.*, 27(1), 417-462, doi:10.1146/annurev.earth.27.1.417.
- Spell, T. L., E. I. Smith, A. Sanford, and K. A. Zanetti (2001), Systematics of xenocrystic contamination: Preservation of discrete feldspar populations at McCullough Pass Caldera revealed by $^{40}\text{Ar}/^{39}\text{Ar}$ dating, *Earth Planet. Sci. Lett.*, 190(3), 153-165, doi:10.1016/S0012-821X(01)00382-X.
- Stockli, D. F. (2005), Application of low-temperature thermochronometry to extensional tectonic

- settings, *Rev. Mineral. Geochem.*, 58(1936), 411-448, doi:10.2138/rmg.2005.58.16.
- Stockli, D. F., T. A. Dumitru, M. O. McWilliams, and K. A. Farley (2003), Cenozoic tectonic evolution of the White Mountains, California and Nevada, *Geological Society of America Bulletin*, 115(7), 788-816, doi: 10.1130/0016-7606(2003)115<0788:CTEOTW>2.0.CO;2.
- Stockli, D. F., K. A. Farley, and T. A. Dumitru (2000), Calibration of the apatite (U-Th)/He thermochronometer on an exhumed fault block, White Mountains, California, *Geology*, 28(11), 983-986, doi: 10.1130/0091-7613(2000)28<983:COTAHT>2.0.CO;2.
- Stockli, D. F., B. E. Surpless, T. A. Dumitru, and K. A. Farley (2002), Thermochronological constraints on the timing and magnitude of Miocene and Pliocene extension in the central Wassuk Range, western Nevada, *Tectonics*, 21(4), 10-1-10-19, doi:10.1029/2001TC001295.
- Stokes, W. L. and D. A. Phoenix (1948), Geology of the Egnar-Gypsum Valley area, San Miguel and Montrose Counties, Colorado, *U.S. Geol. Surv. Oil and Gas Investigations Map OM-93*, scale 1:48,000, 1 p.
- Styron, R. H., M. H. Taylor, K. E. Sundell, D. F. Stockli, J. A. Oalman, A. Möller, A. T. McCallister, D. Liu, and L. Ding (2013), Miocene initiation and acceleration of extension in the South Lunggar rift, western Tibet: Evolution of an active detachment system from structural mapping and (U-Th)/He thermochronology, *Tectonics*, 32(4), 880-907, doi:10.1002/tect.20053.
- Tarantola, A. (2005), *Inverse problem theory: Methods for data fitting and model parameter estimation*, Elsevier, Amsterdam, The Netherlands, 630 p.
- Taylor, W. J. (1990), Spatial and temporal relations of Cenozoic volcanism and extension in the North Pahroc and Seaman Ranges, eastern Nevada, *Geol. Soc. of Am. Mem.*, 176, 181-

194, doi: 10.1130/MEM176-p181

Taylor, W. J. and J. M. Bartley (1992), Prevolcanic extensional Seaman breakaway fault and its geologic implications for eastern Nevada and western Utah, *Geol Soc. Am. Bull.*, 104(3), 255-266, doi: 10.1130/0016-7606(1992)104<0255:PESBFA>2.3.CO;2.

Taylor, W. J., J. M. Bartley, M. W. Martin, J. W. Geissman, J. D. Walker, P. A. Armstrong, and J. E. Fryxell (2000), Relations between hinterland and foreland shortening: Sevier orogeny, central North American Cordillera, *Tectonics*, 19(6), 1124-1143, doi:10.1029/1999TC001141.

Tissot, B., R. Pelet, and P. Ungerer (1987), Thermal history of sedimentary basins, maturation indices, and kinetics of oil and gas generation, *AAPG Bull.*, 71(12), 1445-1466.

Trexler, J. H., P. H. Cashman, W. S. Snyder, and V. I. Davydov (2004), Late Paleozoic tectonism in Nevada: Timing, kinematics, and tectonic significance, *Geol. Soc. Am. Bull.*, 116(5-6), 525-538, doi: 10.1130/B25295.1.

Trudgill, B. (2011), Evolution of salt structures in the northern Paradox Basin: Controls on evaporite deposition, salt wall growth and supra-salt stratigraphic architecture, *Basin Res.*, 23(2), 208-238.

Tschanz, C. M. and E. H. Pampeyan (1970), Geology and mineral deposits of Lincoln County, Nevada, *Nevada Bur. Mines. Bull.*, 73, 1-188.

Tschanz, C. M. and E. Pampeyan (1961), Preliminary geologic map of Lincoln County, Nevada: *U.S. Geol. Surv. Min. Inv. Field Studies Map MF-206*, 1:200,000 scale, 2 p.

U.S. Geological Survey and Nevada Bureau of Mines and Geology (2006), Quaternary fault and fold database for the United States, <http://earthquake.usgs.gov/hazards/qfaults/>, accessed February 15, 2014.

- van Soest, M. C., K. V. Hodges, J. Wartho, M. B. Biren, B. D. Monteleone, J. Ramezani, J. G. Spray, and L. M. Thompson (2011), (U-Th)/He dating of terrestrial impact structures: The Manicouagan example, *Geochem. Geophys. Geosys.*, *12*(5), Q0AA16, doi:10.1029/2010GC003465.
- Vizgirda, J., J. O'Brien, and I. Lerche (1985), Thermal anomalies on the flanks of a salt dome, *Geothermics*, *14*(4), 553-565, doi:10.1016/0375-6505(85)90006-9.
- Waples, D. W. (1980), Time and temperature in petroleum formation: Application of Lopatin's method to petroleum exploration, *AAPG Bull.*, *64*(6), 916-926.
- Waples, D. W. (1994), Maturity modeling: Thermal indicators, hydrocarbon generation, and oil cracking, *The petroleum system-From source to trap: AAPG Memoir 60*, edited by L.B. Magoon and W.G. Dow 285-285.
- Wells, M. L., R. D. Dallmeyer, and R. W. Allmendinger (1990), Late Cretaceous extension in the hinterland of the Sevier thrust belt, northwestern Utah and southern Idaho, *Geology*, *18*(10), 929-933, doi: 10.1130/0091-7613(1990)018<0929:LCEITH>2.3.CO;2.
- Wells, M. L., L. W. Snee, and A. E. Blythe (2000), Dating of major normal fault systems using thermochronology: An example from the Raft River detachment, Basin and Range, western United States, *J. Geophys. Res.: Sol. Ea. (1978–2012)*, *105*(B7), 16303-16327, doi:10.1029/2000JB900094.
- Wernicke, B. (1992), Cenozoic extensional tectonics of the US Cordillera, in *The Cordilleran Orogen: Conterminous U.S.*, vol. G-3, edited by B. C. Burchfiel, P. W. Lipman, and M. L. Zoback, pp. 553-581, Geological Society of America, Boulder, Colorado.
- Wendt, I. and C. Carl (1991), The statistical distribution of the mean squared weighted deviation, *Chem. Geol.*, *86*(4), 275-285.

- Wesnousky, S. G. and C. H. Willoughby (2003), Neotectonic Note: The Ruby–East Humboldt Range, Northeastern Nevada, *B. Seismol. Soc. Am.*, 93(3), 1345-1354, doi:10.1785/0120020032.
- Whitebread, D. H. (1969), Geologic Map of the Wheeler Peak and Garrison Quadrangles, Nevada and Utah, *U.S. Geol. Surv. Misc. Investigations Map 1-578*, 1:48,000 scale.
- Whittington, A. G., A. M. Hofmeister, and P. I. Nábělek (2009), Temperature-dependent thermal diffusivity of the Earth's crust and implications for magmatism, *Nature*, 458(7236), 319-21, doi:10.1038/nature07818.
- Wolf, R., K. Farley, and D. Kass (1998), Modeling of the temperature sensitivity of the apatite (U–Th)/He thermochronometer, *Chem. Geol.*, 148(1), 105-114, doi:10.1016/S0009-2541(98)00024-2.
- Wolf, R., K. Farley, and L. Silver (1996), Helium diffusion and low-temperature thermochronometry of apatite, *Geochim. Cosmochim. Ac.*, 60(21), 4231-4240, doi:10.1016/S0016-7037(96)00192-5.
- Wolfe, M. R., and D. F. Stockli (2010), Zircon (U–Th)/He thermochronometry in the KTB drill hole, Germany, and its implications for bulk He diffusion kinetics in zircon, *Earth Planet. Sci. Lett.*, 295(1), 69-82, doi:10.1016/j.epsl.2010.03.025.
- Yu, Z., I. Lerche, and A. Lowrie (1992), Thermal impact of salt: Simulation of thermal anomalies in the Gulf of Mexico, *Gulf Coast Assoc. of Geol. Soc. Trans.*, 42, 381-387.
- Zhao, C., B. E. Hobbs, and A. Ord (2008), *Convective and Advective Heat Transfer in Geological Systems*, Berlin Heidelberg, Springer-Verlag, 229 p.

Curriculum Vitae

Education

Completion: **Ph.D. Candidate Geoscience**, University of Nevada, Las Vegas
May 2016
Dissertation Title: *(U-Th)/He studies of the Southern Snake Range Metamorphic Core Complex, NV and Gypsum Valley Salt Wall, Paradox Basin, CO, USA*, advisor: Andrew Hanson

December 2011 **M.S. Geology with Honors**, University of Kansas
Thesis Title: *Timing of exhumation of the eastern Central Alps from zircon and apatite (U-Th)/He thermochronology (Graubünden, Switzerland)*, advisor: Daniel Stockli

August 2008 **B.S. Geological Sciences with Highest Distinction**
University of North Carolina, Chapel Hill
Honors Thesis: *The structural nature of the Laurel Creek lineament, NC*, advisor: Kevin Stewart

Teaching and Professional Experience

2015 **Lecture Instructor**, University of Nevada, Las Vegas
Physical Geography of Earth's Environment

2014-2015 **Graduate Teaching Assistant**, University of Nevada, Las Vegas
Introductory Geology Laboratory Instructor
Historical Geology Laboratory Instructor
Sedimentology and Stratigraphy Laboratory Instructor

Sept.–Dec. 2013 **Geoscience Intern**, ExxonMobil Production Company

2009-2011 **Graduate Research Assistant**, University of Kansas
Isotope Geochemistry Laboratory

2008-2010 **Graduate Teaching Assistant**, University of Kansas
Mineral Structures and Equilibria Laboratory Instructor
Igneous and Metamorphic Petrology Laboratory Instructor
Earthquakes and Natural Disasters Teaching Assistant
Prehistoric Life: DNA to Dinosaurs Teaching Assistant

Research Experience

Noble Gas Geochronology and Geochemistry Laboratories, (U-Th)/He analyses, Arizona State University (Apr.-Jun., 2013; May-Jun., 2015)

Low-Temperature Thermochronology Sampling, Onion Creek Diapir, UT (Mar., 2015)

Nevada Isotope and Geochronology Lab, ^{40}Ar - ^{39}Ar analyses, University of Nevada, Las Vegas (Jul. 2012; Mar., 2013; Aug., 2014)

Installation of Sub-Surface Temperature Probes, Onion Creek Diapir, UT (Jul., 2014)

Low-Temperature Thermochronology Sampling, Gypsum Valley Diapir, CO (Jul., 2014)

Geologic Mapping, Southern Snake Range, NV (Jun.-Jul., 2012; Jun. 2013; Jun. 2014)

Low-Temperature Thermochronology Sampling, Southern Snake Range, NV (Sept., 2012)

Neotectonic Mapping and Trench Logging, Muddy Mountains, NV (Apr., 2012)

Seismic Data, Acquisition, and Processing Short Course, Las Vegas, NV (Oct., 2011)

Isotope Geochemistry Laboratory, (U-Th)/He and U-Pb analyses, University of Kansas (2008-2011)

Low-Temperature Thermochronology Sampling, east Central Alps (Sept.-Oct. 2008; Jun.-Jul. 2009; Aug.-Sept. 2010)

Geochronology and Isotope Geochemistry Laboratory, U-Pb analyses, University of North Carolina (Mar., 2008)

Awards Received

The President's UNLV Foundation Graduate Research Fellowship, University of Nevada, Las Vegas, 2013-2014

- Institution wide competitive award of full tuition and stipend granted to three graduate students an academic year

The Fay and Jack Ross Fellowship, University of Nevada, Las Vegas, 2011-2013

- Full tuition, stipend, and research funds awarded to one outstanding incoming Geoscience Ph.D. student for two years

Outstanding Student Research Grant Proposal, Geological Society of America, 2009

Structural Geology and Tectonics Division Student Research Award, Geological Society of America, 2009

Op White Prize in Geology, Chancellor's Award, University of North Carolina, Chapel Hill, 2008

- Awarded to an outstanding senior in Geological Sciences each year

Grants Received

American Association of Petroleum Geologists Grant-in-Aid, 2015

Graduate Student Research Grant, Nevada Petroleum and Geothermal Society, 2014

Graduate and Professional Student Association Research Grant, University of Nevada, Las Vegas, 2013

Graduate Student Research Grant, Nevada Petroleum and Geothermal Society, 2013

Graduate Student Research Grant, Geological Society of America, 2012

ExxonMobil Global Geoscience Recruiting Grant, ExxonMobil, 2012

Sigma Xi Grant-in-Aid of Research, Sigma Xi, 2010

Graduate Student Research Grant, Geological Society of America, 2009

Undergraduate Research Grant, Geological Society of America SE Section, 2007

Publications

Peer Reviewed Publications

Evans, S. L., R. H. Styron, M. C. van Soest, K. V. Hodges, and A. D. Hanson, 2015, Zircon and apatite (U-Th)/He evidence for Paleogene and Neogene extension in the Southern Snake Range, Nevada, USA, *Tectonics*, v. 34, doi:10.1002/2015TC003913.

Peer Reviewed Publications in Preparation

Evans, S.L., and A.D. Hanson, *in prep*, Geologic Map of the Red Ledges 7.5' Quadrangle, White Pine and Lincoln Counties, Nevada, intended for submission to the Nevada Bureau of Mines and Geology in 2016.

Thesis

Evans, S.L., 2011, Timing of exhumation of the eastern Central Alps from zircon and apatite (U-Th)/He thermochronology (Graubünden, Switzerland) [M.S. Thesis]: University of Kansas, 227 p.

Conference Abstracts

Evans, S.L., A.D. Hanson, K. Sefein, 2012, Pre-Miocene extension within the Southern Snake Range: Insights from preliminary mapping of the Red Ledges Quadrangle, NV, T43C 2690, American Geophysical Union Abstracts, 2012 Fall Meeting.

Evans, S.L., D.F. Stockli, G. Manatschal, 2010, Timing of uplift of Austroalpine and Penninic units of SE Switzerland: Implications from Zircon (U-Th)/He thermochronology, Paper 123-4, Geological Society of America Abstracts with Program, Annual meeting, 31 Oct.-3 Nov.

Evans, S.L., D.F. Stockli, O. Muntener, G. Manatschal, 2009, (U-Th)/He Magnetite dating of exhumed serpentinitized mantle: A case study from the Tasna Ocean-Continent Transition, SE Switzerland: *Geochimica et Cosmochimica Acta*, 73(13), p. A345.